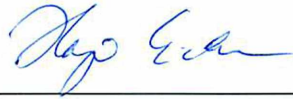# FROM A SNOWFLAKE TO THE SNOW COVER:

PROCESSES THAT SHAPE POLAR AND TAIGA SNOWPACKS

By

Simon Filhol

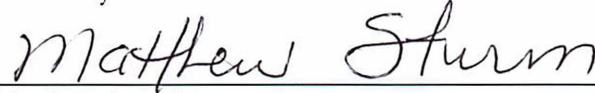RECOMMENDED:
_____

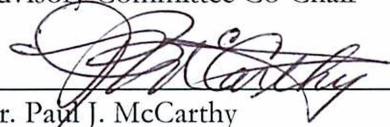Dr. Hajo Eicken

_____

Dr. Christopher F. Larsen

_____

Dr. Martin Truffer
Advisory Committee Co-Chair

_____

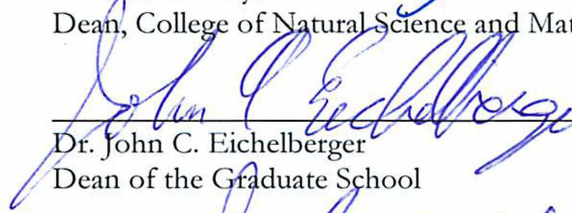Dr. Matthew Sturm
Advisory Committee Co-Chair

_____

Dr. Paul J. McCarthy
Chair, Department of Geosciences

APPROVED:
_____

Dr. Paul W. Layer
Dean, College of Natural Science and Mathematics

_____

Dr. John C. Eichelberger
Dean of the Graduate School

_____

27 July 2016

Date

FROM A SNOWFLAKE TO THE SNOW COVER:

PROCESSES THAT SHAPE POLAR AND TAIGA SNOWPACKS

A

DISSERTATION

Presented to the Faculty

of the University of Alaska Fairbanks

in Partial Fulfillment of the Requirements

for the Degree of

DOCTOR OF PHILOSOPHY

By

Simon Filhol

Fairbanks, AK

August 2016

ABSTRACT

Snowpacks found in boreal and polar regions are the most widespread types of snow in the world, covering up to 14% of the globe. In both regions, snow accumulates over a long period (6-7 months), transforming the landscape by the presence of a thin snowpack ($\leq$70 cm), affecting the local climate, ecology, and hydrology. In the case of polar snow, wind plays a crucial role in redistributing snow, and shaping the snow surface. But in the case of the taiga snow found in the forests of the boreal regions, micro-topography and vegetation are stronger drivers of snow distribution than wind. In this dissertation, I explore the mechanisms responsible for shaping the snow surfaces in windy and in calm conditions. Collecting data at the plot scale with a terrestrial lidar, I sought explanations of the features geometry visible on the snow surfaces in grain scale physical processes. Because snow is close to its fusion temperature in this environment, its behavior at the grain scale can greatly influence its bulk properties. So finding linkages between processes occurring at the grain scale and the observable features at the plot scale may be key to furthering our understanding of snow distribution.

In the first study, I found that the morphology and the occurrence of the seven known types of snow bedforms are dependent on the ability for wind to erode the surface. Erodibility is directly linked to the sintering of wind-slab grains. For this reason, every snow dune eventually turns into sastrugi. In the second study, I studied the effects of underlying topography on the accumulation of snow in calm conditions. I found that processes such as bouncing, cohesion or interlocking of snowflakes can either enhance or inhibit the smoothing of initial bumps. In the third study, I found that plant canopies affect the deposition of snow in the boreal forest. I could differentiate up to five types of canopies for their effects on snow accumulation. Despite the complexity of the canopy structures we observed, over three years, similar accumulation patterns and reactions of canopies to snow loading were seen. I was surprised to find the presence of subnivean cavities associated to plants with a size equivalent to the average snow depth.

TABLE OF CONTENTS

LIST OF FIGURES

LIST OF TABLES

LIST OF APPENDICES

ACKNOWLEDGEMENTS

First coming from France for a five months internship at the Cold Region Research and Engineering Laboratory (CRREL) in Fairbanks, under Tom Douglas, I was drawn to the science about snow done by his coworker Dr. Matthew Sturm. Since, I owe much of this scientific and Alaskan journey to my advisor and mentor Dr. Matthew Sturm. With constant positivity, Matthew led me through this academic program. He taught me how to develop a scientific question, and how to observe and scientifically apprehend snow in its quiet and cold landscape. Despite an initial language barrier, Matthew pursued teaching me the art of writing and presenting my work to the public. Matthew's vibrant passion for winter in northern latitudes, and his insatiable enthusiasm for exploring some of the most remote places of Alaska have been a tremendous source of inspiration and motivation throughout the past six years. I hope being able to preserve and cultivate this set of core values and learning in the future.

The relevance of my scientific inquiries as well as the founding of my hypothesis were consistently challenged by my committee members, Dr. Martin Truffer, Dr. Chris Larsen and Dr. Hajo Eicken, improving, I believe, the quality of the work presented hereafter. I would like to thank them for the time they devoted commenting and editing and discussing my work.

This dissertation is the product of long and strenuous hours spent in the field with colleagues. I would like to acknowledge the valuable help that Chris Polashenski, Art Gelvin, Stephanie Saari, Drew Slater, and Chris Hiemstra have provided through the various seasons in the field. In addition to their physical labor, I will fondly remember the conversations spent discussing science and cross-cultural matters, while waiting for the lidar scanner to finish its measurement cycles.

Six thousands kilometers away from home, I would like to thank my family, Olivier, Nicole and Guilhaume Filhol for always supporting this long lasting project despite the distance and the 10 hours separating us. I have also been lucky to find constant joy, trust and companionship emanating from the precious friendships developed here in Alaska with Alessio Gusmeroli, Josh Barrichelo, Andy Aschwanden, Eyal Saiet, Marc Oggier, Skye Sturm and many more. Finally, I would like to deeply acknowledge my dear and beloved Sarah DeGennaro who over the years not only

participated in many aspects of the work presented hereafter, but always filled our little cabin in the woods with much warmth.

Authors contributions:

The two first chapters are co-authored with Dr. Matthew Sturm who participated for both chapters in editing the manuscripts structurally and grammatically, as well as advising for the design of the experiments. Simon Filhol performed for both chapters the experimental work, data analysis as well as the core manuscript writing. The last chapter is currently single authored by Simon Filhol.

CHAPTER 1: Introduction

When falling and entering a landscape, snowflakes of various shapes and sizes follow unique paths driven by grain-scale physical processes, which ultimately dictate their final destination. Every winter, trillions and trillions of snowflakes fall from the sky, accumulating over land, sea ice, forest, and ice sheets to form in most places, a temporary blanket of snow. In his oil painting representation *Winter* (Figure 1.1), Ivan Shishkin captures the intricacy of the snow cover deposited in a pine forest. Through subtle variations in tone and value, the artist tricks our mind's eye into picturing what lies beneath the blanket of snow covering the forest floor. He also captivates our eyes by depicting the detailed deposition of snow in the pine canopy. What transformative mechanisms has the scene of *Winter* undergone? How has the cumulative effect of single snowflakes falling through the forest canopy and accumulating en mass metamorphosed the entire forest floor? Transported in the air by the wind, bouncing off canopies, landing on other snowflakes, the fate of each snowflake follows a sequence of events that collectively builds the observable snow blanket.

Figure 1.1: *Winter*, oil painting by *Ivan Shishkin* [1890]

Throughout this thesis, I will investigate how the upper boundary of a snowpack, the snow-atmosphere interface, is shaped by the cumulative action of physical processes applied to each individual snowflake. If one thinks of snow depth as being the distance separating the upper and the lower interfaces of the snowpack, then understanding and tracking the evolution of the upper snow

surface's shape is the key to comprehending the origin of snow depth variability, commonly referred to as snow distribution in the scientific literature.

Being in Fairbanks Alaska, and travelling regularly to the North Slope of Alaska, my attention was naturally drawn to taiga and tundra snow [*c.f. Sturm et al.*, 1995] (Figure 1.2). Armed with a terrestrial lidar, I started scanning snow surfaces, and explored their surface geometry. For the first type of snow, taiga snow, which deposits most of the time in calm conditions (no-wind) in forest canopies, I was struck by its smoothing effect on the landscape. Many of the shrubs buried under snow had given way to a smooth rolling surface. Where had these miniature hills originated? Why was the snow surface smooth, not rough? In contrast, windswept tundra snow presents fascinating features like dunes or sastrugi rendering a rough and disordered surface. While both snow packs contain about the same amount of snow (≤ 17 cm of snow water equivalent), how can the action of wind profoundly alter the shape of the resulting snow surface in comparison to taiga snow deposited under calm conditions? Combining physical knowledge of the two types of snow with new lidar technology, allowed me to conduct research on some of the key processes responsible for enhancing or restraining the redistribution of snowflakes, and consequently driving the shapes of snow surfaces.

Tundra and taiga snow are the two most widespread types of snow in the world, particularly if one expands tundra snow to include the snow cover found on sea-ice, ice sheets and any other large open landscapes blown by wind. Combining north and south polar regions, plus sea-ice plus Greenland, what I will refer to as polar snow surfaces covers up to 11% of the globe annually. The taiga forest in which taiga snow covers the ground in winter extends over 11% of continental land. The taiga is the largest terrestrial biome on Earth. In both regions the snowpack lasts for more than two thirds of the year, if not permanently. With such spatial and temporal coverage, the implications of snow for climate, ecology, and hydrology are unequivocal in these two regions of the globe [*Walker et al.*, 1993; *Mote*, 2008; *Orsolini and Kvamtø*, 2009]. And the snow of these regions is already undergoing rapid environmental change [*Derksen and Brown*, 2012; *Hinzman et al., 2013*].

Snow transforms landscapes from dark to bright surfaces reflecting sunlight; it insulates the ground and therefore provides thermal and physical protection to many forms of life. The interactions between snow and life, in particular for plants of the taiga, is such that plants have developed

various strategies and might even affect some control on the distribution of snow to serve their needs (Figure 1.2). In return the effects on the snow cover are quite local (0.1 − 5 m scale) but accumulate in creating a complex landscape scene such as that shown in Figure 1.1.
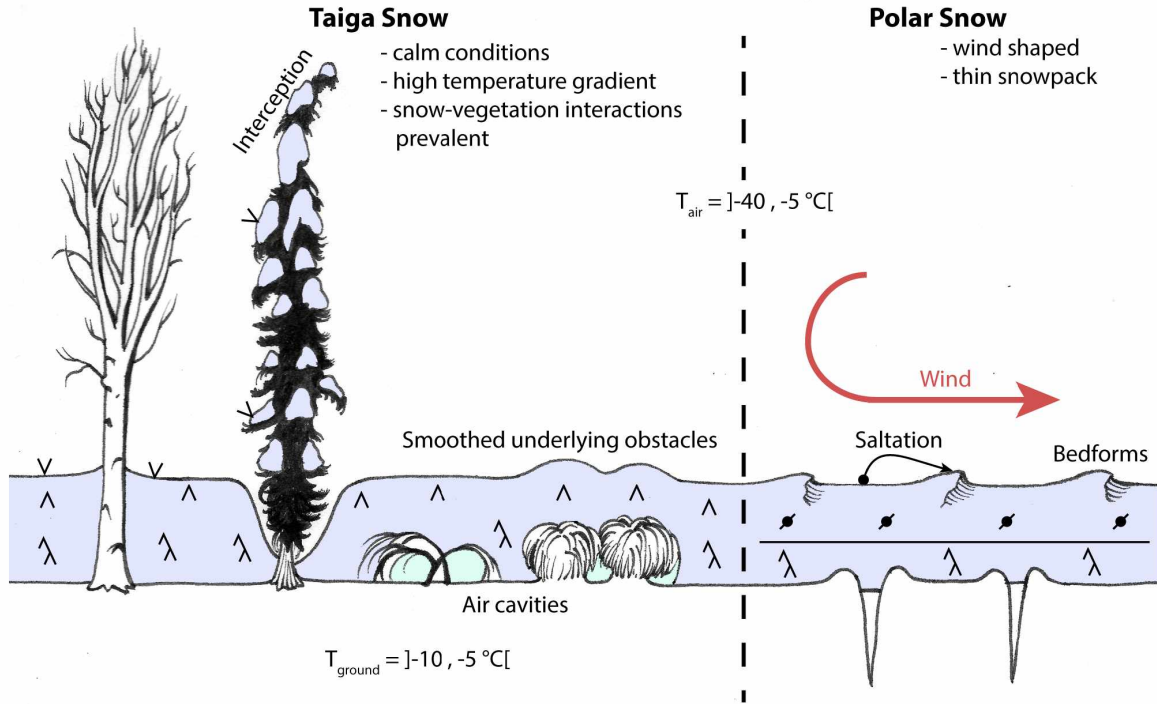
Figure 1.2: Schematic representation of taiga and polar snow covers. Illustration by Sarah DeGennaro.

In his seminal book from 1941, *Bagnold* explored the geomorphology of sand dunes by breaking their physics into the sum of sand grain interactions. Approaching sand as a granular material by linking the physics of sand grains to the geomorphology of dunes, he established the fundamentals for analyzing the dynamics of sand desert features still in use today [*Durán et al.*, 2011; *Parteli et al.*, 2013]. This approach allowed for the development of models grounded in physics, thereby expanding the reach of predictions typically possible from empirical models. In many respects, snow can be observed through the scope of granular material much like sand. Made of billions of grains, the features observable on the snow cover surfaces should find explanations in the cumulative effect of individual snowflakes. Identifying key processes at the grain scale impacting the formation of surface features should help build a fundamental framework for studying snow distribution and the behavior of the snowpack at a larger scale.

In 1954, the Japanese scientist *Nakaya* explained for the first time, through the variables of temperature and water vapor saturation, the genesis of snow crystal shapes. His laboratory, the Institute of Low Temperature Science in Sapporo, Hokkaido, later became a center for snow research with scientists Kuroiwa, Mizuno, Kobayashi, and Kojima, to name a few, that also framed their research around the physics of grains. In 1967, *Kuroiwa et al.* produced a set of experiments through which they looked at snow as a granular material. *Kobayashi* in 1972 photographed snow grains saltating, entrained by wind, revealing the similarity of trajectories between sand and snow grains. Followed in 1980 by the work of *Schmidt*, snow was again interpreted as an ensemble of ice particles susceptible to external forces like the shear stresses induced by wind. *Bunnell and colleagues*, working for the Canadian Forest Service in British Colombia, summarized in a comprehensive report [1985] the advances in the understanding of snow redistribution by tree canopies, largely building on the detailed approach developed by *Miller* [1964] for snow deposition in forests, as well as the set of experiments on snow interception by artificial canopies done by the Japanese government in 1952. In 1987, *Kobayashi* studied snow deposition on flat surfaces, exploring the influence of temperature on the bouncing of snow grains.

Following the comprehensive review on snow interception by trees by *Bunnell et al.* [1985], *Schmidt and Gluns* [1991] started exploring the behavior of snow accumulation in tree branches but once again based on snow grain behavior. A grain falls, bounces off the branch or is intercepted. As snow accumulates, the branch deforms, generating a feedback in the accumulation process. Bridging of the snow clumps might enhance even further the interception efficiency of a branch while the branch bending reduces interception efficiency. Their work was synthesized and abstracted into an empirical model by *Hedstrom and Pomeroy* [1998], which now is the basis for the majority of modeling tools for canopy interception in forest snow accumulation [*Essery et al.*, 2009]. Comparing almost all existing forest snow models, *Rutter et al.* [2009] recently demonstrated the great variability among models, as well as the lack of universality of any of the models. They attributed the scattered predictions to the poor representation of canopy processes in the models. Revisiting our knowledge and our theoretical approach by reconsidering independently the fundamental processes driving canopy interception may be key to improving our understanding of interactions of snow with complex structures like trees.

4

The latest work focusing on grain interactions during the accumulation phase has been the application of fractal surface growth theory to snow accumulation by *Löwe et al.* [2007] and a year later by *Manes et al.* [2008]. Unfortunately, at this time there does not exist a bridge between the knowledge of grain scale processes and their impact on snow distribution at the macro scale. Virtually every model and statistical analysis used to predict snow distribution reaches a lower limit of resolution at the decameter scale [*Brun et al.*, 1989; *Bartelt and Lehning*, 2002; *Liston and Sturm*, 2002; *Trujillo et al.*, 2009, *Grünewald et al.*, 2013] and uses as prediction variables large-scale metrics (*e.g.* topography, elevation, abstract canopy holding capacity, forest density) rather than discrete grains and grain-scale processes.

The most common and cheapest measurement to perform on the snow cover is measuring its depth. Depth is simply calculated as the distance separating the top to the bottom of the snowpack. When sampled in great number, the traditional approach is to derive basic statistics (*e.g.* mean, standard deviation, distribution) for characterizing the snowpack. However, with the new technological development of mapping sensors like lidars (light detection and ranging), it becomes possible to produce samples at such a high resolution that they are no longer independent of one another, which is the case for traditional measurements of depth. With these tools, it is also possible to study the geometry of the surfaces (ground or snow) and their evolution over time. In other words, we can start investigating the processes responsible for the variability in snow depth, and move beyond simple statistical characterizations.

So, throughout this thesis, I have focused on observing how snow covers form in windy and calm environments, and how grain-scale processes are responsible for determining the shape of the snow surfaces. The first section (Chapter 2) of this thesis investigates the role of sintering (the hardening of snow with time) on the sizes of snow dunes and more generally on all snow bedforms, which are typically found in wind swept landscapes. By combining the existing observations, it led to a new classification of snow bedforms providing information on their genesis conditions but also on how each feature relates to the others. The second section (Chapter 3) of this thesis is a set of experiments identifying and investigating how grain scale processes can be responsible for the smoothing and attenuation of underlying relief during the formation of a snow cover under calm conditions. The third section (Chapter 4) is a compilation of comprehensive observations of snow accumulation in the boreal forest, identifying key elements of the forest landscape that affect the

local snow distribution. Finally, in a concluding statement (Chapter 5) I review these contributions, and suggest what areas of interest to build upon in the future.

References

Bagnold, R. A. (1941). The physics of wind blown sand and desert dunes. *Methuen, London*, 265(10).

Bartelt, P., and M. Lehning (2002). A physical SNOWPACK model for the Swiss avalanche warning: Part I: numerical model. *Cold Regions Science and Technology*, 35(3), 123-145, doi: 10.1016/S0165-232X(02)00074-5

Bunnell, F. L., R. S. McNay, and C. C. Shank (1985). Trees and Snow: The Deposition of Snow on the Ground: a Review and Quantitative Synthesis. *Research, Ministries of Environment and Forests.*

Brun, E., E. Martin, V. Simon, C. Gendre, and C. Coleou (1989). An energy and mass model of snow cover suitable for operational avalanche forecasting. *Journal of Glaciology*, 35(12), 1.

Derksen, C., R. Brown (2012). Spring snow cover extent reductions in the 2008–2012 period exceeding climate model projections. *Geophysical Research Letters*, 39, *L19504, doi: 10.1029/2012GL053387.*

Durán, O., P. Claudin, and B. Andreotti (2011), On aeolian transport: Grain-scale interactions, dynamical mechanisms and scaling laws, *Aeolian Research*, 3(3), 243–270, doi: 10.1016/j.aeolia.2011.07.006.

Essery, R., N. Rutter, J. Pomeroy, R. Baxter, M. Stähli, D. Gustafsson, A. Barr, P. Bartlett, and K. Elder (2009), SNOWMIP2: An Evaluation of Forest Snow Process Simulations, *Bulletin of the American Meteorological Society*, 90(8), 1120–1135, doi: 10.1175/2009BAMS2629.1

Grünewald, T., J. Stötter, J. W. Pomeroy, R. Dadic, I. Moreno Baños, J. Marturià, M. Spross, C. Hopkinson, P. Burlando, and M. Lehning (2013), Statistical modelling of the snow depth distribution in open alpine terrain, *Hydrology and Earth System Sciences*, 17, doi: 10.5194/hess-17-3005-2013.

Hedstrom, N. R., and J. W. Pomeroy (1998). Measurements and modeling of snow interception in the boreal forest. *Hydrological Processes*, *12*(1011), 1611-1625, doi: 10.1002/(SICI)1099-1085(199808/09)12:10/11<1611::AID-HYP684>3.0.CO;2-4.

Hinzman, L., C. Deal, A. McGuire, S. Mernild, I. Polyakov, and J. Walsh (2013), Trajectory of the Arctic as an integrated system, *Ecological Applications*, 23(8), 18371868, doi: 10.1890/11-1498.1.

Kobayashi, D. (1972). Studies of snow transport in low-level drifting snow. *Contributions from the Institute of Low Temperature Science*, 24, 1-58.

Kobayashi, D. (1987), Snow accumulation on a narrow board, *Cold Regions Science and Technology*, 13, doi: 10.1016/0165-232X(87)90005-X.

Kuroiwa, D., Y. Mizuno, and M. Takeuchi (1967). Micromeritical properties of snow. *Physics of Snow and Ice: proceedings= 雪氷の物理学: 論文集*, 1(2), 751-772.

Liston, G. E., and M. Sturm (2002). Winter precipitation patterns in arctic Alaska determined from a blowing-snow model and snow-depth observations. *Journal of hydrometeorology*, 3(6), 646-659, doi: 10.1175/1525-7541(2002)003<0646:WPPIAA>2.0.CO;2

Löwe, H., L. Egli, S. Bartlett, M. Guala, and C. Manes (2007). On the evolution of the snow surface during snowfall. *Geophysical Research Letters*, 34(21), *L21507* , doi: 10.1029/2007GL031637.

Manes, C., M. Guala, H. Löwe, S. Bartlett, L. Egli, and M. Lehning (2008). Statistical properties of fresh snow roughness. *Water Resources Research*, 44(11), *W11407*, doi: 10.1029/2007WR006689.

Miller, D. H. (1964) Interception processes during snowstorms. Research Paper PSW-RP-18. Berkeley, CA: Pacific Southwest Forest & Range Experiment Station, Forest Service, U. S. Department of Agriculture; 24 p.

Mote, T. (2008), On the Role of Snow Cover in Depressing Air Temperature, *Journal of Applied Meteorology and Climatology*, 47(7), 20082022, doi: 10.1175/2007JAMC1823.1.

Nakaya, U. (1954). Snow crystals: natural and artificial. *Harvard University Press*.

Orsolini, Y., and N. Kvamstø (2009), Role of Eurasian snow cover in wintertime circulation: Decadal simulations forced with satellite observations, *Journal of Geophysical Research: Atmospheres (1984–2012)*, 114(D19), doi: 10.1029/2009JD012253.

Parteli, E. J., O. Durán, M. C. Bourke, H. Tsoar, T. Poeschel, and H. J. Herrmann (2013), Barchan dune asymmetry: Numerical investigation, *arXiv preprint arXiv:1304.6573*

Rutter, N., R. Essery, J. Pomeroy, N. Altimir, K. Andreadis, I. Baker, A. Barr, P. Bartlett, P., Boone, H. Deng, and H. Douville (2009), Evaluation of forest snow processes models (SnowMIP2), *Journal of Geophysical Research*, 114(D6), doi: 10.1029/2008JD011063

Schmidt, R. A. (1980), Threshold wind-speeds and elastic impact in snow transport, *Journal of Glaciology*, 26, 453-467.

Schmidt, R. A. and D. Gluns (1991), Snowfall interception on branches of three conifer species, *Canadian Journal of Forest Research*, 21(8), 1262–1269, doi: 10.1139/x91-176.

Shishkin, I (1890), Winter, oil painting, *The State Tretyakov Gallery*.

Sturm, M., J. Holmgren, and G. E. Liston (1995), A seasonal snow cover classification system for local to global applications, *Journal of Climate*, *8*(5), 1261-1283, doi: 10.1175/1520-0442(1995)008<1261:ASSCCS>2.0.CO;2

Trujillo, E., J. Ramírez, and K. Elder (2009), Scaling properties and spatial organization of snow depth fields in sub-alpine forest and alpine tundra, *Hydrological Processes*, 23, doi: 10.1002/hyp.7270

Walker, D. A., J. C. Halfpenny, M. D. Walker, and C. A. Wessman (1993). Long-term studies of snow-vegetation interactions. *BioScience*, 43(5), 287-301, doi: 10.2307/1312061

CHAPTER 2: Snow Bedforms: A Review, New Data, and a Formation Model[1]

Abstract

Snow bedforms, like sand bedforms, consist of various shapes that form under the action of wind on mobile particles. Throughout a year, they can cover up to 11% of the Earth surface, concentrated toward the poles. These forms impact the local surface energy balance and the distribution of precipitation. Only a few studies have concentrated on their genesis. Their size ranges from 2 cm (ripple marks) to 2.5 m tall (whaleback dunes). We counted a total of 7 bedforms that are widely recognized. Among them sastrugi, an erosional shape, is the most widespread. From laser scans, we compared scaling of snow versus sand barchan morphology. We found that both have proportionally the same footprint, but snow barchans are flatter. The key difference is that snow can sinter, immobilizing the bedform and creating an erodible material. Using a model, we investigated the effect of sintering on snow dune dynamics. We found that sintering limits their size because it progressively hardens the snow and requires ever-increasing wind speed to maintain snow transport. Compiling the literature and results from this model, we have reclassified snow bedforms based on two parameters: wind speed and snow surface conditions. The new data show that snow dune behavior mirrors that of sand dunes, with merging, calving, and collision. However, isolated snow barchans are rare with most of the snow surfaces encountered in the field consisting of several superimposed bedforms formed sequentially during multiple weather events. Spatially variable snow properties and geometry can explain qualitatively these widespread compound snow surfaces.

2.1 Introduction

Snow bedforms are formations of recognizable sizes, shapes, and patterns at the surface of the snowpack resulting from the conjoint action of wind and moving snow particles. Bedforms in snow include a myriad of features that have analogs in sandy deserts and on river bottoms, including dunes and ripple marks. Other features, like pits, are specific to snow. Collectively, snow bedforms are also known as snow aeolian features.

During the winter of 1902, Vaughan Cornish, a British geographer familiar with sand dunes, traveled across Canada observing the relationship between atmospheric conditions, snow properties and the resulting bedforms [*Cornish*, 1914]. He asked: "What factors are responsible for the bedform shapes, and how do the different shapes relate to each other?" These questions largely remain open today for snow bedforms, as well as for many features found in sand deserts [*Livingstone et al.*, 2007].

This lack of knowledge is surprising when one considers the vast area over which snow bedforms can be found. Including snow bedforms that form on sea ice and the tundra over the course of a year, they can occupy 8 % of the entire globe, an area equivalent to the surface area of Russia, Canada and the USA combined. If we include the ice sheets of Antarctica and Greenland, about 11 % of the terrestrial globe can exhibit snow bedforms.

Despite their extent, only a few scientists have studied or characterized snow bedforms, and scientific interest in their work is low. The few seminal studies about snow bedforms (*e.g. Kobayashi* [1980] and *Doumani* [1967]) have rarely been cited in comparison to equivalent studies about sand bedforms [*Bagnold*, 1941], which have been cited thousands of times. This large gap in interest might relate to the scarcity of the population in regions where snow bedforms occur, or perhaps it is because snow bedforms have an ephemeral life span in comparison to sand bedforms.

Regardless of the reason for the limited amount of interest, snow bedforms have an importance that extends beyond their extent or the complexity of their shapes. The forms influence the Earth's surface roughness in two climate-critical regions (the Arctic and Antarctic), thereby affecting the regional energy balance. This complex surface roughness also complicates the estimation of snow precipitation using microwave remote sensing imagery [*Picard et al.*, 2014], making it difficult to do regional and global water balances. And the rough snow surfaces on ice sheets are known to modify the exchange of air between the firn and the atmosphere, a key process affecting the interpretation of deep ice cores in paleoclimatology [*Colbeck*, 1989; *Albert and Hawley*, 2002; *Birnbaum et al.*, 2010]. Blowing snow on sea ice produces bedforms that set where melt ponds will form in the spring, affecting the sea ice melt rate [*Petrich et al.*, 2012], and these bedforms increase the transfer of momentum between the atmosphere and the sea ice by increasing its surface roughness [*Castellani et al.*, 2014].

Historically, the two practical uses for studying snow aeolian features were: 1) to determine the wind patterns across the Antarctic plateau, and 2) to improve understanding of the accumulation of precipitation on ice caps for mass balance [*Moss,* 1938; *Lister and Pratt,* 1959; *Black and Budd,* 1964; *Fujiwara and Endo,* 1971*; Rundle,* 1971*; Watanabe,* 1978]. Wind directions are marked when strong winds carve the snow into sastrugi, striking features that are elongated down the wind. During expeditions on the Antarctic plateau, scientists recorded the azimuth of sastrugi to map the wind. Precipitation rates were measured either using graduated stakes or by recording the snow stratigraphy: in both cases redistribution of snow by the wind introduced noise in the form of bedforms that made the process of measuring the annual accumulation more problematic.

Both *Cornish* [1914] and *Bagnold* [1941] recognized the strong parallels between bedforms in snow and sand. Indeed, these forms develop through largely similar transport processes, but the forms differ significantly in size, geometry, age, and the particles themselves are different. Sand dunes can reach 100 m high and be centuries old, whereas snow dunes are typically formed within a few hours, rarely last more than a few months, and hardly get higher than a meter. Also, snow particles have a density of 917 kg m^{-3} vs. 2650 kg m^{-3} for sand, a nearly 1:3 ratio. But the key differences between the two forms arise from the ability of snow particles to readily bond to each other. This process, called sintering [*Colbeck,* 1997; *Blackford,* 2007] will be shown to have great influence on the morphology of snow bedforms, and is largely absent in sand.

In this paper we review the existing literature on snow bedforms, describing individually each characteristic form, followed by a presentation of new quantitative descriptions of snow dunes and sastrugi based on laser scanning. We then use the new and old data to explore how the dynamics of snow dune formation are influenced by sintering in a simple mathematical model. Finally we introduce a new classification of snow bedforms based on both the forms and the physical conditions responsible for their genesis.

2.2 Snow Bedform Descriptions

Regardless of their shape and form, all snow bedforms arise from two basic transport mechanisms. These are *creep* and *saltation.* The wind can also move snow in suspension, but this plays little role in the development of bedforms. Creep consists of rolling snow grains at the surface of the snow that

were either entrained by shear stress due to the wind, or dislodged from their initial position by the impact of other entrained grains, and then moved by rolling and sliding. As explained in section 2.2.2, the bedforms called ripple marks are thought to specifically require creep in order to form. Saltation is the second mode of transport. In this mode, particles bounce off the snow surface and, once airborne, are swept downwind. Using snow traps, *Kobayashi* [1972] concluded that 80 to 90% of the moving snow was saltating at winds of about 10 m s^{-1}. He also provided the first photographs of saltating snow particles. They were found to follow trajectories similar to sand particles. Finally, *suspension* consists of snow particles entrained in the air by wind for which the upwelling forces exerted by wind outweigh the downward pull of gravity.

While little quantitative information exists, one important aspect of the overall snow transport phenomenon is that it is spatially and temporally variable on scales of meters and seconds. During a light blizzard it is easy to observe this heterogeneity. The saltating particles move in discrete streamers or sand-snakes. These streamers migrate laterally and pulse with the wind [*Schmidt*, 1986; *Baas and Sherman*, 2005; *Huang and Wang*, 2015], creating spatio-temporal variations in the transported load. Another phenomenon that creates variability in the transport process is wind gustiness, for which snow transport responds in a complex way [*Naaim-Bouvet et al.*, 2011].

The great importance of this spatio-temporal variability in transport during the creation of snow bedforms has not been sufficiently emphasized in the past. All bedforms are the product of both erosion and deposition, with the latter giving rise to the distinct yet subtle layering that characterizes both dunes and sastrugi. Under conditions of steady snow transport, distinct layers should not form, yet they do. We take their existence as widespread evidence that the constantly changing snow transport rates result in distinct layers or beds. This variability is responsible for some of the key shapes, sizes, and patterns we observe in snow bedforms, as we explore in more detail later.

Today, relatively few published descriptions of snow bedforms exist (~30), and these are mostly qualitative. In sharp contrast, a rigorous quantitative methodology exists for describing sand dunes [*Finkel*, 1959; *Sauermann et al.*, 2000] and many detailed descriptions of sand bedforms are available [*e.g. Pye and Tsoar*, 1990; *Tsoar*, 2001]. Where possible in what follows, we have applied these sand methods to our data.

The seven snow bedforms that have been widely recognized are (using their historical names): transverse dunes, barchans, whalebacks, ripple marks, crag and tails, pits, and a broad group of erosional features called sastrugi (Figure 2.1).
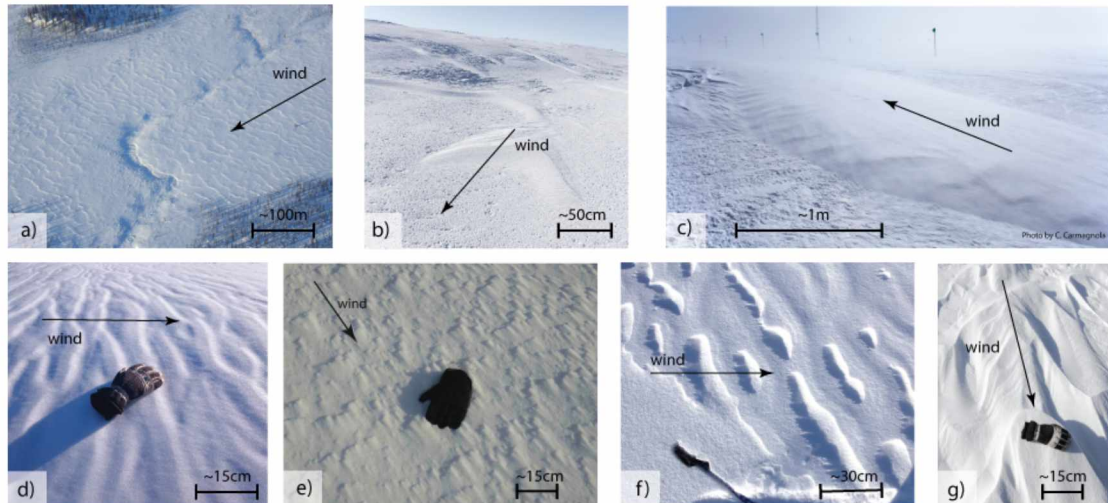
Figure 2.1: Photographs of typical bedforms encountered at the surface of the snow. The black arrow indicates the wind direction. a) snow-waves (transverse dunes) viewed from a plane, b) barchan dunes surrounded by small pits, c) a whaleback dune (photograph by C. Carmagnola), d) ripple marks, e) crag and tail features formed behind ice nucleus, f) pits with the handle of a ski pole for scale, and g) sastrugi (showing bedding or lamellae) with a glove for scale.

2.2.1 Dunes

A dune (Figures 2.1a and 2.1b) is a mound or a pile of snow deposited by the wind. In many cases the dune has a physical elongation either across the wind direction or parallel to it. It can be straight or sinusoidal in plan view, and while it obviously forms through wind and snow particle interactions, little is known about the initial inception process. Here we subdivide dunes into those transverse to the wind vs. those elongated parallel to the wind. We group snow-waves, which are similar to transverse dunes in sandy deserts [*Pye and Tsoar*, 1990; *Cooke et al.*, 1993], with barchans, as there appears to be a continuum between these two forms. Whaleback dunes stand on their own as the conditions that lead to their formation differ from those producing other types of dunes.

There is one other unique type of snow dune: the mega-dune. Mega-dunes are found on the high plateau of Antarctica [*Fahnestock et al.*, 2000; *Frezzotti et al.*, 2002a; *Frezzotti et al.*, 2002b] and have wavelengths of several kilometers. Their genesis involves erosion and saltation as with regular dunes,

13

but also sublimation and recrystallization of snow grains. Because the time scale at which they migrate (few meters per year) and their large size (few kilometers) differs so significantly from the other type of dunes we present here, we do not address them further in this paper.

2.2.1.1 Transverse Dunes

A dune is said to be transverse (Figure 2.1a) when its long dimension lies across the wind direction. "Classic" transverse dunes are called snow-waves because of their resemblance to ocean waves. Despite the fact that some barchans can be longer down the wind direction than across, they are also cataloged as transverse dunes because they form under similar wind conditions. The key difference is that barchans are constrained in their growth by a limited amount of mobile snow particles, while snow-waves are not. In fact, as the snow supply in a snow-wave field decreases, the snow-waves break apart into barchans, and when the snow supply increases in a barchan field, the barchans begin to link up across the wind and form snow-waves [*Dobrowolski*, 1924; *Moss*, 1938]. Similar behavior is also observed for sand barchans, though on much longer timescales [*Werner*, 1995; *Baas*, 2007; *Kocurek et al.*, 2010].

2.2.1.1.1 Snow-waves

Cornish [1902] reported the first observations of snow-waves, noting that they formed during snowfall at moderate (13 m s^{-1}) wind speeds, were usually found on flat surfaces like lake ice, and did not require the presence of obstacles for their inception (Table 2.1). *Kobayashi and Ishida* [1979] observed snow waves forming in Japan at wind speeds ranging from 7 to 15 m s^{-1} at a height of 1 m above ground. Typically snow-waves range from 5 to 20 cm in height and have wavelengths (crest to crest) ranging from 3 to 15 m. They propagate downwind at speeds ranging from 2 to 10 cm min^{-1}. The latest report of snow-waves comes from *Mattsson* [2007], who observed snow-waves forming on a Swedish farm. His results corroborate the earlier observations in terms of metrics and formation conditions (Table 2.1).

Table 2.1: Snow-wave Metrics from the Literature

Authors	Wavelength (m)	Height (m)	Dune Propagation Velocity (cm min⁻¹)	Wind (m s⁻¹)	Temperature (°C)	Location
Cornish [1914]	9.2 ± 2 10 ± 3.7 4.8	0.18 0.13	- - 5.1	- - 13.4	- - -22	Canada
Kotlyakov [1966]	10 -15	< 2.5	-	-	-	Antarctica
Kobayashi and Ishida [1979]	3 - 15	0.05 - 0.2	2-10	< 15	-	Hokkaido, Japan
Mattsson [2007]	< 10	-	-	10	-1	Sweden

The scarcity of published snow-wave observations (total of 4) suggests to us that they can form only under a narrow range of conditions. Indeed, in all published cases, the observations were made right after a significant snowfall that was followed by a wind event: more than 8 cm of fresh snow for *Cornish*, 10 cm or more for *Kobayashi*, and few tens of cm for *Mattson* (no data for *Kotlyakov* [1966]). Three of the four reports are from temperate regions. It seems the necessary conditions are a) a significant snowfall (less likely in non-temperate regions), b) wind immediately following the snowfall, c) low enough temperatures to prevent snow clumping or melting, and d) a flat, open area. This combination must occur relatively infrequently especially in polar regions because of the scarcity of precipitation.

Kobayashi [1980]'s work provides deeper insight into the linkage between the turbulent flow of the wind over the snow-wave field and the snow-waves themselves. He found that the spatial scale of turbulent eddies and the wavelength of snow-waves were of the same size for a given wind speed. He concluded that as wind speed increases, the spatial scale of the turbulences decreases, along with the distance from one snow-wave crest to the next. His data suggest that at wind speeds of 15 m s⁻¹, and greater, snow waves disappear because the turbulent eddies approach a scale length of zero.

2.2.1.1.2 Barchan Dunes

Barchan dunes (Figure 2.1b) are crescentic shaped mounds with a tail directed upwind and two horns pointing downwind. *Moss* [1938] described their shape as an *arrowhead* pointing into the wind, while *Lister and Pratt* [1959] suggested they took the shape of a *laundry iron* (Figure 2.2a). Barchans form in sand as well as in snow and have been extensively studied on both Earth and Mars [*Cutts and Smith*, 1973; *Bourke*, 2010]. Their distinctive shape and apparent self-organizing property [*Werner*, 1995; *Baas*, 2007; *Werner*, 2003] have fascinated geomorphologists [*Cornish*, 1902; *Bagnold*, 1941; *Finkel*, 1959] and planetary scientists [*Iversen et al.*, 1975; *Bourke*, 2010; *Lorenz*, 2014] for years. *Cornish* [1914] was the first to note that snow barchans are flatter and smaller than sand barchans. The former are typically from 3 to 20 m long and between 5 to 12 m wide (Table 2.2), but only 0.1 to 0.5 m tall, while the latter can easily be 10 m high, 100 m wide and 150 m long. The largest snow barchans of which there is any record [*Kobayashi*, 1980; *Goodwin*, 1990] may have been as much as 2 m tall, but such large barchans must be extremely rare, as we have neither seen nor heard of any others having seen such large features. Barchans, like snow-waves, propagate downwind at speeds ranging from 1.5 to 6.6 cm min^{-1}, with small barchans moving faster than bigger ones [*Kuznetsov*, 1960]. Some very high propagation speeds (10 to 17 cm min^{-1}) have been reported by *Hargitai* [2013] based on webcam measurements made in Hungary in winds of 11 to 15 m s^{-1}.
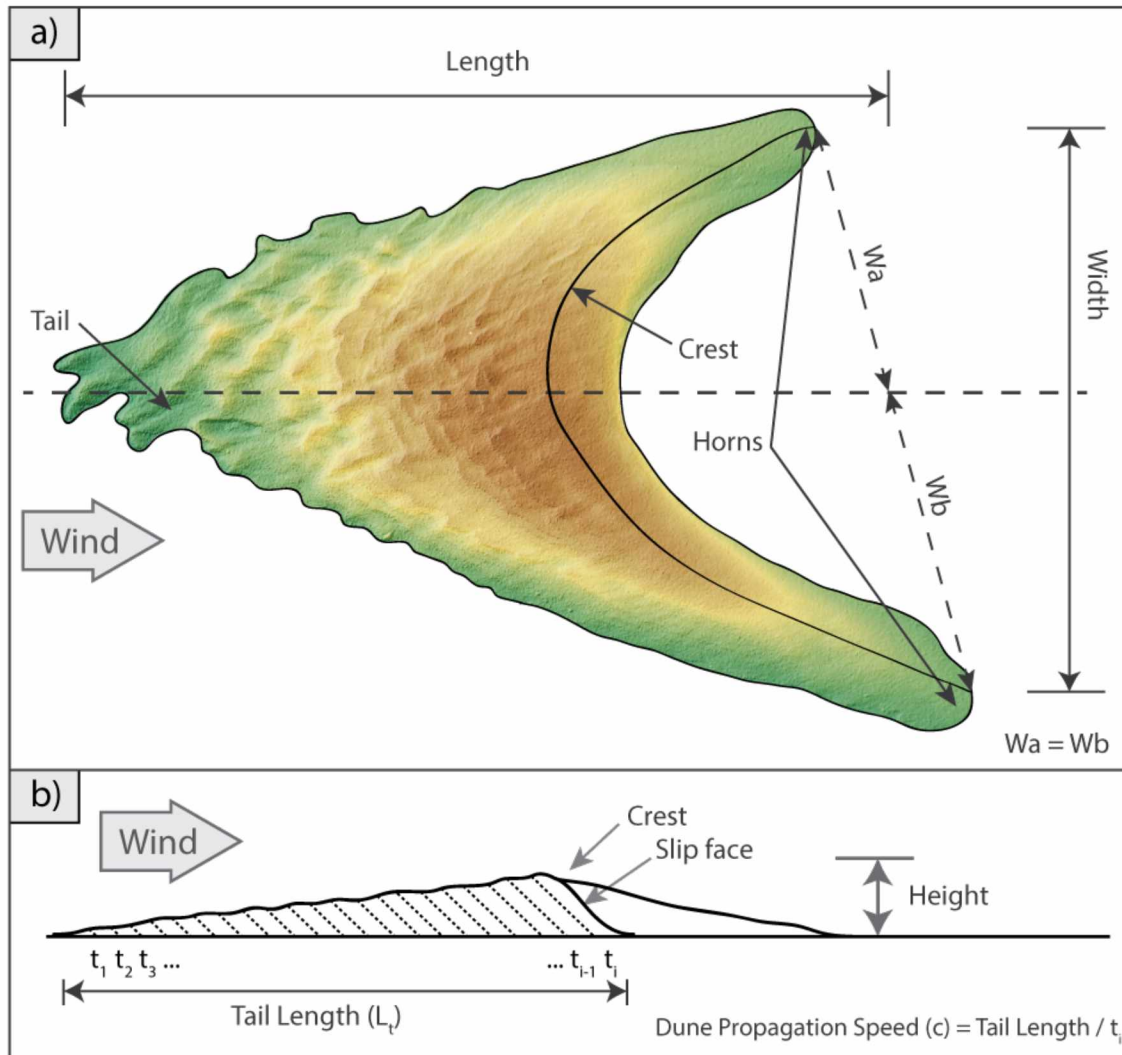
Figure 2.2: The morphology of a barchan from a lidar scan showing how the width, length, and height are measured. a) Plan view of a barchan showing the primary and secondary features. The coloration corresponds to the surface height, with green indicating low and brown indicating high areas. b) Vertical cross section along the longitudinal axis of the barchan shown in (a). Dotted lines indicate the idealized internal stratigraphy created by the deposition of fore-set beds on the slip face. Deposited layers are oldest on the tail, youngest at the current slip face. The gray arrows indicate the wind direction.

Table 2.2: Barchan Metrics

Authors	Length (m)	Width (m)	Height (m)	Propagation Speed (cm min⁻¹)	Slip face angle (°)	Wind speed (m s⁻¹)	Temperature (°C)	Location
Moss [1938]	3-5	10-12	-	0.22 – 2.23[a]	-	≤ 10	-	NE Greenland
Kuznetsov [1960]	10-25	5-8	0.3-0.5	1.5-2.5	-	13-15	-12	Mirny Station, Antarctica
Benson [1962]	-	-	-	1.67	-	-	-	Greenland
Kotlyakov [1966]	Several tens of meters	-	≤ 1	2.5-4.2	40-60°	13-15	-12	Antarctica: coastal and inland
	-	-	-	6.6	-	18	-	-
	-	-	-	1.5	-	-	-	Victoria land
Doumani [1967]	-	-	≤ 1	3.3	30	-	-50	-
	-	-	-	3	-	11	-	
Kobayashi and Ishida [1979]	-	-	0.3-2	1.5	-	-	-	Antarctica
Goodwin [1990]	-	-	< 2	-	-	-	-	Antarctica
Warren [1992] (personal communication)	-	-	-	-	-	10	-50	South Pole, Antarctica
Birnbaum et al. [2010]	8 ± 3	4 ± 2	0.2 ± 0.1	few	-	> 10 at 2m high	-	Antarctica
This study Field 1 Field 2 Field 3	5.8± 1.4 4.1 ± 1 7.6 ± 2.3	2.5 ± 0.9 2.4 ± 0.8 2.8 ± 1.3	0.08 ± 0.02 0.05 ± 0.02 0.16 ± 0.05	- - -	≤ 15° ≤ 15° ≤ 46°	- - -	- - -	Alaska, North Slope

[a] *Moss* [1938] gives dune propagation speed in cm s⁻¹, which we ought to think mistaken for cm min⁻¹

The morphology of a barchan consists of a gentle slope facing the wind rising from the tail to the crest. Particles are eroded from this surface, cascade over the crest, and fall down the steeper lee-side slope (slip face) where they are deposited (Figure 2.2b). The windward side of a barchan often develops secondary erosional features resembling flutes and scallops similar to those found in rocks [*Allen*, 1971; *Richardson and Carling*, 2005]. However, in snow these features are oriented in the opposite direction with regard to the wind: the steep entry to the flute is actually on the downstream end of the feature in snow. These secondary erosional features were described by *Moss* [1938] who suggested that they form when wind erosion accentuates the slight variations in hardness between deposition layers. Later these incipient differences are transformed into a regular pattern of pits and sharp-edged sastrugi. Remnants of these carved-up tail forms can often be seen with little else of the initial barchan remaining, suggesting the tails are more resistant to erosion than the crests. In fact, *Kuznetsov* [1960] tested the hardness of the snow surface along a barchan profile while the barchan

was still moving, and found the crest to be much softer than the tail. This is a salient observation for understanding the processes that lead to the formation of both barchans and sastrugi (Section 2.4).

Most observations of barchans have been reported from Antarctica and Greenland [*Moss*, 1938; *Kuznetsov*, 1960; *Budd et al.*, 1966; *Kotlyakov*, 1966; *Doumani*, 1967; *Goodwin*, 1990; *Birnbaum et al.*, 2010] (Table 2.2) where snow precipitation is low, and large flat open landscapes are common. There, barchans typically form when cyclonic winds transport newly fallen snow [*Kuznetsov*, 1960]. As with snow-waves, the range of conditions necessary for barchan formation appears to be quite limited, and the number of direct observations of their formation is equally low. In our combined 40 years of experience working in wind-blown snow areas, we have only directly seen barchans forming three times. Winds of about 8 to 20 m s^{-1} appear necessary, with higher wind speeds (typical of katabatic winds in Antarctica) disintegrating the barchans [*Kuznetsov*, 1960]. If the snow supply increases (i.e. it begins to snow) at a constant wind speed, the barchans transform into snow-waves [*Dobrowolski*, 1924]. In short, there seems to be a delicate balance between wind speed and snow particle flux outside of which barchans will not form.

2.2.1.1.3 Whaleback Dunes

Whaleback dunes are bedforms appearing under winds greater than 15 m s^{-1} [*Kuznetsov*, 1960; *Kobayashi*, 1980]. They are greatly elongated domes, parallel to each other and to the direction of the wind (Figure 2.1c). Commonly, they are 20 to 50 m long but can reach as much as 150 m. They are 1 to 3 m wide, and their heights range from 0.3 to 2.5 m [*Lister and Pratt*, 1959; *Kotlyakov*, 1966; *Goodwin*, 1990]. The few published descriptions of whaleback dunes come from Antarctica, where they have only been observed after their formation, probably because during the extreme weather in which they form a human observer would have trouble observing anything.

To illustrate their formation, the whaleback shown in Figure 2.1c formed at Summit Station, Greenland on June 4th, 2011 at a mean wind speed of 15 m s^{-1}, but with gusts reaching 21.8 m s^{-1}. The authors have also observed the presence of such features in the Arctic, where they are known to the Inupiaq as "qimuagruk", which also means whaleback [*Sturm*, 2010]. To our knowledge, no other type of depositional form has been reported in association to such strong winds.

2.2.2 Ripple Marks

Ripple marks (Figure 2.1d) are small wave like features that form transverse to the wind. Typical snow ripple marks have wavelengths ranging from 5 to 20 cm and amplitudes of 0.2 to 2 cm. Like dunes, they propagate downwind, moving at 0.5 cm min^{-1} or more [*Cornish*, 1914; *Kotlyakov*, 1966; *Kobayashi and Ishida*, 1979; *Kosugi et al.*, 1992]. Like barchans the lee slope of a ripple mark is shorter and steeper than the windward slope.

The formation of snow ripples is similar to sand ripples and requires a fine balance between creeping and saltating particles (Figure 2.3). When particles saltate, they impact the snow surface and dislodge resting particles. Fine particles are ejected upward and become entrained by the wind, flying downwind on a parabolic trajectory. Coarse particles are also impacted, but being too heavy to bounce upward, they remain at the surface and move downwind by creep. When the wind speed is 5 to 7 m s^{-1} [*Kosugi et al.*, 1992] both saltation and creep occur and ripples form by differential motion of the fine and coarse grains. When the wind speed drops below 5 m s^{-1} insufficient momentum is transferred to the larger particles to initiate creeping. When the wind becomes too strong, all the particles saltate and none creep, destroying any existing ripples and making a flat smooth surface [*Bagnold*, 1941; *Pye and Tsoar*, 1990].
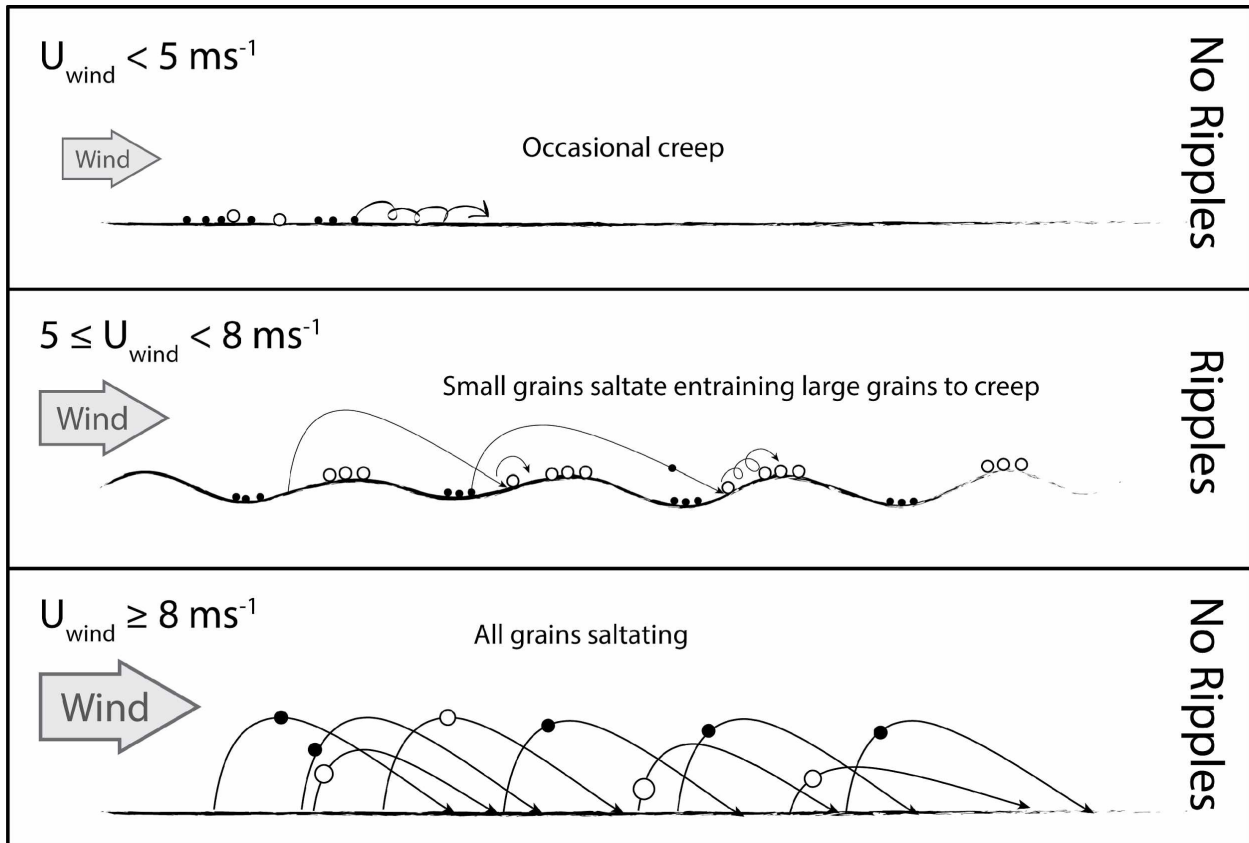
Figure 2.3: Two transport modes of snow particles by wind: creep and saltation. When both take place, ripple marks can form.

The key observation that supports differential movement as the genesis of ripple marks is that the coarse grains are found at the ripple crests [*Bagnold*, 1941]. These have been pushed uphill by impacts from the finer saltating particles. The fine particles lie in the troughs, where they are shielded from being dislodged by other saltating particles. For example, from an initial snow bed of particles averaging 0.42 mm in diameter, *Kosugi et al.* [1992] found that after wind transport the averaged particle size on the crest was 0.64 mm, whereas the particle size in troughs was similar to the initial grain size. They proposed these relationships between wind speed (U in m s^{-1}), ripple wavelength ($\square$ in cm), and height (h in mm):

$$\lambda = 4.1U - 13.2 \qquad \text{and} \qquad h = 0.92U - 1.5 \qquad (2.1)$$

They also found a power law relating the ripple propagation speed (V in cm/min) to the wind speed (U in m/s):

$$V = 2.4 \times 10^{-3} U^{4.1} \qquad (2.2).$$

21

Fujiwara and Endo [1971] and *Doumani* [1967] have described a Y-shaped ripple mark that is only found in snow. Based on their photographs, these Y-ripples are equivalent to normal ripple marks in size, but nothing is known about why, how, and under what conditions they form.

2.2.3 Crag and Tails

Another feature commonly encountered in early winter or on rough snow surfaces are crag and tail features (Figure 2.1e). They are also referred as scour marks by *Allen* [1965]. They consist of small and elongated drifts forming in the lee of fixed micro-relief (Figure 2.4). Their genesis differs significantly from other forms described above because a hard nucleus, not necessarily made of snow, is required for their formation. *Dobrowolski* [1924] referred to them as forced dunes. Crag and tail features commonly form during snowfall under light winds, often on top of a hard snow surface. When the nucleus is small and made of an ice pellet or a hard ball of snow, the blowing snow particles accumulate in the lee of the hard ball, and a small erosion scour forms upwind and around the sides of the nucleus [*Allen*, 1965] (Figure 2.4). At larger scales these features can be encountered behind tussocks or rocks.
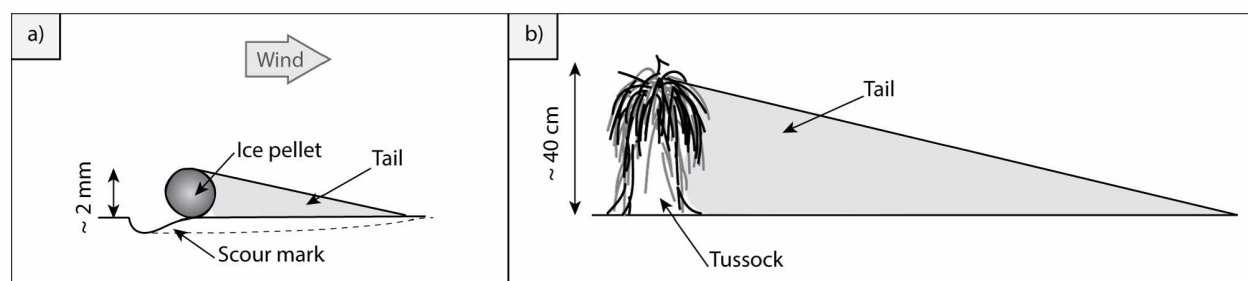
Figure 2.4: Two cases where obstacles create crag and tail forms. a) An ice pellet acts as an obstacle and a tail of snow deposits behind it; a scour mark forms in front and around the ice pellet [*Allen*, 1965]. b) A tundra tussock nucleate a long tail of snow in its lee.

2.2.4 Pits

Snow surfaces in windy regions exhibit some smaller bedforms that have been photographed but not measured. Among them are pits (Figure 2.1f), which are small dimples or cup-shaped depressions in the snow surface. They typically form when there is a thin crust that is slightly harder than the underlying snow. Slight variations in snow hardness drive the shaping of the pits [*Dobrowolski*, 1924; *Doumani*, 1967]. Typically, the downwind pit slope is steeper than the upwind

slope. As with other bedforms, the pits propagate downwind about 1 cm min^{-1} [*Dobrowolski*, 1924; *Kobayashi*, 1980]. *Doumani* [1967] suggested that pits are the inception phase of the erosional features like sastrugi.

2.2.5 Sastrugi

The current usage of the term *sastrugi* describes a bewildering array of forms resulting from snow erosional processes carving into wind packed snow [*Kotlyakov*, 1984; *Leonard*, 2009]. In the past, this term has also been used to designate erosional shapes in warm deserts, but today the term is limited to snow [*Blackwelder*, 1930] and the related sand features are called yardangs [*Goudie*, 2007]. The main erosional process for both yardangs and sastrugi is the abrasion of a cohesive material by the bombardment of particles entrained by wind. However, because yardangs last for decades, if not centuries, and can also be tens of kilometers long, so additional formation processes such as cracking and weathering are important in their formation, but play no role in the formation of snow sastrugi.

Kotlyakov [1984] defined sastrugi as having steep slopes facing the wind and gentle slopes downwind that form sets of furrows. One of the main geometrical traits of sastrugi is the intersection of curved surfaces (furrows) into sharp edges (Figure 2.1f). These surfaces have also been described as grooves, scallops, and flutes. The most advanced forms of sastrugi are the lanceolate sastrugi, also referred as anvil heads, which have a cantilever and undercut point oriented into the wind [*Doumani*, 1967]. If the point protrudes far enough, it will deform and bend downward under its own weight.

Because the morphology of intersecting grooves, flutes and ridges is complex and diverse, unlike dunes, no simple way of measuring sastrugi has been suggested, other than referring to their general height and alignment. In general the features are about 0.3 to 0.5 m high, with exceptionally large sastrugi being 2 m high [*Kotlyakov*, 1966; *Doumani*, 1967; *Kotlyakov*, 1984; *Goodwin*, 1990]. As we discuss later, it is not a coincidence that the maximum height is the same as the exceptionally large snow dunes.

Sastrugi form when an unsaturated flux of saltating snow particles erodes layers of hardened wind slabs [*Kotlyakov*, 1966]. The snow being eroded must reach a critical hardness so that it can resist

large-scale entrainment in the saltation flux, yet still be soft enough to be eroded locally. Thick layers of snow of similar hardness in "wind-exposed" locations are necessary for sastrugi formation, conditions easily met after the formation of a snow dune.

Watanabe [1978] sectioned two sastrugi in Antarctica. He found regularly spaced bedding within the sastrugi. The authors have tried a similar approach to detect layering in sastrugi in the Arctic, but despite trying multiple methods to enhance the bedding, such as brushing, powder paint, near-infrared photography [*Tape et al.*, 2010] and sun backlighting, we have not been able to reproduce *Watanabe*'s results. The only hint of such bedding has been seen on the tails of old barchans, where wind erosion has exposed thin layering due to slight differences in hardness (Figure 2.1f). *Harder et al.* [2000] also sectioned two sastrugi, but for measuring the spatial variation of non-sea-salt sulfate (nss-SO_4) concentration. They found a significant decrease of SO_4 concentration from the nose (windward) to the tail of the sastrugi, highlighting the effect of wind pumping through the snow.

There is a class of rock bedforms that has a superficial similarity to sastrugi. These are the flutes and scallops that form underwater [*Allen*, 1971; *Richardson and Carling*, 2005] on rock surfaces. Unlike yardangs and sastrugi, however, these flutes and scallops form by the dissolution of the substrate. For example, *Allen* [1971] describes flutes forming underwater in gypsum. Because of the turbulent flow of the fluid boundary layer, the initial uneven dissolution of the bed emphasizes itself by modifying the flow of water into stationary fluvial vortices that further dissolve the rock. The resulting shapes can be described using the same terminology as for sastrugi, despite the difference in formation processes. The similarity suggests that perhaps stationary wind eddies, and some feedback between the snow forms and the eddies, is involved in sastrugi formation.

2.3 Bedform Morphology Using a Laser Scanner

2.3.1 Data Collection Method

The current lack of quantitative data or metrics for the various snow bedforms reflects the lack of a tool that could be used to collect data on complex shapes. Now, however, it is possible to use laser-scanning technology to produce detailed three-dimensional models of real snow surfaces [*Prokop*, 2008; *Deems et al.*, 2013].

In April 2012, 2013, and 2014 we scanned 9 tundra snow sites [*Sturm et al.*, 1995] on the North Slope of Alaska, USA (Table 2.3). We used a Leica ScanStation C10 scanner. Of the 9 sites, 6 had what we designate as compound surfaces (superimposed bedforms of several types) and were heavily eroded, but 3 sites presented discrete and recognizable individual forms, specifically barchan dunes.

Table 2.3: Laser Scanning Sites

Site Name	Date	Location (lat/long)	Number of Scan	Substrate Type
Field 1	April 19th, 2013	68.63/-149.61	4	Lake ice
Field 2	April 22nd, 2014	68.61/-149.56	3	Tundra
Field 3	April 17th, 2013	69.84/-148.78	3	Lake ice
Field 4	April 16th, 2013	69.61/-148.65	4	Tundra
Field 5	April 17th, 2013	69.84/-148.77	4	Tundra
Field 6	April 15th, 2012	69.61/-148.65	4	Tundra
Field 7	April 16th, 2013	69.58/-148.64	4	Lake ice
Field 8	April 18th, 2013	69.84/-148.77	3	Tundra
Field 9	April 16th, 2012	69.58/-148.64	3	Lake ice

At each site, a snowmobile was used to delineate a plot of 50 to 70 m diameter. We then successively installed and leveled the laser scanner at multiple positions along the track on a surveying tripod resting on hard frozen ground. The scanner positions were spread to the four quadrants or three trisects of the site in order to minimize occlusion of the laser and improve the 3D reconstruction of the rough snow surface. Scans from each plot were combined together to ultimately generate a digital elevation model (DEM). The scan of a complete site could be executed within a couple hours during which the snow surface remained unchanged: no data were acquired in windy and saltating conditions. In all cases, the bedforms had already formed when we arrived at each site, so we had no direct information on their formation process.

The DEM was produced from the laser output point cloud, a collection of points where each point represents one range measurement located in space by a distance from the laser scanner sensor, an azimuth, and a vertical angle [*Deems et al.*, 2013]. Hence, each point had spatial coordinates that could be converted into a Cartesian framework (XYZ), where the X-Y plane is horizontal and Z is the local vertical elevation.

2.3.2 Post-Processing Method and Accuracy

The raw point clouds produced by the scanner were co-registered using a set of tie points obtained from 4 fixed reflectors located on the outer part of each scanned area. The software Cyclone (http://hds.leica-geosystems.com/en/Leica-Cyclone_6515.htm) automatically co-registers the point clouds from the different scanner positions into one larger point cloud containing all the data for one site. These global point clouds were then cleaned manually of large unwanted scanned features such as snowmobiles, human bodies, poles, and other artificial equipment. These combined point clouds were then imported in the software CloudCompare (www.cloudcompare.org) to be subsampled and exported as DEMs in raster files. We chose a pixel resolution of 4 cm as a fair compromise between high spatial resolution and maximizing the number of points within each pixel.

As an assessment of the vertical error associated with our data, we derived the vertical spread of points per pixel. Ninety-five percent of all pixels had a vertical spread of less than 6 mm and 99% had a vertical spread less than 14 mm. This vertical spread was uncorrelated with the number of points per pixel and remained constant even as the distance from the scanner increased, indicating no laser shot angle dependence. The spread values include the effects of real micro-terrain roughness, some measurement error, and some light penetration into the snow.

We examined the errors associated with light penetration. The scanner is a green laser (532 nm wavelength) that can penetrate into the snow surface. Various measurements of the extinction coefficient for the 500 nm wavelength in snow provide a wide range of possible values for this penetration. They range from 0.06 cm^{-1} for fresh snow [*Perovich*, 2007] to 0.2 cm^{-1} for denser Arctic snow [*Grenfell and Maykut*, 1977]. Applying the Bouguer-Lambert law with a coefficient of extinction of 0.2 cm^{-1} leads to a penetration depth of 3.4 cm for 50% attenuation. However, this is the penetration along a laser light ray path, which in the scanning geometry is often close to horizontal. Consequently, 3.4 cm is a gross over-estimate of the potential light penetration error. Moreover, if we were suffering light penetration of this magnitude, we would expect to see a strong angular dependence, with the largest errors nearest the scanner. Instead, we found no trend in vertical spread with incident angle. We believe the 5 to 14 mm spread per pixel is a more accurate estimate of the true vertical errors in our bedform DEMs.

As the final stage of analysis, information about bedforms was extracted and analyzed from the DEM files using the open-source software project R (www.r-project.org) and the geographical information system software QGIS (www.qgis.org).

2.3.3 Snow Surface Metrics

2.3.3.1 Morphology of Barchans

We used the methods of *Sauermann et al.* [2000] and *Andreotti et al.* [2002] for measuring barchan geometry (Figure 2.2). Height was derived by subtracting the substrate base elevation from the elevation of the highest point of the dune. Where the substrate had local slope, the entire point cloud was de-trended by fitting a plane to the substrate, then forcing the plane to be horizontal. Barchan width and length were calculated after picking three characteristic points: the tail and the two horn extremities. The length was computed as the distance between the tail and the midpoint between the two horns. The width was taken as the distance separating the two horn extremities perpendicular to the direction of the length measurement. We define the axis of the barchan as the line along which we measure its length, though this may not coincide exactly with the wind direction.

Only the barchan fields in which the dunes were distinct and separate (Figure 2.5) were analyzed. Field 1 was located on a frozen lake. Field 2 was located in rolling hills covered by tundra, and Field 3 was located on a frozen lake in the coastal plain about 60 km south of the Arctic ocean (Table 2.3). Our results are compared to earlier measurements of barchans in Table 2.2. There were some distinct differences between our samples and ones reported in the literature, as well as between our three fields. Barchans from Field 1 and 2 had statistically equal means and variances for their width and height distributions, but the barchans from Field 1 were longer by 1.66 m on average. We also found that barchans from Field 3 were about 10 cm taller for a given length than for the other fields, and these bigger dunes had steeper lee sides ($\leq 46°$). The standard deviations of the barchan axes within each field were within $\pm 5°$ of the mean, suggesting fairly stable wind directions across the fields.
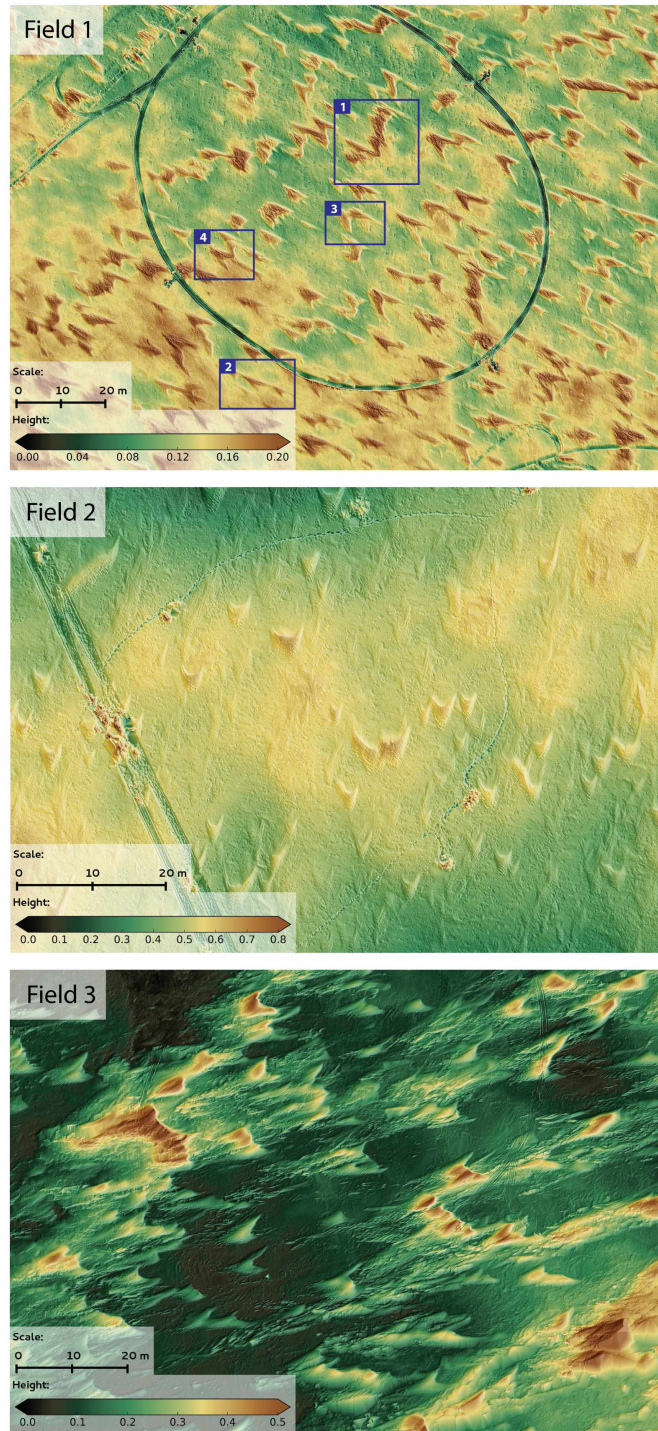
Figure 2.5: Overview of the three fields of barchan we measured. The horizontal scales and the color bars are different in each panel. The tracks are from snowmobiles. The numbered blue boxes (Field 1) appear in detail in Figure 2.10. The three fields have 4 cm horizontal resolution and a vertical accuracy estimated at $\pm$ 1.4 cm. All units are in meter.

The ratios of width:length:height of sand barchans have been shown to be invariant with barchan size [*Sauermann et al.*, 2000; *Andreotti et al.*, 2002], and we found similar results for snow barchans (Figures 2.6, 2.7 and 2.8). Because sand barchans are larger than snow barchans, we divided all of the reported sand dimensions by 10 in order to plot all data together. We found statistically significant correlations for the snow barchan measurements (Table 2.4). From Figure 2.8, we can see that snow and sand barchan footprints (width: length) are similar, and for all sand and snow data the slope relationships are equivalent as well (Figure 2.8). However, as *Cornish* noted 113 years ago, snow barchans are flatter than sand barchans, with a height to length ratio of 1:70, and a height to width ratio of 1:55 as compared to 1:15 and 1:11 for sand. On the other hand, the barchans from Fields 1 and 2 present equal proportions between their footprint and their height. All of the snow barchans had windward slope angles of between 2° and 6°. Field 1 and 2 had barchans with lee slopes ranging from 9 to 13°, whereas the barchans in field 3 had slopes of 30° on average.
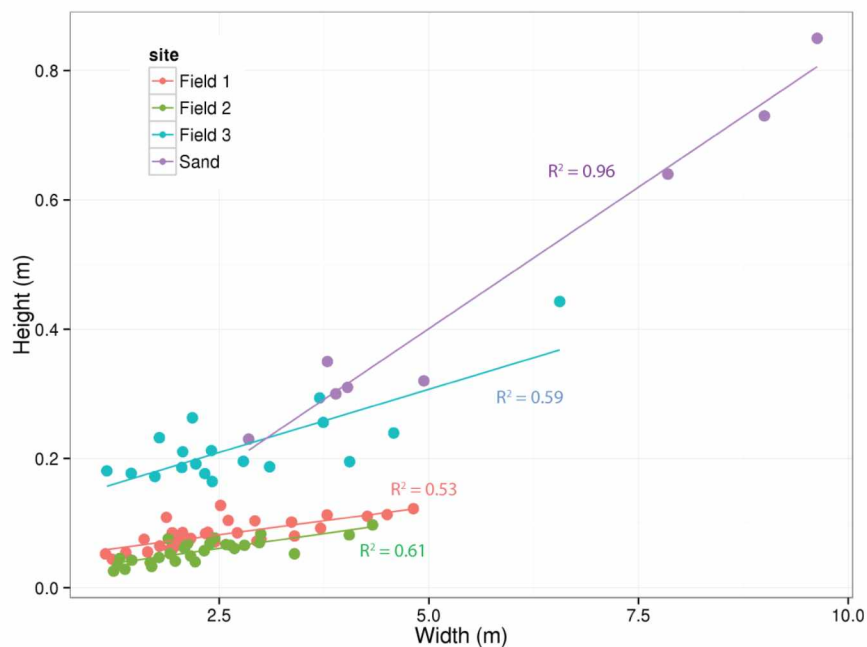
Figure 2.6: Relationship between width and height of barchans for Field 1 (red), Field 2 (green) and Field 3 (blue), and sand (purple). Pearson's correlation coefficients indicated for each field. Dimension of sand dunes have been divided by 10 for easier comparison with snow dunes.
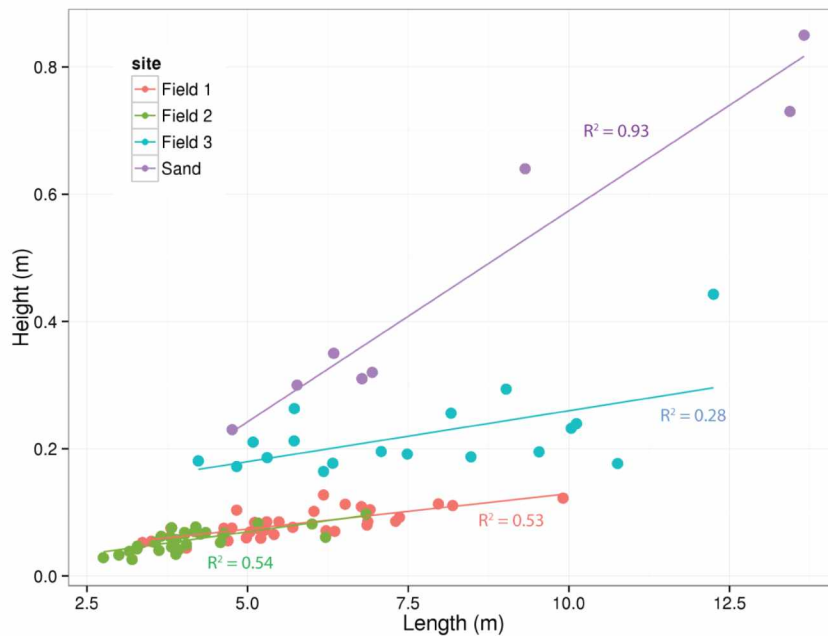
Figure 2.7: Relationship between length and height of barchans for Field 1 (red), Field 2 (green), Field 3 (blue), and sand (purple). Pearson's correlation coefficients indicated for each field. Dimension of sand dunes have been divided by 10 for easier comparison with snow dunes.
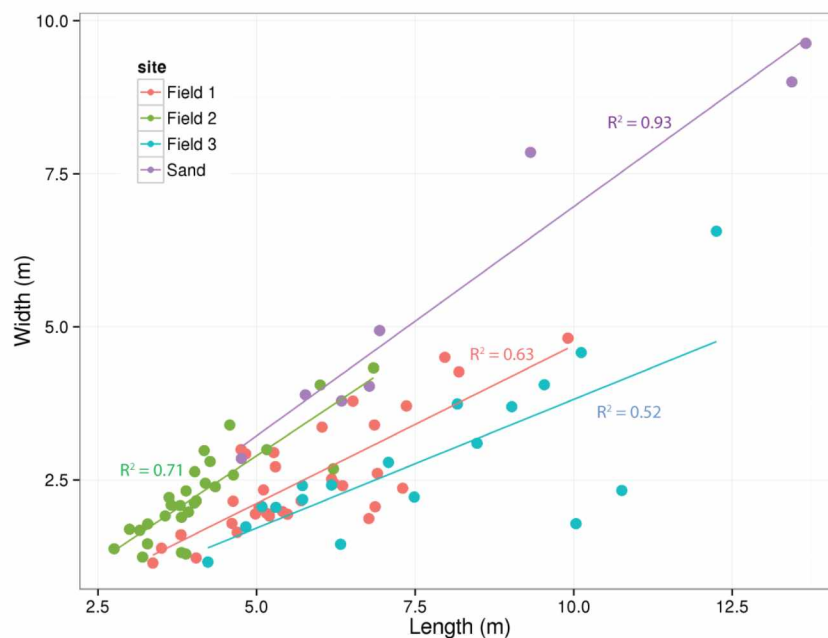
Figure 2.8: Relationship between width and length of barchans for Field 1 (red), Field 2 (green), Field 3 (blue), and sand (purple). Pearson's correlation coefficients indicated for each field. Dimension of sand dunes have been divided by 10 for easier comparison with snow dunes.

Table 2.4: Snow and Sand Barchan Morphology Relationships.

Variables	Field name	Linear fit[a]	R^2	P-value
Width ~ height	Field 1	$32h - 0.09$	0.53	10^{-6}
	Field 2	$34h + 0.45$	0.56	10^{-6}
	Field 3	$16h - 0.68$	0.59	10^{-4}
	Field 1 & 2	$25h + 0.71$	0.44	10^{-9}
	Sand	$11h + 5.8$	0.96	10^{-6}
Width ~ length	Field 1	$0.52L - 0.46$	0.63	10^{-8}
	Field 2	$0.76L - 0.77$	0.83	10^{-11}
	Field 3	$0.42L - 0.39$	0.52	10^{-4}
	Field 1 & 2	$0.42L + 0.31$	0.52	10^{-11}
	Sand	$0.74L - 5.71$	0.93	10^{-5}
Length ~ height	Field 1	$49h + 1.8$	0.53	10^{-6}
	Field 2	$40h + 1.9$	0.54	10^{-6}
	Field 3	$20h + 3.2$	0.28	0.014
	Field 1 & 2	$51h + 1.4$	0.67	10^{-15}
	Sand	$14h + 17.8$	0.93	10^{-5}

[a] Intercept of the linear fits are expressed in meters

2.3.3.2 Morphology of Sastrugi

Sastrugi are the most ubiquitous and common of all the snow bedforms, but the least studied. In an informal canvas of hundreds of photos of tundra snow taken over dozens of years, all the other snow bedforms appear rarely or intermittently, with barchans and snow-waves appearing in only a fraction of cases, but sastrugi are present in virtually every photo. Later we present an explanation for this prevalence, but we want to emphasize here that sastrugi deserve more attention.

For measurements, we focused on the sharp ridges that characterize sastrugi. We traced these manually from our laser-scanned DEMs (Figure 2.9) in order to accentuate the spatial pattern of these ridges, their orientation with respect to the wind, their length, and the nature of their terminations (cusps, scallops, flutes etc.). We found a heterogeneous distribution with zones of dense sastrugi interspaced with exempt zones where there were few or no ridges. These latter areas appear to be downwind of remnant barchan tails, the remnants having apparently created a wind shadow that resulted in a sastrugi-free zone. Where sastrugi are present, we found two types of traces: 1) *prow and scoop combinations*, and 2) *patterned tail markings*.

The former (*prow and scoop*) consists of sets of parabolas, some opening away from the wind and others opening into the wind. The latter (*patterned tail markings*) create an *en echelon* series of parallel lines. Physically, the parabolas delineating the prows define a leading edge, or front line, of the erosional forms. In some cases these parabolas outline lanceolate sastrugi. Extending downwind

from this front line, ridge traces either dissipate or extend and connect to scoop traces, which mark flutes. In combination, the prows and scoops essentially define sastrugi, though many sastrugi have no flute terminations, instead dissolving in flat snow surfaces. The vertical relief of the front lines facing the wind range from 2 to 15 cm for the field shown in Figure 2.9. These front line ridge segments were typically 0.25 m to a few meters wide perpendicular to the wind, while the flute ends did not exceed 0.5 m width.
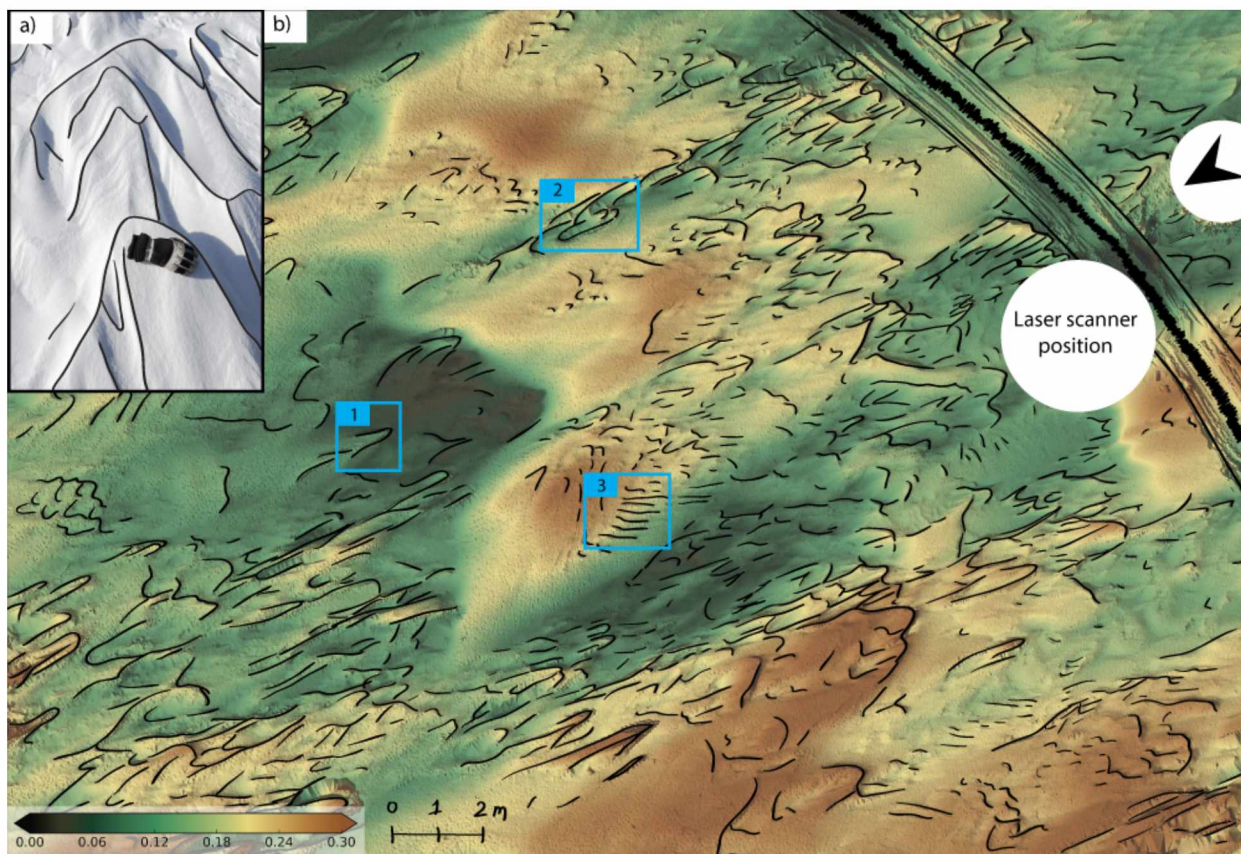
Figure 2.9: Plan view of traced sastrugi ridges. The inset photo suggests what has been traced where all the edges of sastrugi have been delineated. The background color in the main figure indicates the relative elevation (see the color-scale bar). The wind direction responsible for the sastrugi is indicated in the upper right corner, next to the snow mobile tracks. Blue box 1 is an example of a prow/anvil head sastrugi, box 2 presents a typical scoop field, and box 3 shows typical *en echelon* pattern. All units are in meters.

The second type, patterned tail markings, were first observed and sketched by *Moss* in 1938. They seem to be present on most snow barchans but absent on sand barchans. The traces of these features form oblique angles to the main wind direction, and generally originate from the sastrugi outer edge and trend inward and downwind toward the slip face. The markings can be on one or both sides of the midline of the barchan (or what remains of the barchan). When the markings are

on only one side, they form an en echelon pattern, but if they are on both sides and intersect, then a harlequin pattern is produced. The *en echelon* spacing of the traces is almost an order of magnitude larger than the thickness of the foreset bedding that produces the lamellae described in Section 2.2.1.1.2 and shown in Figure 2.2b, though closer scrutiny of the DEMs and photos indicate that this finer, lower relief bedding is also present. This finer bedding is mostly visible close to barchan crests where the erosion has been minimal; the coarser, more widely spaced markings become more prominent towards the tail of the barchan. We discuss the significance of these traces of patterned tail markings in more detail shortly.

2.3.4 Bedforms and Surface Dynamics

Despite the fact that our DEMs are static and that we only visited sites once, we can deduce from the scanned bedforms some aspects of the surface dynamics that took place when the bedforms were forming. These dynamics are complex and involve multiple snowfall and wind events, often from various directions. One consistent feature of the dynamics is that they tend to create complex compound surfaces rather than producing discrete and separate forms like those described above. These dynamics explain to a large extent why forms like barchans and snow waves are relatively rare.

2.3.4.1 Dynamic Behavior of a Barchans Field

While a few videos of moving barchans are available (i.e. *Météo-France* [2008] and *Niwot Ridge Youtube Channel* [2013]), to date there has not been a study on snow barchans in motion. But because snow and sand barchans are similar we can infer much from these desert studies. Specifically, using aerial and satellite imagery of deserts on Earth and Mars, as well as cellular automata modeling, *Ewing and Kocurek* [2010] and *Kocurek et al.* [2010] have classified the interaction of barchan dunes. These interactions include collision, calving, merging, and lateral linking. From our scanned snow surface "snapshots" of barchans that froze when the wind speed dropped and saltation ceased, similar behavior is observed in snow (Figure 2.10). In these scans there is: 1) the lateral merging of several barchans into a sinuous transverse dune (also called a barchanoid and described by [*Doumani*, 1967]), 2) the oblique alignment of several barchans that could perhaps become a whaleback, 3) the calving of a small barchan from a larger one, and 4) the collision of a small barchan into a larger one that has formed from the merger of two barchans. Certainly more than just these four types of snow dune interactions exist.
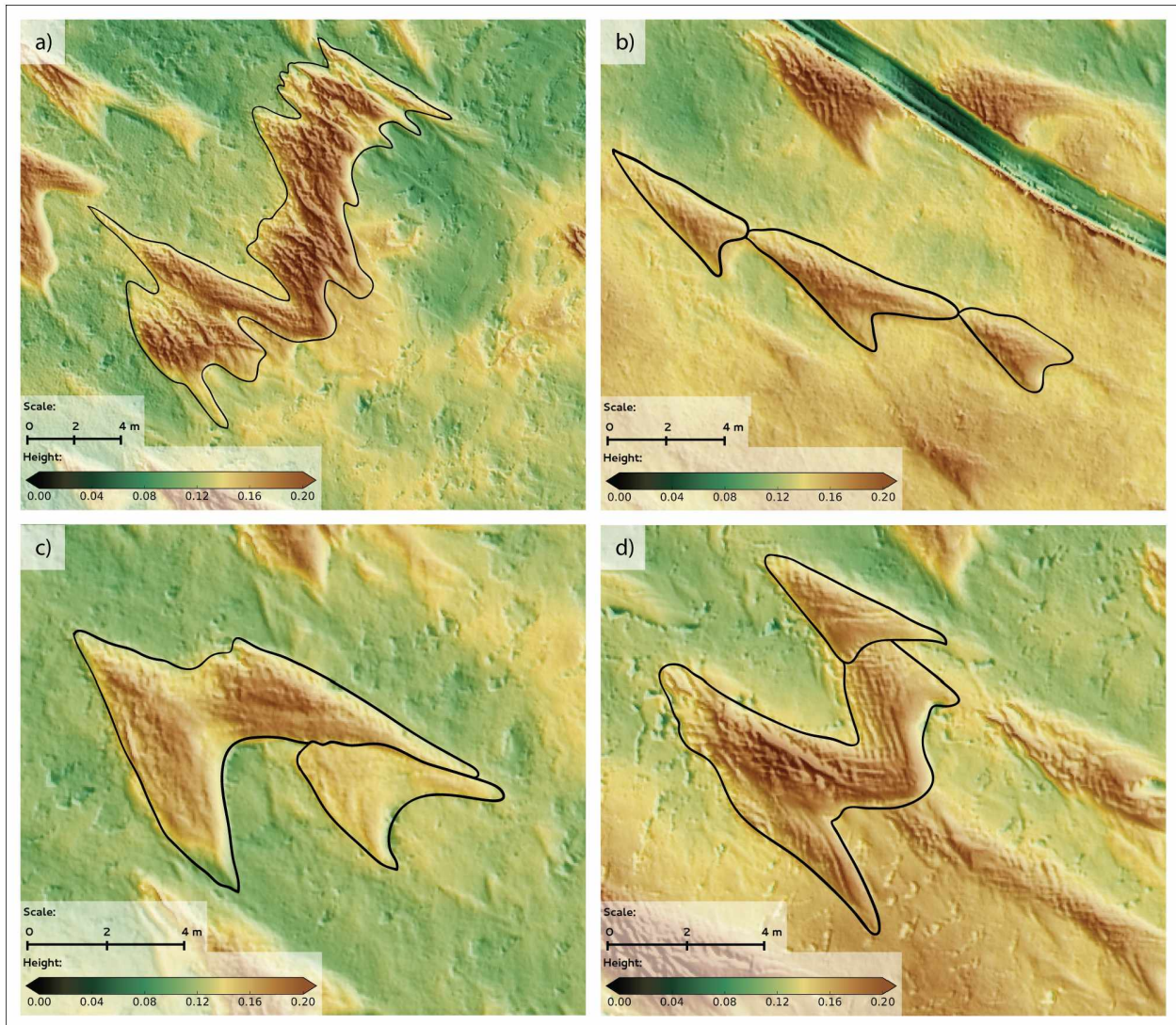
Figure 2.10: Details of the barchans of Field 1 from Figure 2.5. The four panels illustrate the various dynamic behaviors that dunes and barchans can exhibit: a) Lateral merging of several barchans, b) barchans aligning downwind, c) calving of a small barchan off a larger one, and d) collision of a small barchan into a larger one that already merged laterally with a second large barchan. The four maps have a horizontal resolution of 4cm. All units are in meter.

2.3.4.2 From a Dune to a Sastrugi

When *Watanabe* [1978] sectioned a sastrugi he found deeply dipping internal bedding. Because sastrugi are erosional forms this layering had to have been pre-existing, and was most likely a series of foreset beds deposited on the slip face during the formation of a dune or barchan (Figure 2.2b) into which the sastrugi were carved. We have watched the slip face of a snow dune during a blizzard, and these foreset beds are formed in pulses, consistent with the observations of *Baas and Sherman*

[2005] that saltation does not occur uniformly. Snow streamers and wind gustiness may be what drive these pulses. Whatever their cause, the resulting layers are thin, real, but subtle and difficult to detect by an observer in cross-section. The wind, however, does a good job of exposing these beds because of slight variations in hardness that lead to differential erosion. The foreset beds are truncated by the substrate base, across which the barchan propagates. These beds intersect that base at angles ranging from 15° to 45° in the center of the barchan (Table 2.2) but less than 5° along the outer edges of the horns due to the curved geometry of the slip face (Figure 2.2a). Consequently for beds about 15 mm thick the horizontal spacing of the beds along the outer edge of the barchan will be much larger due to the low angle of intersection between the foreset beds and the substrate: that spacing would range from 17 to 28 cm (spacing =15 mm/sin(intersection angle)) for angles ranging from 3° to 5°.

As detailed in Section 2.3.3.2, these same edges show a serration at a comparable spacing (Figure 2.11), suggesting preferential erosion controlled by bed spacing. In some fashion we do not fully understand, the intersection of the foreset beds with the substrate base serve as the inception points for the erosion that ultimately produces sastrugi. We see that with increasing time and degree of erosion, the edge serrations turn into a series of hard ridges that make an oblique angle to the wind direction, the same ridges that create the patterned tail markings we described earlier as a harlequin pattern. *Moss* [1938] described exactly the same pattern on the Greenland ice cap, implying that this dynamic erosion pattern is widespread. He called it an "interference" pattern producing a perfectly regular system of little pits, and suggested that once these diamond-shaped scoops or pits had formed, a feedback process with the wind would deepen and widen them. We agree with his analysis and suggest that with time and continued wind erosion, sastrugi, and eventually lanceolate sastrugi, are produced from this modest inception process.
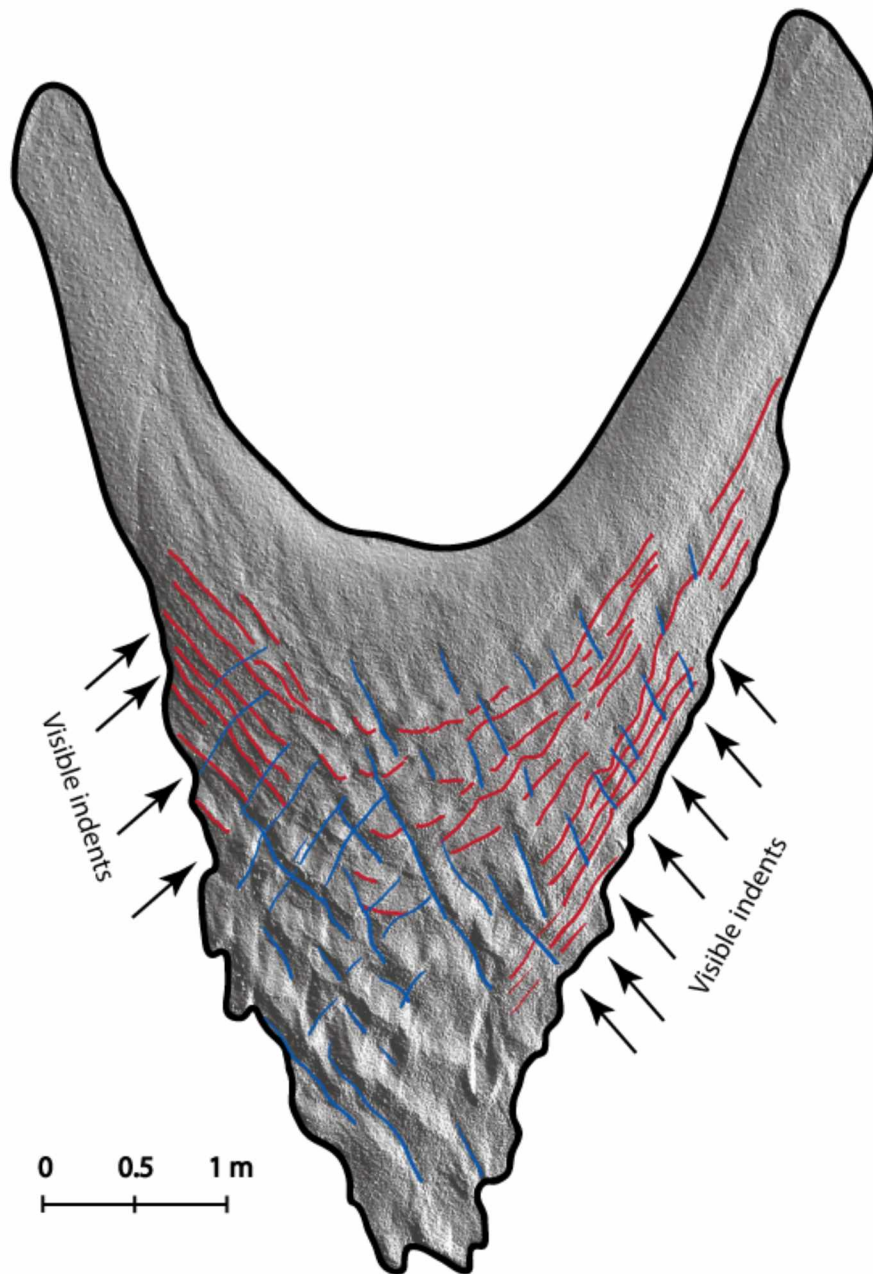
Figure 2.11: A barchan showing serrated edges with approximately 25 cm serrations. Serrations emanating from both edges intersect in the middle of the dune in a harlequin pattern. *Moss* [1938] called this an "interference pattern producing a perfectly regular system of little pits." Red lines show the fore-set bed lines, and in blue the serration lines.

These secondary erosional features suggest that some sastrugi have as their inception the thin bedding created during the deposition of the source dune. Subtle variations in bedding hardness leads to a pattern of initial erosion pits and ridges on the tail of the barchan. These pits must affect the turbulent structure of the near-surface wind field, as they preferentially deepen with time and wind action. There are undoubtedly alternative formation processes for sastrugi that do not require bedding for sastrugi inception that remain to be investigated, but what is clear is that given time and wind, a dune or barchan will be eroded into sastrugi.

2.4 A Model of Snow Bedform Formation

There are many similarities, and some striking differences, between snow and sand bedforms. Snow bedforms mirror sand bedforms for dunes, barchans, and ripple marks, but there are no real analogies in sand for the snow erosional features (pits, sastrugi, and lanceolate sastrugi). Sand bedforms are also much larger (10X) and much older (100 years vs. 0.3 years). The key to the similarities and differences is time: because snow can and will sinter [*Colbeck*, 1997; *Blackford*, 2007], it limits the length of time the snow remains loose and cohesionless like sand. Once sintering has occurred, it produces a hardened and bonded material that can and will allow erosion, hence it is sintering that leads to the class of snow features not found in sand deserts.

We think of sintering as a timer that starts the moment a snow grain is deposited. If that grain remains in position long enough (and long enough is a function of many things including temperature and grain size), it will become bonded. This rarely takes more than 24 hours. Once this bonding sets in, the flux of grains nurturing depositional bedforms begins to diminish, and there is an inevitable shift from depositional to erosional bedforms. As we have shown, the formation conditions for most depositional snow bedforms (ripples, barchans, snow-waves) are quite rare, but conditions for the erosional forms occur with great frequency. This is the reason sastrugi are so much more common than dunes.

Many of the differences between snow and sand bedforms can be explained by this timer. For example, the difference in age and size of dunes is readily explained by the fact that once a snow dune stops moving, it will sinter and then start eroding rather than growing. Since this takes place in a matter of hours or days, it limits snow dune growth to a period that is about 1/300th as long as a

sand dune, so it is not surprising that snow dunes are generally 1/10th to 1/100th the height of sand dunes. The development of patterned markings and scoops on the tails of barchans also arises from the sintering timer. As *Kuznetsov* [1960] showed, the crest of a barchan is softer than the tail. As we will detail in what follows, that is because the crest is younger and there the sintering timer has not yet run down. For the far upwind end of the tail, however, time will have run out and the grains will have sintered. The tail will stop moving and begin to erode. This also explains why barchan tails remain after an erosion event (harder), but not the younger downwind sections of the barchan (softer).

In what follows we present a simple model that describes this behavior. We start with classic functions from *Bagnold* [1941] linking the flux of snow grains to the wind speed. The flux controls both the growth and the downwind propagation speed of a dune, and therefore the difference in age between the dune tail (old) and the dune slip face (young). The faster the dune moves, the smaller the age differential. As long as the flux of grains remains high, the dune can continue to propagate fast, but its growth in height creates ever-increasing demands on the flux to maintain forward motion, and eventually the dune has to slow down. Here we bring in sintering, which increases the snow hardness as a function of time. It serves as a control on the availability of snow grains for transport. Between increasing demand for material driven by the growth of the dune, and the decreasing supply due to the sintering timer winding down, eventually, the dune stops, or at least its tail does so. At this point in time erosion rather than deposition commences. In fact, in our simple model, erosion (into sastrugi) is the ultimate fate of every snow dune.

2.4.1 The Windblown Flux of Granular Material in the Boundary Layer

The windblown flux is what keeps dunes propagating and growing in height. It is a function of wind speed, but also of the cohesive forces preventing grains from being entrained by the wind. Here we first derive a simple equation relating the flux and the wind speed.

Bagnold [1941] understood that the main driver in sand dune morphology was the flux of material transported by wind, and that, in turn, this was a function of wind speed. Particles become mobilized for transport when the wind shear stresses are sufficiently high to overcome grain inertia due to the mass, as well as other cohesive forces retaining the grain in its initial position. *Bagnold*

compared the velocity profile of a steady-state wind blowing over a hard surface versus that over a saltating surface. He found a reduced velocity profile when there were saltating particles because of the transfer of momentum from wind to particles.

When no saltation occurs in steady state conditions, the wind shear stress (τ_0) in force per unit area is directly related to the wind velocity gradient ($\delta U / \delta ln z$):

$$\tau_0 = \rho_{air} \left(\kappa \frac{\delta U}{\delta ln\ z} \right)^2 \qquad (2.3)$$

where κ is the Von Kármán constant ($\simeq 0.4$), and z the height above ground. For convenience, a friction velocity U_* can be defined by $((\tau/\rho_{air})^{0.5})$, then solving Equation (2.3) we obtain the following wind velocity profile equation:

$$U(z) = \frac{U_*}{\kappa} ln \left(\frac{z}{z_0} \right) \qquad (2.4)$$

where z_0 is the height where the mean wind velocity extrapolates to zero, also called the roughness height.

Bagnold observed that the wind velocity profile can be split into two parts: 1) the profile in the saltating layer, which increases at a rate called the threshold friction velocity (U_{*th}) up to a new roughness height (k'), and 2) the profile above the saltating layer, which has a modified rate of increase (U_*). The threshold velocity (U_{th}) can be found where the wind profile changes slope. U_*' can then be derived:

$$U_*' \propto \frac{(U - U_{th})}{ln \left(\frac{z}{k'} \right)} \qquad (2.5)$$

with U measured at height z, and U_{th} at height k'. If now we assume a saltating flux q_s, then the momentum transferred to the particles per second is equal to τ', the drag on the air by the particles in motion:

$$\tau' = q_s \frac{(u_2 - u_1)}{l} \qquad (2.6)$$

where u_2 is the particle's horizontal velocity after traveling through the air a distance l, and u_1 is the initial horizontal velocity of the particle, which can be neglected. Following *Bagnold*'s reasoning, more recently *Andreotti et al.* [2002] have suggested that u_2/l can be approximated by the ratio between gravity and the initial vertical velocity of the particle: g/w_1. Then equation (2.6) becomes

$$\tau' = \rho_{air} U_*'^2 = q_s \frac{g}{w_1} \qquad (2.7).$$

By substituting equation (2.5) into (2.7) and assuming that w_1 is proportional to U_*', according to *Bagnold*, equation (2.7) becomes:

$$q_s \propto \rho_{air} \frac{(U - U_{th})^3}{g} \qquad (2.8).$$

However, *Iversen et al.* [1975], studying aeolian structures around Martian craters with similitude models in wind tunnels, developed a slightly different version of equation (2.8) for q_s that was later applied and tested for blowing snow by *Iversen* [1980] and *Schmidt* [1982]:

$$q_s \propto \rho_{air} U_*^2 \frac{(U_* - U_{*th})}{g} \qquad \text{when} \quad U_* > U_{*th} \qquad (2.9).$$

In both equations (2.8) and (2.9) the flux is assumed to be in equilibrium with the wind speed, and therefore would reach saturation.

2.4.2 Dune Propagation as a Function of the Flux

Early on, *Exner* [1931] deduced that transverse dune propagation depended on the particle flux flowing across the dune and the dune height (*cf.* Figure 2.2b). The dune propagation speed (c) is typically measured at the crest. If we assume a two dimensional dune of height h and length L moving in the direction of the wind, the velocity of the dune is proportional to the volume of particles moving from the windward side of the dune to the leeward side, or as expressed explicitly by *Kobayashi* [1980]:

$$c = \alpha \frac{Q}{\rho_{bulk} h} \qquad (2.10)$$

where Q is the total particle flux, which can be approximated by the saltating flux q_s. α is a coefficient corresponding to the efficiency of deposition of particles on the leeward side, and ρ_{bulk} is the bulk density of the dune. Later, we will assume $\alpha = 1$ and $\rho_{bulk} = 350$ kg m^{-3}.

2.4.3 Snow Grain Sintering

Sintering is a process where two ice particles in contact grow an ice bond [*Colbeck*, 1997; *Blackford*, 2007]. The effect of sintering is to increase the cohesive forces holding a grain in place. Considerable effort has gone into trying to understand the controls and rates of this process. *Hobbs* [1974] suggested that ice bonds grow at a rate that depends on the temperature (T), pressure (P), and grain radius (R), as expressed by:

$$\left(\frac{x}{R}\right)^5 = \frac{B(T,P)t}{R^3} \qquad (2.11)$$

where $B(T,P)$ is an empirical function relating temperature and pressure conditions to the ice neck geometry, and x is the bond radius. *Schmidt* [1980] used this relationship to derive the force required to break the bond between two idealized ice grains assuming an ice tensile strength of σ, and that ice behaves elastically for impact forces at temperature ranging from -3 to -40°C. He then estimated a threshold impact velocity necessary to break bonds of radius x. His results indicate that as the ratio (x/R) increases, the threshold impact velocity has to increase too. Consequently, as snow sinters, stronger and stronger winds are needed to break loose grains and mobilize them for saltation.

Schmidt's model is difficult to use in practice. Not only does it use a highly idealized grain geometry and packing, but it also has limited applicability to natural snow because equation (2.11) was derived from laboratory experiments by *Hobbs and Mason* [1964]. They prepared snow samples of high density (>550 kg m^{-3}) and did not account for the presence of air convective cells typically present in natural snow packs, which would enhance sintering considerably.

Instead, we use here an empirical relationship to model sintering. *Gow and Ramseier* [1964] experimentally measured the snow hardness (*i.e.* unconfined compressive strength) evolution for different temperatures and ambient conditions at the South Pole of non-sieved snow samples. As they were interested in mechanical properties of snow for building under-snow facilities by the U.S.

Army, they looked at the evolution of snow hardness over 400 hrs. Their results show in all cases a rapid increase in hardness in the first 20-40 hours, followed by a slower secondary increase. *Jellinek* [1959] did a similar experiment using sieved and compacted snow samples previously stored for at least 30 days at -20°C. He obtained higher compressive strength, but he also found a rapid increase of the strength during the first 20-40 hours.

As *Gow and Ramseier* [1964] provide hardness measurements as a function of time for undisturbed snow, we choose to use their data for snow samples exposed to solar radiation at -26°C. For our modeling, we restricted our use to the first 24 hours of data, which can be approximated by a linear fit:

$$H = 0.152A + 0.836 \qquad (2.12)$$

where A is the age of the snow since deposition in hours and the hardness H is in kg m^{-2}.

Kotlyakov [1966] empirically related the minimum wind speed necessary to begin eroding a snow surface for a given hardness. He performed his measurement at Mirny station in Antarctica, the same location where *Kuznetsov* [1960] observed the formation of barchan dunes. Few details are provided about his data collection methods, but his observations of snow and the wind conditions necessary to erode the snow are unique. Within a temperature range from -12 to -15°C, he found a linear dependence between the snow hardness (H) and the wind speed (U):

$$H = 0.15U - 0.75 \qquad (2.13)$$

with H in in kg m^{-2} and U in m s^{-1}.

As the formulation of sintering (Equation 2.11) is derived from laboratory experiments and requires theoretical assumptions to be applied to real blowing snow, and because equations (2.12) and (2.13) are the only in-situ measurements with undisturbed snow that relate U_{th}, the threshold wind speed, to snow hardness and therefore to a time variable, we use the latter to explore the effect of sintering on dune dynamics by combining them into a single equation:

$$U_{th} = 0.01A + 0.57 \qquad (2.14).$$

2.4.4 Dune Age Function

Kuznetsov [1960] noted that the tail of a migrating dune was harder than its crest. It is also older and has therefore undergone greater sintering. If we assume a two dimensional dune of length L migrating down the wind at speed c, the age difference between the crest and the upwind end of the tail is:

$$A = L/c \qquad (2.15).$$

From data for barchan Fields 1 and 2 (Figure 2.7), we can derive a relationship between the length and height of a dune: $L = 51.29h+1.38$, which when substituted into equation (2.15) gives:

$$A = (1.38 + 51.29h)/c \qquad (2.16).$$

2.4.5 The Effect of Sintering on Dune Dynamics

We are now ready to model the behavior of a dune that is growing, propagating downwind, and aging. Equation (2.16), linking dune height and propagation speed to the age of the tail, can be substituted into equation (2.14), which provides the threshold wind speed necessary to saltate snow that has undergone a given amount of sintering. As *Iversen*'s equation (2.9) relates the threshold friction velocity, the friction velocity, and the flux, we can, for a known stage of sintering (age), estimate the friction velocity required to sustain a given flux of snow. By assuming in equation (2.4) a roughness height z_0 of 1 mm [*Andreas*, 2011], we can then convert the friction velocity back to its equivalent wind speed U at 1 m high.

We have plotted dune propagation speed vs. dune height (Figure 2.12), then overlaid these with contours of fluxes obtained from equation (2.10) and the equivalent wind speed necessary to sustain the flux. Ages older than 24 hours have been left off the graph as we are limited by the linear fit of the data of *Gow and Ramseier* [1964], for which we only use the first 24 hrs.

43
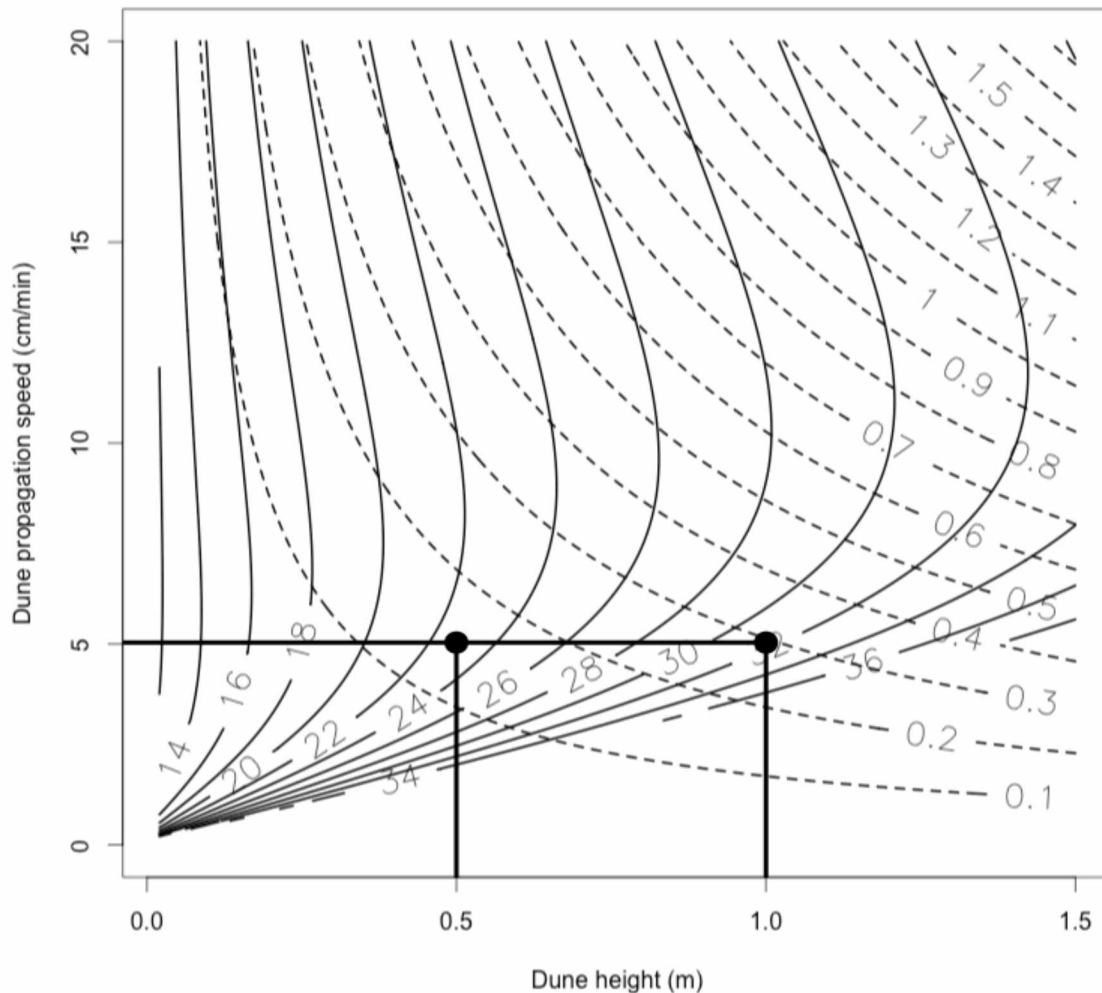
Figure 2.12: Relationship between dune height, velocity propagation speed, flux of saltating snow (dashed contour lines) in kg (s m)$^{-1}$, and the wind speed necessary to sustain the saltating flux in m s^{-1} (black contour lines) for moving a dune of a given height. Values presented in this diagram are estimates and do not account for changes of sintering rates due to snow temperature. Snow is assumed to have a bulk density of 350 kg m^{-3}. The two black dots indicate two sets of conditions for maintaining a dune respectively 0.5 m and a 1 m tall moving at 5 cm min^{-1}.

Effectively, Figure 2.12 shows the wind speed required to sustain a dune of a given height (*h*) moving at a given speed (*c*). A dune will sustain itself when it is moving sufficiently fast enough that deposited snow particles do not have time to sinter before being entrained by the wind. For example, a 0.2 m high dune (a reasonable height, see Table 2.2) might propagate at 5 cm min^{-1} (also a reasonable value). To do so, the wind would initially need to be blowing 20 m s^{-1}, a stiff wind. As the same dune grew to a height of 0.6 m through deposition, the wind would need to increase to 29 m s^{-} ^{1} (104 km h^{-1}) in order to prevent the tail of the dune from sintering past the point where the wind

could continue to entrain snow grains. For the Arctic regions in which we work, the probability of such a high wind is vanishingly small (<0.01%). To reach 1 m height without immobilization, the wind would have to reach an extreme speed of 37 m s^{-1}. The figure makes it clear that as a field of snow dunes develops, the wind will have to continuously increase in order to counteract the effect of sintering, otherwise the tails of the dunes will eventually sinter, and then erosion rather than deposition will commence. The results[2] also suggest why no snow dunes can ever reach the size and the age of sand dunes.

2.5 A New Classification of Snow Bedforms

Earlier classification systems of snow bedforms [*Watanabe*, 1978; *Goodwin*, 1990] recognized erosional and depositional forms, but were not based on the physical conditions that generated these forms. The connections between wind speed, erodibility, flux, and age discussed in Section 4 can be used to frame a new classification system. In it, the various bedforms appear as a continuum of aeolian shapes that arise due to the physical conditions prevailing at the snow surface (Figure 2.13). The axes of the classification are wind speed and the threshold wind speed for maintaining a saturated flux, U_{th}. In this system, if due to sintering, U_{th} is greater than U, then a saturated flux cannot be sustained and erosional forms like sastrugi develop. The erosion regime occupies the entire domain above the line $U=U_{th}$. When U exceeds U_{th}, then a saturated flux can be maintained and will increase with wind speed. In this regime, depositional forms are produced, but as discussed in Section 2.2.1.1, it is the flux that determines the nature of these forms. As the flux increases, barchans (Figure 2.5) transition to barchanoids (Figure 2.10a), and then these become snow-waves (Figure 2.1a).

Using this physical classification system, one can describe bedform trajectories. These would take the form of a curving path through the U--U_{th} space. The time spent on the path in one area of the domain would be related to the time that a feature was able to grow in size (or in the case of sastrugi, deepen), with larger barchans and dunes the product of more time spent in that part of the domain. As wind speed and snow surface conditions changed, the forms found in one part of the classification would morph into those found in another part. This path would then represent the

---

[2] Sensitivity analysis of the model available in Appendix A

unique history by which an observed snow surface arrived at its current condition. If we could follow these paths sufficiently well, like *Nakaya* [1954] using a snowflake to determine the conditions in the cloud from which the snowflake fell, we could use the characteristics of a particular bedform as a witness of past surface atmospheric conditions that prevailed in the area.
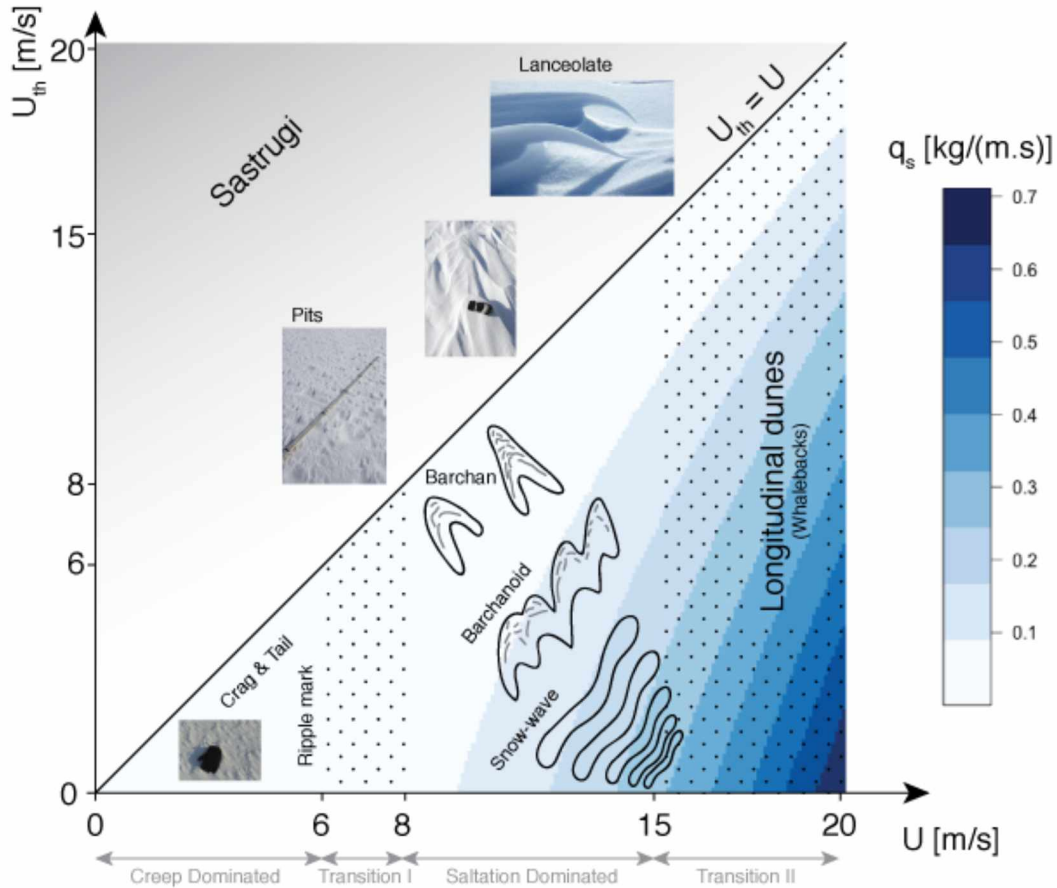
Figure 2.13: Classification of bedforms genesis based on the average wind speed U, and the average threshold wind velocity U_{th} of the snow surface. The flux of saltating snow (q_s) depending on U and U_{th} is overlaid as it explains the transition between barchans to barchanoid to snow-waves.

2.6 Discussion: Compound Snow Surfaces

Even if we could draw scenario paths on Figure 2.13, in most cases they would not help much with understanding how a particular snow surface came about. Unfortunately, most windblown snow surfaces exhibit complex compound features because they are the result of multiple erosion/deposition events. And as *Moss* so presciently noted in 1938, not only do the conditions for bedform development change with time (Figures 2.12 and 2.13), but also the near-surface wind fields evolve with eddies and vortices being set up as a result of the changing surface micro-

46

topography. Strong, but poorly known, feedbacks exist between bedforms and the wind, and these have as large an impact on bedform evolution and shape/size as do the considerations discussed in Sections 2.4 and 2.5. In addition, surface forcing conditions (wind speed and direction, temperature, sunlight, and the nature of the loose snow grains) are constantly changing with the winter weather. Changes affecting surface conditions happen at both landscape and bedform scales. A good example of bedform scale variation is the difference of hardness between the tail and the crest of a barchan, thus varying the threshold wind speed over the distance of a few meters and facilitating the appearance of sastrugi on the barchan tail.

In all of the preceding sections we have described and modeled individual discrete bedforms, and most previous researchers have focused on these as well. But of the sites we measured using the laser, 6 of the 9 sites had compound surfaces (Figure 2.14). Examination of these surfaces reveals that they are composed of intersecting dunes (Figure 2.10), dune remnants (Figure 2.14), and of course, a heavy preponderance of sastrugi (Figures 2.1 and 2.9). In fact, Figure 2.9 (sastrugi ridge traces) is a subset of the compound surface shown in Field 4 in Figure 2.14.

Observing the bedforms from Field 7 in Figure 2.14 can lead us toward a hypothetical evolution in six steps: 1) a new snowfall provides material for transport by 2) a rising south wind. This leads to 3) the development of a field of barchan dunes (indicated by the blue stars on Field 7), which 4) over a period of time sinter and harden so that 5) when the wind rises again, some of the barchans are carved into sastrugi (i.e. lanceolate sastrugi). Favored barchans (or at least parts of barchans) survive this erosion, so that 6) when the next new snowfall occurs with winds from the North, a new set of intersecting barchan dunes is formed, these oriented 180° from the previous ones (indicated by the red stars in Figure 2.14).

An infinite range of surface forms is possible for compound surfaces. At one end of the spectrum, the surface might be composed primarily of superimposed intersecting and overlapping dunes. At the other end of the spectrum, the surface might be almost completely erosional with intersecting sastrugi from many directions, and every sort of combination in between is also possible.
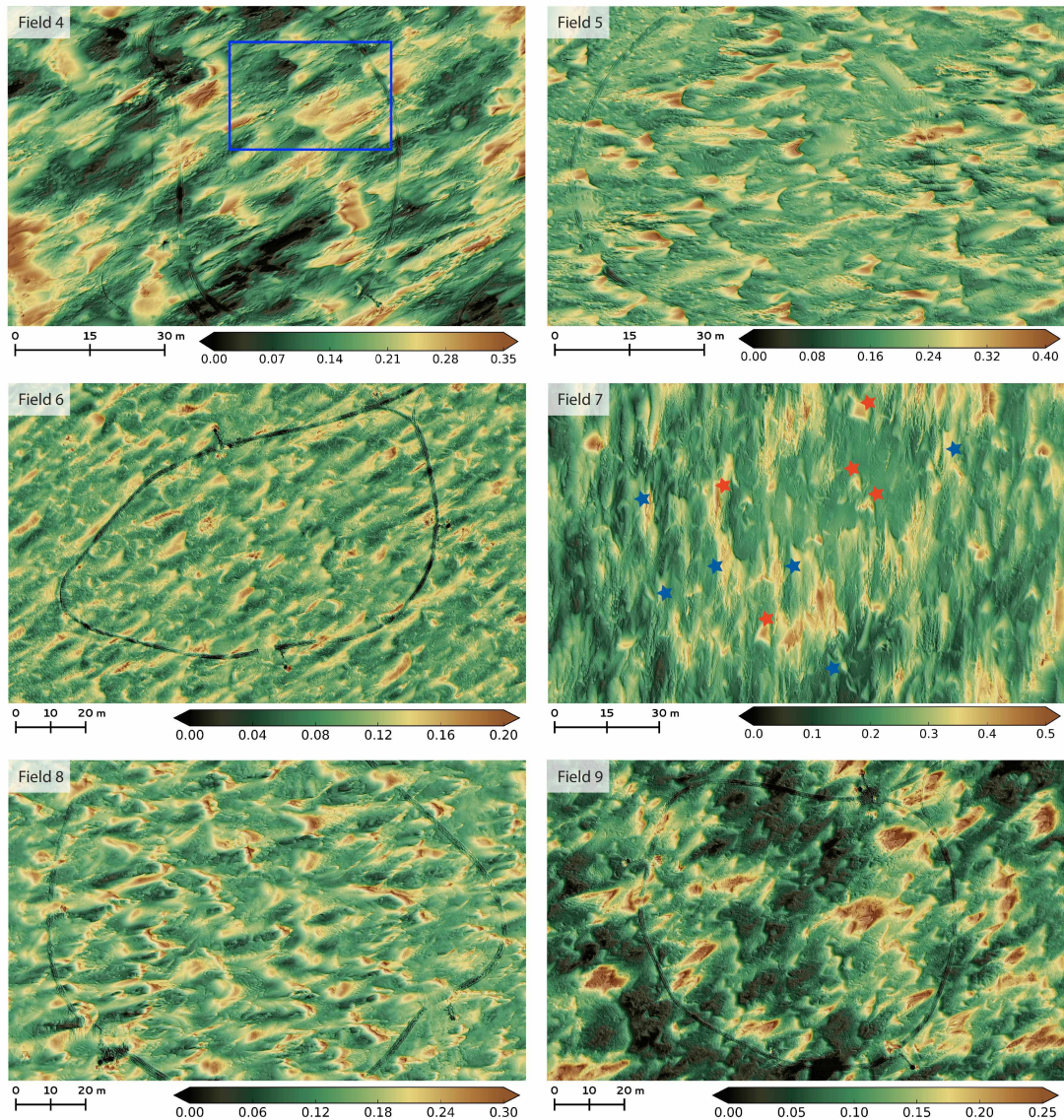
Figure 2.14: Overview of six snow fields surface elevation resulting from the superposition of a variety of bedforms. These surfaces can be seen as compound because of the various bedforms witnessing of multiple snow drifting events. On each site we can see some barchan dunes, surrounded by heavy sastrugi fields. Field 4, 5, 6 and 8 were sites located on the tundra of the North Slope coastal plain. Fields 7 and 9 were located on frozen lakes. The blue box on field 4 indicates the boundary of the sastrugi field presented in Figure 2.9. The red and blue stars on field 7 indicate two sets of barchans that formed under opposite wind directions. Each of these terrain models was detrended by fitting a horizontal plane. Large-scale topography (>8m) was eliminated from fields 5, 6, and 8 using an averaging kernel of 8 by 8 meter. All units are in meter.

These compound surfaces are the result of a succession of weather events interacting with a spatially heterogeneous granular material whose properties change with the weather and age. *Budd et al.* [1966]

have produced a rich description of how such surfaces evolved during 129 sequential weather events over the course of eight months at Byrd Station, Antarctica. We agree completely with their conclusion that "*A full understanding of drift features require[s] an analysis of the surface history preceding each run [individual event] . . .*"

The existing spatial variability of the surface properties of the snow (*i.e.* hardness, geometry, grain size, layering…) sets the type of effect the wind will have on snow: erosion versus deposition. For example, in Figure 2.9 there are distinct zones of where there are sastrugi, and other shadowed zones where there are not. Figure 2.14 shows more examples where the spatial heterogeneity has many scales of variability.

Our model shows how sintering plays a key role in the construction of compound surfaces through its limitation of bedform age and size. By immobilizing bedforms, it creates the material for erosion and sastrugi. However, sintering also affects the surface heterogeneity by locally attenuating or accentuating the erodibility of the snow because it produces a snowfield with a wide range of ages of features.

2.7 Conclusion

Here we have reviewed the literature and introduced new data on snow bedforms. Based on the new and old data, we have suggested a new classification system of snow bedforms that not only describes their shapes, but also relates them to the set of physical conditions (wind and surface threshold conditions for grain erosion) that generate their shapes. Using a simple mathematical model, we show that for discrete dunes or barchans, there is a fine balance between the flux of saltating snow, the wind speed, and the hardness (erodibility) of the snow, with the latter determined by snow sintering. Sintering acts fast to lock up snow (usually in less than 24 hours), so unless the wind and flux can keep a dune propagating downwind rapidly, the dune will stop, at which point erosion and the development of sastrugi will begin. In this way snow differs from sand. Sintering limits snow dune growth, which is why snow dunes are so much smaller than sand dunes, and is the reason why sastrugi (erosional features) are the most common snow bedform.

Our classification system and model also indicate that conditions (wind speed and mobilizable snow) required to grow dunes are quite restrictive, which explains why so few observations of snow dunes are available in the literature despite the vast area where they could form. Among these rarer bedforms, snow-waves are the rarest: they require a very large flux of snow but also a narrow window of wind speed, which goes a long way toward explaining why there are only four examples in the literature to date.

The development of laser scanning technology (terrestrial and airborne) as well as the recent advances in structure-from-motion techniques for snow, open the possibility of collecting far more quantitative data on snow bedforms. Using terrestrial laser scanning technology on the North Slope of Alaska, we have provided the first detailed morphological characteristics of snow barchans of which we are aware. The technology alone, however, is not going to be sufficient to improve our understanding of these features. For that, we are going to need to make increasing use of the research and methods being used to study sand bedforms and sand barchan processes. Comparing our data to sand barchans, we find that snow barchans are flatter but that their footprints are quite similar. Snow barchans also form on a time scale that is almost ephemeral compared to sand barchans. Such a property could actually prove useful and relevant in the study of sand dune dynamics, because for snow in a few hours it is possible to observe bedform evolution that might take decades in sand.

Our model on the effect of sintering on snow surface conditions and bedform development is indicative of the potential impacts of sintering on bedforms, and more generally, on blowing snow features. The current lack of clear literature on the relationship between drifting snow and sintering is a key area of research that is going to be needed before we can more accurately model these features in the future.

Finally, we have highlighted that compound snow bedforms are by far the most prevalent. Our current understanding of snow bedforms and the interaction of wind and snow grains does not provide enough knowledge for modeling such a complex system. In this area we need to emulate the progress that has been achieved towards understanding temporal and spatial variations of sand particle transport [*Baas and Sherman*, 2005; *Huang and Wang*, 2015], and physically based modeling of

sand transport [*Durán et al.*, (2010), *Parteli et al.*, 2014] in order to make further progress in the study of snow bedforms.

Acknowledgements

References

Albert, M. R., and R. L. Hawley (2002), Seasonal changes in snow surface roughness characteristics at Summit, Greenland: Implications for snow and firn ventilation, *Annals of Glaciology*, *35*(1), 510–514, doi: 10.3189/172756402781816591.

Allen, J. (1965), Scour marks in snow, *Journal of Sedimentary Research*, *35*(2), doi: 10.1306/74D71267-2B21-11D7-8648000102C1865D.

Allen, J. (1971), Bed forms due to mass transfer in turbulent flows: a kaleidoscope of phenomena, *Journal of Fluid Mechanics*, *49*(01), 49–63, doi: 10.1017/S0022112071001927.

Andreas, E. (2011), The Fallacy of Drifting Snow, *Boundary-Layer Meteorology*, 141(3), 333347, doi: 10.1007/s10546-011-9647-8.

Andreotti, B., P. Claudin, and S. Douady (2002), Selection of dune shapes and velocities part 1: Dynamics of sand, wind and barchans, *The European Physical Journal B-Condensed Matter and Complex Systems*, *28*(3), 321–339, doi: 10.1140/epjb/e2002-00236-4.

Baas, A. C. (2007), Complex systems in aeolian geomorphology, *Geomorphology*, *91*(3), 311–331, doi: 10.1016/j.geomorph.2007.04.012.

Baas, A. C. W., and D. Sherman (2005), Formation and behavior of aeolian streamers, *Journal of Geophysical Research: Earth Surface (2003–2012)*, *110*(F3).

Bagnold, R. A. (1941), The physics of wind blown sand and desert dunes, *Methuen, London, 265*.

Benson, C. S. (1962), Stratigraphic studies in the snow and firn of the greenland ice sheet, *Technical Report SIPRE-RR-70*, US Army, Snow, Ice and Permafrost Reseach Establisment.

Birnbaum, G., J. Freitag, R. Brauner, G. König-Langlo, E. Schulz, S. Kipfstuhl, H. Oerter, C. H. Reijmer, E. Schlosser, S. H. Faria, H. Ries, B. Loose, A. Herber, M. G. Duda, J. G. Powers, K. W. Manning, and M. R. van den Broeke, (2010), Strong-wind events and their influence on the formation of snow dunes: observations from Köhnen station, Dronning Maud Land, Antarctica, *Journal of Glaciology*, *56*(199), 891–902, doi: 10.3189/002214310794457272.

Black, H., and W. Budd (1964), Accumulation in the region of Wilkes, Wilkes land, Antarctica, *Journal of Glaciology*, *5*(37), 3–15.

Blackford, J. R. (2007), Sintering and microstructure of ice: a review, *Journal of Physics D: Applied Physics*, *40*(21), R355, doi: 10.1088/0022-3727/40/21/R02.

Blackwelder, E. (1930), Yardang and zastruga, *Science*, *72*(1868), 396–397, doi: 10.1126/science.72.1868.396.

Bourke, M. C. (2010), Barchan dune asymmetry: Observations from mars and earth, *Icarus*, *205*(1), 183–197, doi: 10.1016/j.icarus.2009.08.023.

Budd, WF, W. Dingle, and U. Radok (1966), The Byrd snow drift project: outline and basic results, *Studies in Antarctic Meteorology*, 71-134, doi: 10.1029/AR009p0071.

Castellani, G., C. Lüpkes, S. Hendricks, and R. Gerdes (2014), Variability of Arctic sea-ice topography and its impact on the atmospheric surface drag, *Journal of Geophysical Research Oceans*, 119, doi: 10.1002/2013JC009712

Colbeck, S. (1989), Air movement in snow due to windpumping, *J. Glaciol, 35*(120), 209–213.

Colbeck, S. C. (1997), A review of sintering in seasonal snow, *Technical report*, DTIC Document.

Cooke, R. U., W. Andrew, and A. Goudie (1993), *Desert geomorphology*, Taylor & Francis.

Cornish, V. (1902), On snow-waves and snow-drifts in Canada, with notes on the" snow-mushrooms" of the selkirk mountains, *The Geographical Journal*, *20*(2), 137–173.

Cornish, V. (1914), *Waves of sand and snow and the eddies which make them*, Fisher-Unwin, London.

Cutts, J., and R. Smith (1973), Eolian deposits and dunes on mars, *Journal of Geophysical Research*, *78*(20), 4139–4154.

Deems, J. S., T. H. Painter, and D. C. Finnegan (2013), Lidar measurement of snow depth: a review, *Journal of Glaciology*, *59*(215), 467–479, doi: 10.3189/2013JoG12J154.

Dobrowolski, A. B. (1924), Mouvement de l'air et de l'eau sur des accidents du sol, *Geografiska Annaler*, *6*, 300–367.

Doumani, G. A. (1967), Surface structures in snow, *Physics of Snow and Ice: proceedings*, *1*(2), 1119–1136.

Durán, O., Parteli, E. J., and H. J. Herrmann (2010), A continuous model for sand dunes: Review, new developments and application to barchan dunes and barchan dune fields. *Earth Surface Processes and Landforms*, *35*(13), 1591-1600, doi: 10.1002/esp.2070.

Ewing, R. C., and G. A. Kocurek (2010), Aeolian dune interactions and dune-field pattern formation: White sands dune field, New Mexico, *Sedimentology*, *57*(5), 1199–1219, doi: 10.1111/j.1365-3091.2009.01143.x.

Exner, F. (1931), Zur Dynamik der Bewegungsformen auf der Erdoberfläche (in German), *Ergeb. Kosmisch. Phys.*, *1*, *374–445*.

Fahnestock, M., T. Scambos, C. Shuman, R. Arthern, D. Winebrenner, and R. Kwok (2000), Snow megadune fields on the East Antarctic Plateau: Extreme atmosphere-ice interaction, *Geophysical Research Letters*, 27, doi: 10.1029/1999GL011248.

Finkel, H. J. (1959), The barchans of southern Peru, *The Journal of Geology*, pp. 614–647.

Frezzotti, M., S. Gandolfi, F. La Marca, and S. Urbini (2002a). Snow dunes and glazed surfaces in Antarctica: new field and remote-sensing data. *Annals of Glaciology*, 34(1), 81-88. doi: 10.3189/172756402781817851

Frezzotti, M., S. Gandolfi, and S. Urbini (2002b), Snow megadunes in Antarctica: Sedimentary structure and genesis, *Journal of Geophysical Research.*, 107(D18), 4344, doi: *10.1029/2001JD000673*, 2002.

Fujiwara, K., and Y. Endo (1971), Preliminary report of glaciological studies, *Japanese Antarctic Research Expedition scientific reports. Special issue*, *2*, 68–109.

Goodwin, I. D. (1990), Snow accumulation and surface topography in the katabatic zone of eastern Wilkes Land, Antarctica, *Antarctic science*, *2*(03), 235–242.

Goudie, A. S. (2007), Mega-yardangs: A global analysis, *Geography Compass*, *1*(1), 65–81, doi: 10.1111/j.1749-8198.2006.00003.x.

Gow, A. J., and R. O. Ramseier (1964), Age hardening of snow at the South Pole, *Technical report*, DTIC Document.

Grenfell, T. C., and G. A. Maykut (1977), The optical properties of ice and snow in the arctic basin, *Journal of Glaciology*, *18*, 445–463.

Harder, S. L., S. G. Warren, and R. J. Charlson (2000), Sulfate in air and snow at the South Pole: implications for transport and deposition at sites with low snow accumulation. *Journal of Geophysical Research: Atmospheres*, *105*, 22825-22832, doi: 10.1029/2000JD900351

Hargitai, H. I. (2013), Live monitoring of development of ice and snow features as planetary analogs on lake Balaton, *Paper presented at 44th Lunar and Planetary Science Conference, Lunar and Planetary Inst., The woodlands, USA.*

Hobbs, P. V. (1974), Ice physics, *Oxford: Clarendon Press, 1974, 1.*

Hobbs, P. V., and B. Mason (1964), The sintering and adhesion of ice, *Philosophical Magazine*, *9*(98), 181–197.

Huang, N. and Wang, Z. (2015), A 3-D simulation of drifting snow in the turbulent boundary layer, *The Cryosphere Discussion*, 9, 301-331, doi: 10.5194/tcd-9-301-2015

Iversen, J. (1980), Drifting snow similitude-transport rate and roughness modeling, *Journal of glaciology*, *26*, 393 403.

Iversen, J., R. Greeley, B. R. White, and J. B. Pollack (1975), Eolian erosion of the Martian surface, part 1: Erosion rate similitude, *Icarus*, *26*(3), 321–331.

Jellinek, H. H. G. (1959). Compressive strength properties of snow. *Journal of Glaciology*, *3*, 345-354.

Kobayashi, D. (1972), Studies of snow transport in low-level drifting snow, *Contributions from the Institute of Low Temperature Science*, *24*, 1–58.

Kobayashi, S. (1980), Studies on interaction between wind and dry snow surface, *Contributions from the Institute of Low Temperature Science*, *29*, 1–64.

Kobayashi, S., and T. Ishida (1979), Interaction between wind and snow surface, *Boundary-Layer Meteorology*, *16*(1), 35–47.

Kocurek, G., R. C. Ewing, and D. Mohrig (2010), How do bedform patterns arise? New views on the role of bedform interactions within a set of boundary conditions, *Earth Surface Processes and Landforms*, *35*(1), 51–63, doi: 10.1002/esp.1913.

Kosugi, K., K. Nishimura, and N. Maeno (1992), Snow ripples and their contribution to the mass transport in drifting snow, *Boundary-Layer Meteorology*, *59*(1-2), 59–66.

Kotlyakov, V. M. (1966), *The Snow Cover of the Antarctic and Its Role in the Present Day Glaciation of the Continent*, 7, Israel Program for scientific translations.

Kotlyakov, V. M. (1984) *Glyatsiologicheskiy Slovar'* (Glaciological Dictionary). Leningrad, Gidrometeoizdat.

Kuznetsov, M. A. (1960), Barchan snow drift in the wind belt of east Antarctica, *Sovetskaya Antarkticheskaya ekspditsiya*, *10*, 175–179.

Leonard, K. C. (2009), Antarctic snow drift processes, Thesis, *Columbia University*.

Lister, H., and G. Pratt (1959), Geophysical investigations of the commonwealth trans-Antarctic expedition, *Geographical Journal*, pp. 343–354.

Livingstone, I., G. F. Wiggs, and C. M. Weaver (2007), Geomorphology of desert sand dunes: a review of recent progress, *Earth-Science Reviews*, *80*(3), 239–257, doi: 10.1016/j.earscirev.2006.09.004.

Lorenz, R. D. (2014), Physics of saltation and sand transport on Titan: A brief review, *Icarus*, *230*, 162–167, doi: 10.1016/j.icarus.2013.06.023.

Mattsson, J. O. (2007), Formation of snow dunes in Sweden in winter 2006, *Weather*, *62*(4), 94–95, doi: 10.1002/wea.1.

Météo-France (2008), http://www.cnrm.meteo.fr/spip.php?rubrique167&lang=en

Moss, R. (1938), The physics of an ice-cap, *The Geographical Journal*, *92*(3), 211–227.

Naaim-Bouvet, F., M. Naaim, H. Bellot, and K. Nishimura (2011), Wind and drifting-snow gust factor in an alpine context, *Annals of Glaciology*, *52*(58), 223–230, doi: 10.3189/172756411797252112.

Nakaya, U. (1954), *Snow crystals: natural and artificial*. Harvard University Press.

Niwot Ridge Youtube Channel (2013), https://www.youtube.com/watch?v=KrjspdzU19A, *Youtube*.

Parteli, E. J., O. Durán, M. C. Bourke, H. Tsoar, T. Pöschel, and H. Herrmann (2014), Origins of barchan dune asymmetry: Insights from numerical simulations. *Aeolian Research*, *12*, 121-133, doi: 10.1016/j.aeolia.2013.12.002

Perovich, D. K. (2007), Light reflection and transmission by a temperate snow cover, *Journal of Glaciology*, *53*(181), 201–210, doi: 10.3189/172756507782202919.

Petrich, C., H. Eicken, C. M. Polashenski, M. Sturm, J. P. Harbeck, D. K. Perovich, and D. C. Finnegan (2012), Snow dunes: A controlling factor of melt pond distribution on arctic sea ice, *Journal of Geophysical Research: Oceans (1978–2012)*, *117*(C9), doi: 10.1029/2012JC008192.

Picard, G., A. Royer, L. Arnaud, and M. Fily (2014), Influence of meter-scale wind-formed features on the variability of the microwave brightness temperature around dome c in Antarctica, *The Cryosphere*, *8*(3), 1105–1119, doi: 10.5194/tc-8-1105-2014.

Prokop, A. (2008), Assessing the applicability of terrestrial laser scanning for spatial snow depth measurements, *Cold Regions Science and Technology*, *54*(3), 155–163, doi: 10.1016/j.coldregions.2008.07.002.

Pye, K., and H. Tsoar (1990), *Aeolian sand and sand dunes*, Unwin Hyman.

Richardson, K., and P. A. Carling (2005), A typology of sculpted forms in open bedrock channels, *Geological Society of America Special Papers*, *392*, 1–108, doi: 10.1130/0-8137-2392-2.1.

Rundle, A. S. (1971), Snow accumulation and firn stratigraphy on the east Antarctic plateau, *Antarctic Snow and Ice Studies II*, pp. 239–255.

Sauermann, G., P. Rognon, A. Poliakov, and H. Herrmann (2000), The shape of the barchan dunes of southern morocco, *Geomorphology*, *36*(1), 47–62, doi: 10.1016/S0169-555X(00)00047-7.

Schmidt, R. (1980), Threshold wind-speeds and elastic impact in snow transport, *Journal of Glaciology*, *26*, 453–467.

Schmidt, R. (1982), Properties of blowing snow, *Reviews of Geophysics*, *20*(1), 39–44.

Schmidt, R. (1986), Transport rate of drifting snow and the mean wind speed profile, *Boundary-Layer Meteorology*, *34*(3), 213–241.

Sturm, M. (2010), *Apun: The Arctic Snow (A Teacher's Guide)*, University of Alaska Press.

Sturm, M., J. Holmgren, and G. E. Liston (1995), A seasonal snow cover classification system for local to global applications, *Journal of Climate*, *8*(5), 1261–1283, doi: 10.1175/1520-0442(1995)008<1261:ASSCCS>2.0.CO;2.

Tape, K. D., N. Rutter, H-P. Marshall, R. Essery, and M. Sturm (2010), Recording microscale variations in snowpack layering using near-infrared photography, *Journal of Glaciology*, *56*(195), 75–80, doi: 10.3189/002214310791190938.

Tsoar, H. (2001), Types of aeolian sand dunes and their formation, *Geomorphological Fluid Mechanics*, doi: 10.1007/3-540-45670-8_17.

Watanabe, O. (1978), Distribution of surface features of snow cover in Mizuho plateau, *Memoirs of National Institute of Polar Research*, pp. 44–62.

Werner, B. (1995), Eolian dunes: Computer simulations and attractor interpretation, *Geology*, *23*(12), 1107–1110, doi: 10.1130/0091-7613(1995) 023<1107.

Werner, B. (2003), Modeling landforms as self-organized, hierarchical dynamical systems, *Prediction in geomorphology*, pp. 133–150, doi: 10.1029/135GM10.

APPENDIX A

Snow Bedforms Model Sensitivity Analysis

Introduction

The supporting information presented here comprises a sensitivity analysis of the dune formation model presented in section 2.4 of the main paper. The sensitivity analysis focuses on the impact of the three input variables, bulk snow density, aerodynamic roughness length, and sintering rate, on the model outcomes (Figure 2.12).

The dune formation model describes the growth dynamic of a 2-dimensional dune under the effect of sintering. The dynamic of the dune is captured by its propagation speed (c) and its height (h), which are driven by the wind speed and the wind speed threshold for snow erosion (snow surface condition). The model, being a simplification and abstraction of the actual processes, can be used to reveal the overall effect of sintering of snow particles on the development of a snow dune, but should not be relied on to provide specific values of speed, height and so on.

First, the model computes the necessary flux to sustain a given dune dynamic (h, c). Then by solving Iversen's equation (Equation 2.9) for $U*$, we can estimate the wind speed necessary to sustain this flux. Using Equation 2.4, we then convert the resulting $U*$ to U. The model was implemented in R; the code is attached.

Table A1 provides the input parameters used in the sensitivity analysis. These input parameters are: snow bulk density of the dune ($\rho_{snow\ bulk}$), the surface roughness length (z_a), and the sintering rate of Equation 2.14. We chose to provide the model four runs for each variable we test. The reference run corresponds to the run presented in the main paper, and is based on credible values for the 3 input parameters.

Table A.1: Input parameters for the sensitivity analysis.

	Reference run	Sensitivity values for $\rho_{snow\ bulk}$	Sensitivity values for z_o	Sensitivity values for the sintering rate
$\rho_{snow\ bulk}$ [kg m^{-3}]	350	100 200 400	350	350
Z_o [mm]	1	1	0.1 10 100	1
Sintering rate [kg (hr m^2)$^{-1}$]	0.15	0.15	0.15	0.1 0.2 0.3

Results from the sensitivity test of $\rho_{snow\ bulk}$:

The bulk density included in Equation 2.10 (Chapter 2) affects the flow of transported snow. As the density of a dune increases, the flux of snow required to propagate the dune (at a fixed height and at the same speed) must increase. As a consequence, the wind required to move the amount of snow must increase too (Figure A.1).
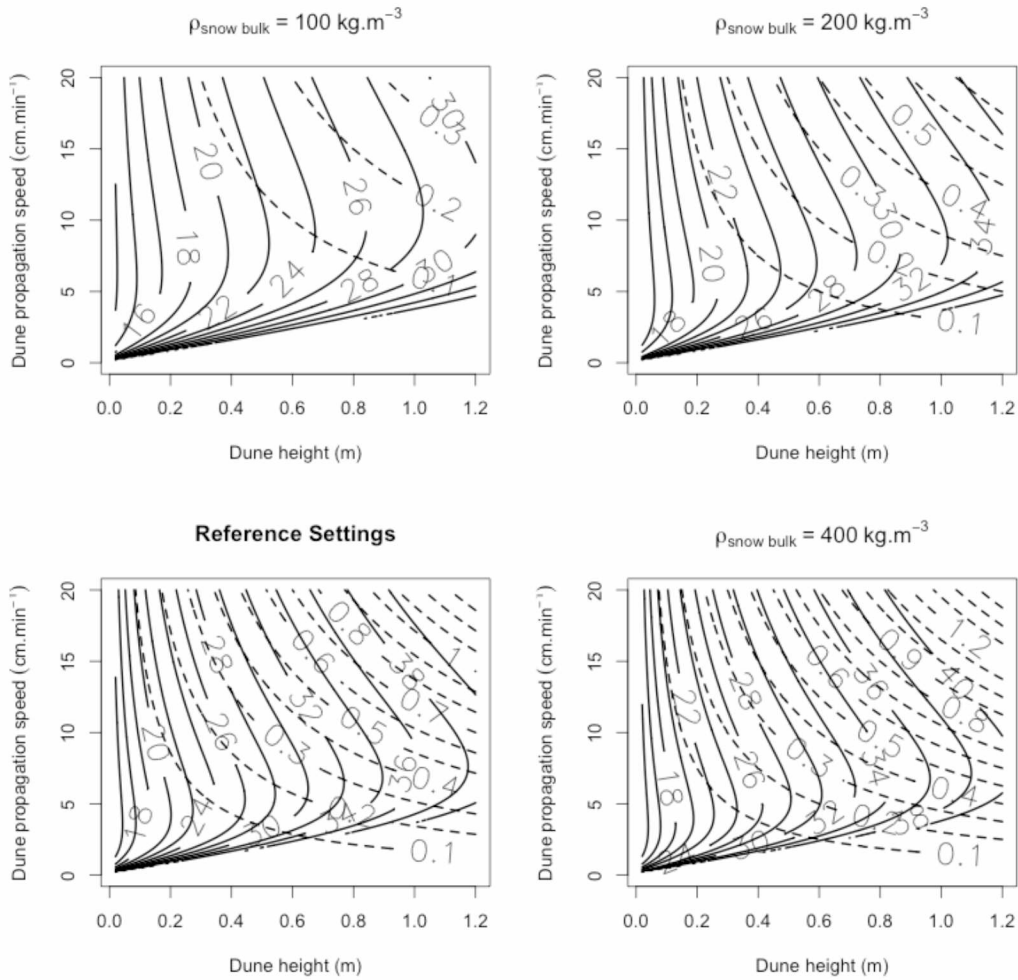
Figure A.1: Sensitivity test of the model to the bulk density of the snow dune. Dotted contour lines show the flux of snow (kg (s m)$^{-1}$), and plain contour lines show the wind speed (m s^{-1}) necessary to support the flux of saltating snow.

Results of the sensitivity test of roughness length

The roughness length is used in the model to convert U_{th} to $U_{th}*$ based on the formulation of Equation 2.4, and to convert $U*$ to U. A shorter roughness length implies a lower wind speed threshold. As a result, the wind speed necessary to sustain a given flux has to increase as z_o decreases (Figure A.2).
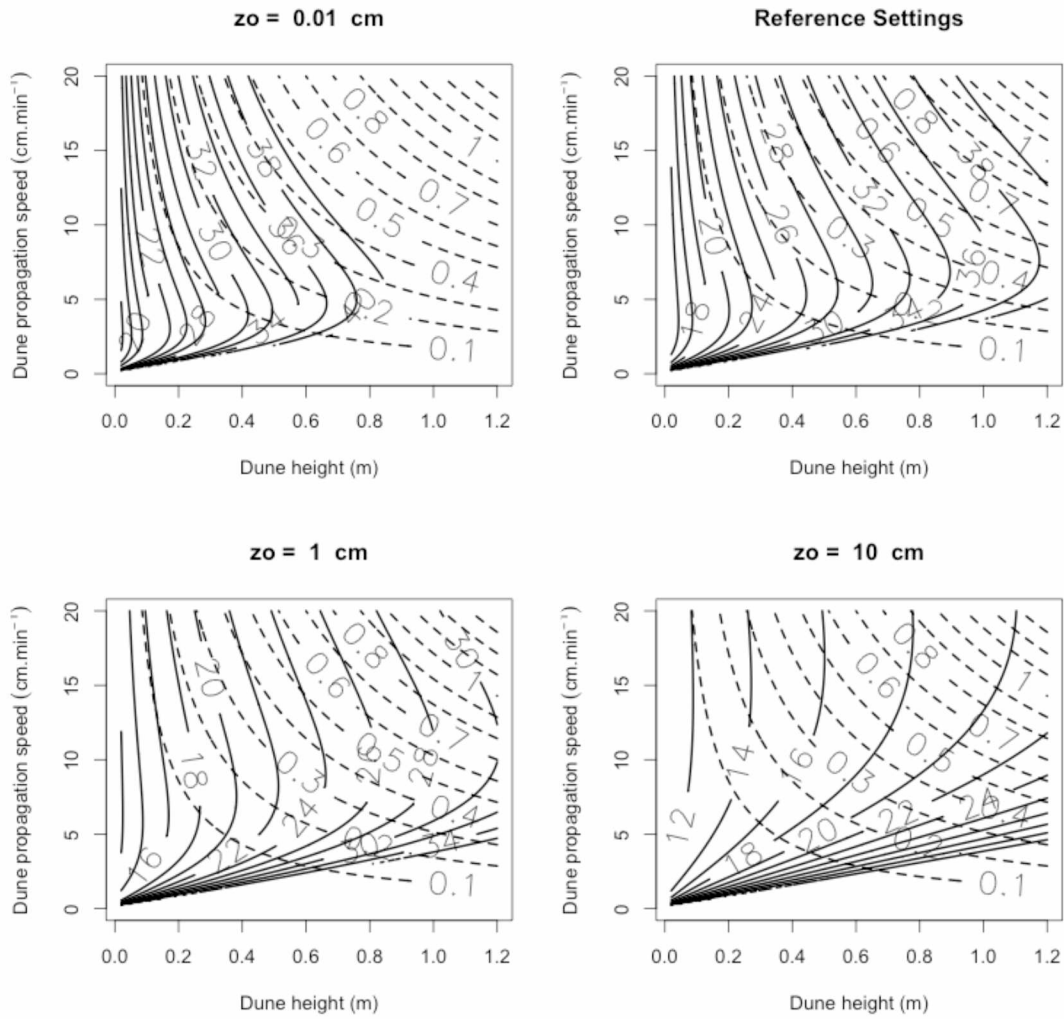
Figure A.2: Sensitivity analysis of the roughness length. Dotted contour lines show the flux of snow (kg (s m)$^{-1}$), and plain contour lines show the wind speed (m s^{-1}) necessary to support the flux of saltating snow.

Results of the sensitivity test for sintering rate.

We simulated three extra sintering paths for the snow based on simple linear function (Figure A.3). We tested our model for one sintering rate slower than the one used in the paper (0.1(red line)), and two sintering rates greater than the original assumption (green and purple lines, 0.2 and 0.3 respectively).

As expected, as sintering happens faster, the wind speed to sustain a given flux has to increase faster in order to counteract the increasing threshold for erosion (Figure A.4).
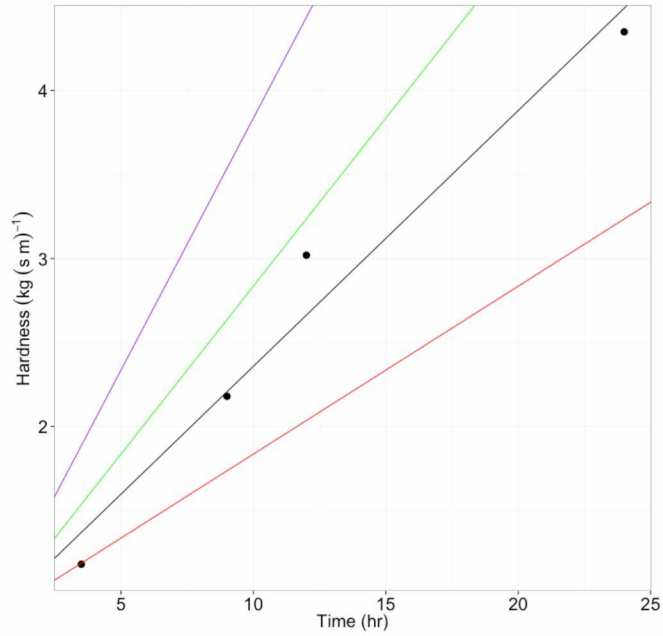
Figure A.3: Sintering paths. Black dots are the data from *Gow and Ramseier* [1964] fitted by the black line. The red line corresponds to a sintering rate of 0.1, the green line to a sintering rate of 0.2, and the purple line to a sintering rate of 0.3.
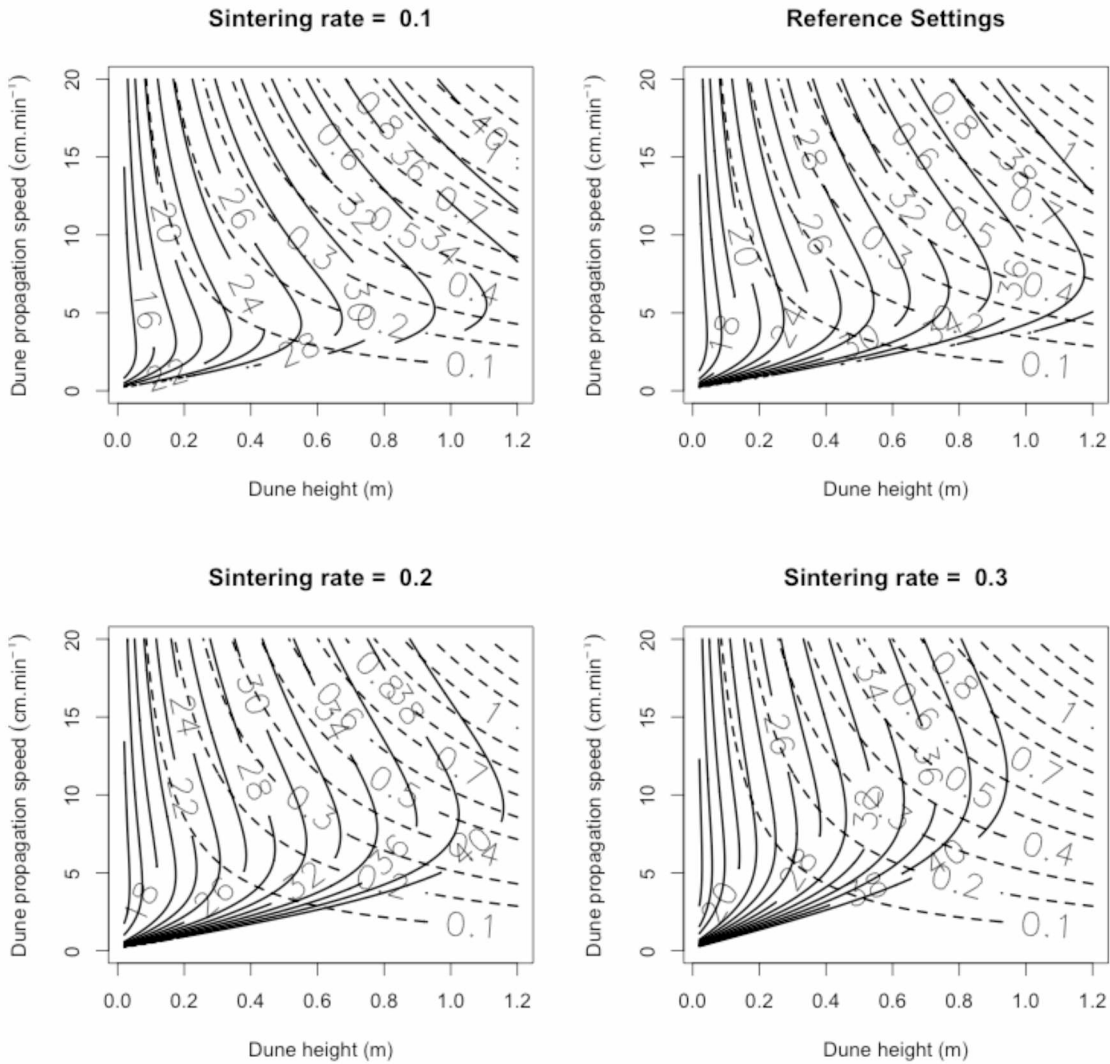
Figure A.4: Sensitivity analysis of the sintering rate. Dotted contour lines show the flux of snow (kg (s m)$^{-1}$), and plain contour lines show the wind speed (m s^{-1}) necessary to support the flux of saltating snow.

Summary

To understand in greater detail the influence of each input parameter on the outcome, Figure A.5 shows for a dune of 50 cm high propagating at a speed of 5 cm s^{-1} how the flux and/or wind speed must vary. We observe that the flux is only affected by the bulk density of the snow whereas the wind speed is greatly influenced by other parameters. This is due to the fact that the flux only depends on c, h, and $\rho_{\text{snow bulk}}$ in Equation 2.10.

The roughness length and the sintering rate are the two parameters having the greatest impact on the model results. These two parameters are also the most variable in real conditions. However, despite the variability of input parameters accounted in the sensitivity analysis, we observe that the behavior of snow dunes remain the same. Sintering remains a limiting factor for the growth of snow dune, with the example in the main text still a valid case likely representative of natural conditions.
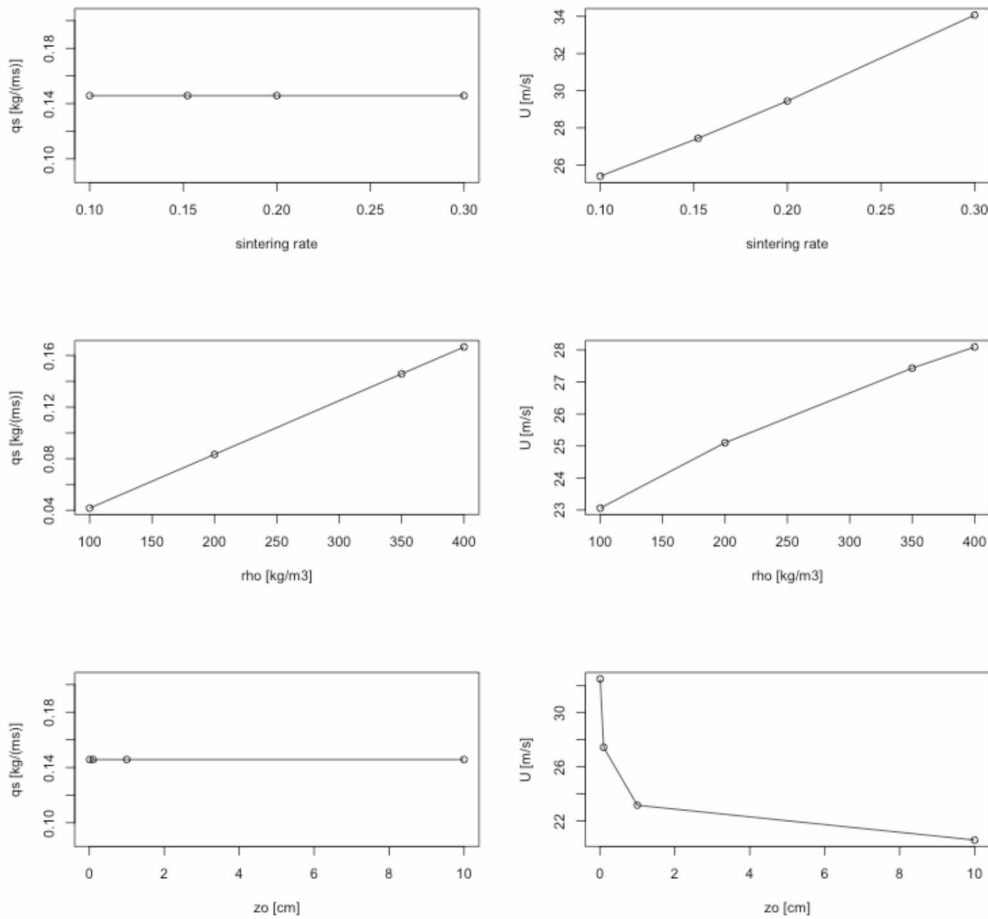
Figure A.5: Sensitivity analysis of the flux q_s and the wind speed U for the three input parameters sintering rate, snow bulk density ($\rho_{\text{snow bulk}}$), and roughness length (z_o). Results plotted are for a dune of 50cm tall propagating at 5 cm s^{-1}.

R-code implementation of the sensitivity analysis.

This code can be run independently by simply copy-paste it into a R-script.

```
# Simon Filhol, May 2015
# Sensitivity Analysis

# This script is a sensitivity analysis for the model presented in the paper titled:
```

```r
# Snow Bedforms: A Review, New Data, and a Formation Model, Filhol and Sturm
library(ggplot2)

my.model <- function(c,h,rho.snow.bulk, L, gow.coeff, z, zo){
  Q <- rho.snow.bulk*h%*%t(c/60*.01)
  Age <- (L)%*%t(1/(c/6000))/3600
  Age[Age>24] <- NA  # ignore dunes older than 24hrs
  H <- gow.coeff[1]+gow.coeff[2]*Age
  Uth <- (.75+H)/.15
  Uth_star <- Uth*.4/(log(z/zo))  # convert threshold wind speed to threshold friction velocity
  # Numerical solver for the cubic polynomial. Output is Ustar
  Ustar <- Q*NA
  for(i in 1:length(h)){
    for(j in 1:length(c)){
      if(!is.na(Uth_star[i,j])){
        FF <- (polyroot(c(-Q[i,j],0,-(1.33/9.8*Uth_star[i,j]),(1.33/9.8))))
        FFim <- abs(Im(FF))<1E-10
        Ustar[i,j] <-Re(FF[FFim])
      }
    }
  }
  U <- Ustar*log(z/zo)/.4  # convert Ustar to wind speed
  return(list("Q"=Q, "U"=U))
}


# Reference run ====
# Input parameters
c <- seq(0,20,.1)
h <- seq(.02,1.2,.01) #vector of possible dune height in (m)
rho.snow.bulk  <- 350 #kg/m3
L <- 1.38+51.29*h
t.gow <- c(3.5,9,12,24) # data table AII Series B
H.gow <- c(1.18,2.18,3.02,4.35) # data table AII Series B
gow.coeff <- summary(lm(H.gow~t.gow))$coeff[,1]
gow.coeff
z <- 100 #cm
zo <- .1 #cm

result.ref <- my.model(c,h,rho.snow.bulk, L, gow.coeff, z, zo)

par(mfrow=c(1,1))
contour(h,c,result.ref$Q,xlab='Dune height (m)',ylab='Dune propagation speed (cm/min)',main="Reference",labcex=1.5,lwd=2, lty=2,
levels=seq(0,10,0.1) )
contour(h,c,result.ref$U,levels=seq(0,60,2),add=TRUE,labcex=1.5,lwd=2,lablwd=10)

# Influence of Snow density ====
rho.snow.bulk1  <- 100 #kg/m3
rho.snow.bulk2  <- 200 #kg/m3
rho.snow.bulk3  <- 400 #kg/m3
result.1 <- my.model(c,h,rho.snow.bulk1, L, gow.coeff, z, zo)
result.2 <- my.model(c,h,rho.snow.bulk2, L, gow.coeff, z, zo)
result.3 <- my.model(c,h,rho.snow.bulk3, L, gow.coeff, z, zo)

par(mfrow=c(2,2))
contour(h,c,result.1$Q,xlab='Dune    height    (m)',ylab='Dune    propagation    speed    (cm/min)',main=paste('Rho    snow    =    ',
as.character(rho.snow.bulk1),' kg/m3'),labcex=1.5,lwd=2, lty=2, levels=seq(0,10,0.1) )
contour(h,c,result.1$U,levels=seq(0,40,2),add=TRUE,labcex=1.5,lwd=2,lablwd=10)
contour(h,c,result.2$Q,xlab='Dune    height    (m)',ylab='Dune    propagation    speed    (cm/min)',main=paste('Rho    snow    =    ',
as.character(rho.snow.bulk2),' kg/m3'),labcex=1.5,lwd=2, lty=2, levels=seq(0,10,0.1) )
contour(h,c,result.2$U,levels=seq(0,40,2),add=TRUE,labcex=1.5,lwd=2,lablwd=10)
contour(h,c,result.ref$Q,xlab='Dune      height      (m)',ylab='Dune      propagation      speed      (cm/min)',main="Reference
Settings",labcex=1.5,lwd=2, lty=2, levels=seq(0,10,0.1) )
contour(h,c,result.ref$U,levels=seq(0,40,2),add=TRUE,labcex=1.5,lwd=2,lablwd=10)
contour(h,c,result.3$Q,xlab='Dune    height    (m)',ylab='Dune    propagation    speed    (cm/min)',main=paste('Rho    snow    =    ',
as.character(rho.snow.bulk3),' kg/m3'),labcex=1.5,lwd=2, lty=2, levels=seq(0,10,0.1) )
contour(h,c,result.3$U,levels=seq(0,40,2),add=TRUE,labcex=1.5,lwd=2,lablwd=10)

Q.rho1 <- result.1$Q[50,50]
Q.rho2 <- result.2$Q[50,50]
Q.rho3 <- result.3$Q[50,50]
U.rho1 <- result.1$U[50,50]
U.rho2 <- result.2$U[50,50]
U.rho3 <- result.3$U[50,50]

# influence of zo ====
zo1 <- .01
zo2 <- 1
zo3 <- 10

result.1 <- my.model(c,h,rho.snow.bulk, L, gow.coeff, z, zo1)
```

```r
result.2 <- my.model(c,h,rho.snow.bulk, L, gow.coeff, z, zo2)
result.3 <- my.model(c,h,rho.snow.bulk, L, gow.coeff, z, zo3)

par(mfrow=c(2,2))
contour(h,c,result.1$Q,xlab='Dune height (m)',ylab='Dune propagation speed (cm/min)',main=paste('zo = ', as.character(zo1),'
cm'),labcex=1.5,lwd=2, lty=2, levels=seq(0,10,0.1) )
contour(h,c,result.1$U,levels=seq(0,40,2),add=TRUE,labcex=1.5,lwd=2,lablwd=10)
contour(h,c,result.ref$Q,xlab='Dune          height          (m)',ylab='Dune          propagation          speed          (cm/min)',main="Reference
Settings",labcex=1.5,lwd=2, lty=2, levels=seq(0,10,0.1) )
contour(h,c,result.ref$U,levels=seq(0,40,2),add=TRUE,labcex=1.5,lwd=2,lablwd=10)
contour(h,c,result.2$Q,xlab='Dune height (m)',ylab='Dune propagation speed (cm/min)',main=paste('zo = ', as.character(zo2),'
cm'),labcex=1.5,lwd=2, lty=2, levels=seq(0,10,0.1) )
contour(h,c,result.2$U,levels=seq(0,40,2),add=TRUE,labcex=1.5,lwd=2,lablwd=10)
contour(h,c,result.3$Q,xlab='Dune height (m)',ylab='Dune propagation speed (cm/min)',main=paste('zo = ', as.character(zo3),'
cm'),labcex=1.5,lwd=2, lty=2, levels=seq(0,10,0.1) )
contour(h,c,result.3$U,levels=seq(0,40,2),add=TRUE,labcex=1.5,lwd=2,lablwd=10)


Q.zo1 <- result.1$Q[50,50]
Q.zo2 <- result.2$Q[50,50]
Q.zo3 <- result.3$Q[50,50]
U.zo1 <- result.1$U[50,50]
U.zo2 <- result.2$U[50,50]
U.zo3 <- result.3$U[50,50]

par(mfrow=c(1,2))
plot(c(zo1,zo,zo2,zo3),c(result.1$Q[50,100],result.ref$Q[50,100],result.2$Q[50,100],result.3$Q[50,100]),xlab='zo',ylab='Q')
plot(c(zo1,zo,zo2,zo3),c(result.1$U[50,100],result.ref$U[50,100],result.2$U[50,100],result.3$U[50,100]),xlab='zo',ylab='U')


# Influence of sintering rate ====
gow.coeff1 <- c(gow.coeff[1],0.1)
gow.coeff2 <- c(gow.coeff[1],0.2)
gow.coeff3 <- c(gow.coeff[1],0.3)

result.1 <- my.model(c,h,rho.snow.bulk, L, gow.coeff1, z, zo)
result.2 <- my.model(c,h,rho.snow.bulk, L, gow.coeff2, z, zo)
result.3 <- my.model(c,h,rho.snow.bulk, L, gow.coeff3, z, zo)

par(mfrow=c(2,2))
contour(h,c,result.1$Q,xlab='Dune      height      (m)',ylab='Dune      propagation      speed      (cm/min)',main=paste('Sintering   rate   = ',
as.character(gow.coeff1[2])),labcex=1.5,lwd=2, lty=2, levels=seq(0,10,0.1) )
contour(h,c,result.1$U,levels=seq(0,40,2),add=TRUE,labcex=1.5,lwd=2,lablwd=10)
contour(h,c,result.ref$Q,xlab='Dune          height          (m)',ylab='Dune          propagation          speed          (cm/min)',main="Reference
Settings",labcex=1.5,lwd=2, lty=2, levels=seq(0,10,0.1) )
contour(h,c,result.ref$U,levels=seq(0,40,2),add=TRUE,labcex=1.5,lwd=2,lablwd=10)
contour(h,c,result.2$Q,xlab='Dune      height      (m)',ylab='Dune      propagation      speed      (cm/min)',main=paste('Sintering   rate   = ',
as.character(gow.coeff2[2])),labcex=1.5,lwd=2, lty=2, levels=seq(0,10,0.1) )
contour(h,c,result.2$U,levels=seq(0,40,2),add=TRUE,labcex=1.5,lwd=2,lablwd=10)
contour(h,c,result.3$Q,xlab='Dune      height      (m)',ylab='Dune      propagation      speed      (cm/min)',main=paste('Sintering   rate   = ',
as.character(gow.coeff3[2])),labcex=1.5,lwd=2, lty=2, levels=seq(0,10,0.1) )
contour(h,c,result.3$U,levels=seq(0,40,2),add=TRUE,labcex=1.5,lwd=2,lablwd=10)

par(mfrow=c(1,1))
ggplot()+geom_point(aes(x=t.gow,y=H.gow),size=4)+
  geom_abline(intercept=gow.coeff[1],slope=gow.coeff[2])+
  geom_abline(intercept=gow.coeff1[1],slope=gow.coeff1[2], colour='red')+
  geom_abline(intercept=gow.coeff2[1],slope=gow.coeff2[2], colour='green')+
  geom_abline(intercept=gow.coeff3[1],slope=gow.coeff3[2], colour='purple')+
  theme_bw()+xlab("Time (hr)")+
  ylab("Hardness ()")+
  theme(axis.text=element_text(size=20),axis.title.y = element_text(size = 20), axis.title.x = element_text(size = 20))

Q.sint1 <- result.1$Q[50,50]
Q.sint2 <- result.2$Q[50,50]
Q.sint3 <- result.3$Q[50,50]
U.sint1 <- result.1$U[50,50]
U.sint2 <- result.2$U[50,50]
U.sint3 <- result.3$U[50,50]

# Influence on Q and U of the input parameters:
par(mfrow=c(3,2))
plot(c(gow.coeff1[2],gow.coeff[2],gow.coeff2[2],gow.coeff3[2]),c(Q.sint1,result.ref$Q[50,50],Q.sint2,Q.sint3),xlab='sintering
rate',ylab='Q [kg/(ms)]',type='l')
points(c(gow.coeff1[2],gow.coeff[2],gow.coeff2[2],gow.coeff3[2]),c(Q.sint1,result.ref$Q[50,50],Q.sint2,Q.sint3))
plot(c(gow.coeff1[2],gow.coeff[2],gow.coeff2[2],gow.coeff3[2]),c(U.sint1,result.ref$U[50,50],U.sint2,U.sint3),xlab='sintering
rate',ylab='U [m/s]',type='l')
points(c(gow.coeff1[2],gow.coeff[2],gow.coeff2[2],gow.coeff3[2]),c(U.sint1,result.ref$U[50,50],U.sint2,U.sint3))

plot(c(rho.snow.bulk1,rho.snow.bulk2,rho.snow.bulk,rho.snow.bulk3),c(Q.rho1,Q.rho2,result.ref$Q[50,50],Q.rho3),xlab='rho
[kg/m3]',ylab='Q [kg/(ms)]',type='l')
```

```
points(c(rho.snow.bulk1,rho.snow.bulk2,rho.snow.bulk,rho.snow.bulk3),c(Q.rho1,Q.rho2,result.ref$Q[50,50],Q.rho3))
plot(c(rho.snow.bulk1,rho.snow.bulk2,rho.snow.bulk,rho.snow.bulk3),c(U.rho1,U.rho2,result.ref$U[50,50],U.rho3),xlab='rho
[kg/m3]',ylab='U [m/s]',type='l')
points(c(rho.snow.bulk1,rho.snow.bulk2,rho.snow.bulk,rho.snow.bulk3),c(U.rho1,U.rho2,result.ref$U[50,50],U.rho3))

plot(c(zo1,zo,zo2,zo3),c(Q.zo1,result.ref$Q[50,50],Q.zo2,Q.zo3),xlab='zo [cm]',ylab='Q [kg/(ms)]',type='l')
points(c(zo1,zo,zo2,zo3),c(Q.zo1,result.ref$Q[50,50],Q.zo2,Q.zo3))
plot(c(zo1,zo,zo2,zo3),c(U.zo1,result.ref$U[50,50],U.zo2,U.zo3),xlab='zo [cm]',ylab='U [m/s]',type='l')
points(c(zo1,zo,zo2,zo3),c(U.zo1,result.ref$U[50,50],U.zo2,U.zo3))
```

Reference

Gow, A. J., and R. O. Ramseier (1964), Age hardening of snow at the South Pole, *Tech. rep.*, DTIC Document.

CHAPTER 3: How Falling and Settling of Snowflakes Smooth a Landscape[1]

Abstract

Every winter, the scenery of northern landscapes is smoothed by snow deposition in calm conditions (no wind). In this study we investigate how snow falling uniformly can attenuate topographic relief at scales smaller than, or equivalent to, the snow depth. Based on a set of three experiments we observed smoothing processes at the grain scale along with their cumulative effect at the snowpack scale. The experiments consisted of 1) a strobe-light box for tracking the trajectories of snowflakes at deposition, 2) a closed-box experiment looking at the effects of a spatially constrained vertical influx on the accumulation of snow, and 3) a set of artificial surfaces of various sizes on which natural snow was allowed to accumulate. We found that smoothing requires the lateral displacement of snow particles, but unlike sand, snow presents unique behaviors and more processes that enhance (bouncing, ejection, breakage, fall trajectory, creep, metamorphism, fall spatial variability) or restrain (interlocking, cohesion, adhesion, sintering) the rate of smoothing. In common with sand and other granular materials, smoothing of the snow surface is driven by the curvature of the surface topography, but unlike sand, snow can sustain steeper angles of repose and can bridge gaps. Our findings suggest that better understanding the processes behind smoothing could provide new insight into evolution of snow depth variability and snow and vegetation interactions.

3.1 Introduction

"On top of this ice were as many feet of snow. It was all pure white, rolling in gentle undulations where the ice-jams of the freeze-up had formed."

Jack London, To Build a Fire, 1908.

Jack London in his short story To Build a Fire, describes how the massive jumbled ice blocks of the Yukon River had been covered and smoothed by snow. His description is not only accurate, but this ability of snow to smooth and soften a landscape (Figure 3.1) is universally recognized. Moreover,

---

[1] Filhol, S., and M. Sturm (2016), How Falling and Settling of Snowflakes Smooth a Landscape, Prepared for submission to the Journal of Geophysical Research Earth Surface

69

artists and poets often use the smoothing property of snow as an allegory for evoking feelings such as cleansing, purity, and softness [*Gautier*, 1890; *Burnside*, 2013]. But the actual physical processes driving smoothing of the underlying surface topography by snow deposited in the absence of wind are poorly understood.

Figure 3.1: In this oil painting by *Grant Wood* [1940] snow smooths the Iowa landscape, imparting a bleak but serene feel.

There are practical reasons why we might need to know how snow smooths a landscape. For example, in order to assess the trafficability of snow surfaces, we might want to know the damping effect of snow as a function of snow depth and the underlying roughness. Even more basic, depth is the most common measurement made on snow, essential when trying to estimate and model water storage in a basin. Understanding the processes controlling the lateral redistribution of snow on the ground (and therefore the depth variance) is needed for successful sampling. But the most compelling reason for seeking knowledge on snow smoothing is that it is fundamental to the redistribution of snow in a landscape. All over the snow-covered world, some 45 million km^2 in the Northern Hemisphere alone, millimeter-scale snow grains moving laterally during and following deposition transform the Earth's surface across fields, hills, and forests. The very "look" of the

winter reflects how an immense number of these small grain movements, some 10^{19} grains in motion at any one time, combine to smooth and soften the world.

We ask two questions:

- *Which grain-scale processes promote or restrain snow smoothing of the underlying landscape?*
- *At the snowpack scale, how does the smoothing proceed, and what factors accelerate or retard it?*

While there is a general understanding of what "smoothing a surface" means, the precise definition varies from mathematics (having continuous derivatives to some n^{th} order) to woodworking (free from irregularities, roughness, or projections), and implies a particular scale. Here our scale is on the order of the snow depth (several meters), about a thousand times larger than the grain scale surface roughness of snow [*Löwe et al.*, 2007], and our definition includes in it a reduction in surface irregularities and a dampening of the amplitude of bumps (micro-topographic features) under the snow. We explored the answers to questions 1 and 2 through a series of experiments, and based on these and prior research, propose a general description of snow smoothing.

3.2 Background

If snow falls evenly on a smooth, flat surface, without wind, the snow-atmosphere interface will remain flat at a scale larger than the grain scale, but if the original surface is not flat, the snow-atmosphere interface will become smoother than the underlying relief as the snow deepens. This process requires the lateral displacement of snow grains, which begins when snowflakes, single crystals or at higher temperatures (~0°C) clumps of crystals, accumulate on the ground and on top of each other. As the snowflakes collide with the surface or with previously deposited flakes, they bounce, break into multiple pieces, and come to rest through dissipation of their kinetic energy. They can eject or dislodge other grains (splash), altering the overall arrangement of grains at the surface. Higher fall speeds and greater snowflake mass favor bigger bounces, more breakage and ejection, and therefore a higher probability of lateral motion[2]. Once deposited, the grains settle and deform, cascading downslope singly or en masse if gravitational forces exceed cohesive forces (here

---

[2]   For a surface of constant elastic properties, heavier falling particles approaching the surface with greater momentum will bounce higher/further than lighter particles.

we are focused on small-scale sloughing, not avalanching), again producing some lateral motion. Cavities under the snow surface can develop when the snow bridges gaps, creating airspaces (subnivean space) important to both animals and plants [*Korslund and Steen*, 2006], a process that can also accelerate smoothing. While some of these processes are similar for granular materials like sand (*e.g.* bouncing), others (*e.g.* breakage, sintering, deformation, metamorphism) are unique to snow.

There has been considerable work on the fall speed of snowflakes [*e.g. Locatelli and Hobbs*, 1974; *Mellor and Mellor*, 1988], but of more interest to us here is what happens once the grains hit the surface. *Kuroiwa et al.* [1967], studying the micromechanical properties of snow, found that the angle of repose depended mainly on grain shape and temperature, with the steepest angles forming at the highest temperatures. Snow piles were observed to be much steeper than granular materials like sand because of the interlocking dendritic shape of snowflakes and the cohesive forces between grains produced by the liquid-like layer found on snow grains [*Faraday*, 1850; *Sazaki et al.*, 2012]. This early work was followed by experiments by *Wakahama et al.* [1978] on snow accumulation on power lines. Their work showed that even at above-freezing temperatures (+4°C) snowflakes bounced and broke into pieces when they impacted a cable. *Kobayashi* [1987] continued this line of inquiry, discovering that at temperatures above -4°C the accumulation of snow on flat boards was enhanced. Using ice spheres bouncing on an ice plate, Kobayashi observed a rapid reduction in the restitution of energy at impact for temperature above -4°C. There have also been many studies [*e.g. Miller* 1964; *Bunnell et al.*, 1985; *Schmidt and Gluns, 1991; Pfister and Schneebeli*, 1999] focusing on snow interception by tree canopies that not only identified similar modes of grain-scale motion, but also demonstrated the importance of snow bridging in forming a continuous snow cover in tree branches, a process that would not occur if the material was sand.

Valuable information on snow smoothing has also come from studies on the evolution of interfaces [*Barabási and Stanley*, 1995]. Based largely on theoretical work, multiple continuous and discrete models have been developed that capture the behavior of a wide range of interface phenomena including modeling the shape of a coffee stain on fabric [*Deegan et al.*, 1997; *Yunker et al.*, 2013] and the dynamics of growing sand piles [*Mehta et al.*, 1996], often applying the theory of fractals to describe the roughening or smoothing of these interfaces. *Löwe et al.* [2007] and *Manes et al.* [2008] found that for snow, a ballistic model [*Vold*, 1963] was useful in describing the evolution of snow surface roughness at the grain scale. At the larger scale of interest here, the Edwards and Wilkinson

equation (EW equation) [*Edwards and Wilkinson*, 1982] has been used to imitate snow smoothing in virtual landscapes [*Festenberg and Gumhold*, 2011]. The EW equation is effectively a diffusive equation that tracks the rate at which the height and geometry of a surface changes under the aggregation of individual particles. Surface curvature drives particle rearrangement. The EW equation is a special case of the Kardar-Parisi-Zhang equation (KPZ)[*Kardar et al.*, 1986], which includes a nonlinear term based on the surface slope as well as a linear term driven by surface curvature. In both models, individual grain processes are not described, but rather represented by bulk coefficients.

Finally, useful information on snow smoothing has come from the world of computer graphics. Driven by aesthetic criteria rather than physical realism, the computer vision community has produced interesting approaches to simulate snow in video games and animated movies (*e.g.* the Disney Studio animated movie *Frozen*, using the model described in *Stomakhin et al.*, [2013]). As mentioned before, *Festenberg and Gumhold* [2011] implemented the EW equation to simulate the smoothing effect, but had to implement an arbitrary algorithm for mimicking bridging. The virtual scenes produced are remarkable to the eye, suggesting that at least in form, the numerical solutions achieved to date are reasonable.

3.3 Experiments

We ran three types of experiments to observe processes producing lateral displacement of snow grains during deposition, as well as bulk smoothing processes during and following deposition. To observe how snowflakes moved laterally when they impacted a surface (including one covered with snow) we (1) used a high-frequency strobe light and video camera to photograph falling and bouncing snowflakes. To observe the bulk smoothing behavior of snow we (2) allowed snow to fall through a narrow gap in a closed box with flat bottom and then examined the shape of the resulting deposits, and we (3) watched the build-up of snow on tables equipped with artificial relief in the form of bumps of various sizes, shapes, and spacing. All experiments were run under natural snowfall in calm conditions in a small clearing surrounded by trees (>5 m tall) of the boreal forest shadowing winds at the experiment's location, near the University of Alaska at Fairbanks, Alaska.

3.3.1 Methods

3.3.1.1 Snowflake Impacts Tracked with a Strobe-light

A dark box illuminated by a strobe light (Figure 3.2) was used to photograph falling snowflakes. The box was fully covered except for an open slot 4 cm wide parallel to the camera sensor plane. The strobe light had an adjustable frequency. In most cases 200 Hz was found to be a good compromise to visualize both rapidly falling snowflakes and slower flakes after bouncing. The strobe light was built using white LED strips connected to an open-source microcontroller Arduino® (www.arduino.cc). The frequency accuracy of the strobe was checked using an oscilloscope. The video camera was a digital single-lens reflex camera Canon 60D. The camera was set in video mode at 30 frames/second with a resolution of 1920*1080 pixels. The exposure time was fixed at 1/30 s, while the aperture and the sensor sensitivity (*i.e.* ISO) were optimized for a balanced exposure of the image. We placed various shapes and surface types (metal, wood, branch, snow) under the gap.
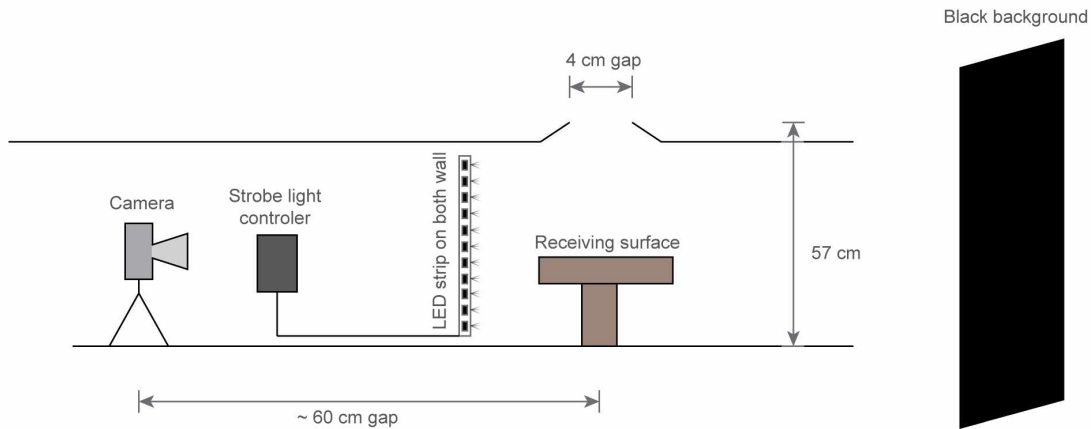
Figure 3.2: The experimental setup used in observing falling and bouncing snowflakes. The setup was enclosed into a black tunnel-like box with a black backdrop at its end to obtain maximum contrast between the snowflakes and the background.

The videos were split into individual images that were processed using the library OpenCV [*Bradski,* 2000] by converting them to grayscale images, and then applying a threshold filter to differentiate the falling snowflake tracks from the black background. The pixels were scaled using objects of a known size in the picture frame. To estimate fall speed, fall direction, and size of falling flakes, we cropped the images to the upper 400 pixels, and extracted the location of the snowflake tracks from

the thresholded images with a blob detection algorithm [*Shapiro*, 1992] as provided in the OpenCV library.

3.3.1.2 Snow Deposition Through a Gap

We allowed snow to deposit in a closed box 62 cm deep and 100 cm long with an open slot 4 cm wide at the top. The snowflakes deposited on a flat wooden surface as well as on the top of the box adjacent to the slot (Figure 3.3). We sectioned and photographed the cross profile of the freshly deposited snow against a dark gridded card, then digitized the shape of the snow section. Multiple sections were obtained by cutting back along the deposit in a series of slices. In between each storm, the box was emptied and the top cleared so that the next storm deposited snow on a clean base and top. For each event we also recorded the total snow accumulated on a nearby flat surface.
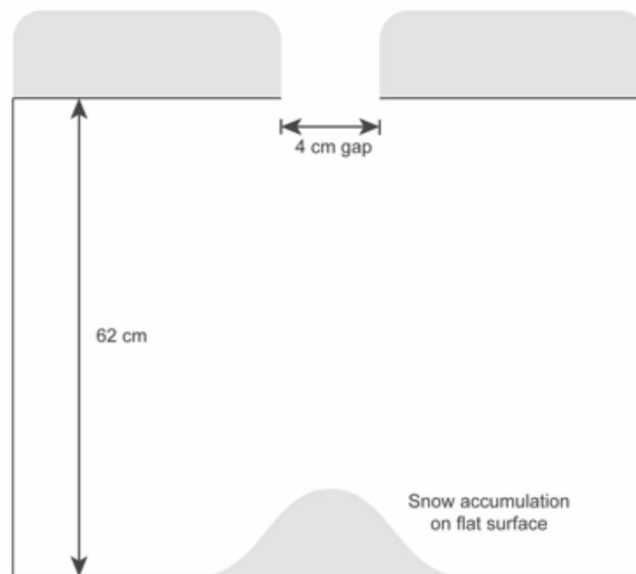
Figure 3.3: Closed box with a 4 cm gap that allowed snow to accumulate on the box floor.

3.3.1.3 Snow Deposition over Artificial Relief

During two winter seasons (2012-2013, 2014-2015), we installed artificial bumps of various shapes, sizes, and spacing on outdoor tables and allowed them to be buried by snow. These bumps, actually long ridges, were essentially two-dimensional with respect to snow accumulation, extending back from the table edges about 0.6 m. At the end of each season, we sectioned the snow across the bumps and photographed the sections with a near-infrared (NIR) camera (Fujifilm S9100 digital camera) using the method of *Tape et al.* [2010]. This allowed us to extract the snow stratigraphy in

detail. The tables sat 90 cm above ground, which kept the snow nearly isothermal, inhibiting extreme depth hoar metamorphism [*Trabant and Benson*, 1972; *Sturm and Benson*, 1997]. However, in this installation the snow still underwent some metamorphism, which reduced the mean grain size with time [*Bader et al.*, 1954; *Flin et al.*, 2004; *Dominé et al.*, 2013]. Surface hoar also occasionally formed.

In the winter of 2012-2013, using lumber (3.8 by 8.9 cm in cross section) we installed rectangular periodic surfaces of varying heights and gap widths (Figure 3.4 top and Table 3.1). In the winter of 2014-2015, we installed triangular surfaces made of galvanized steel of two different heights (7.6 and 15.5 cm) and several widths in order to produce triangles with different slope angles (27°, 43°, 55°) (Figure 3.4 bottom). The triangles were set sufficiently far apart so that there was no interference between adjacent profiles, except in two cases where three E-triangles were separated by 15.6 (E1 profile) and 24.9 cm (E2 profile) crest to crest. We installed two sets of tables in 2014-2015 because we hoped to section the snow over a two-month period in order to estimate the effect of creep, but rain and melt events ruined the snow cover before the second set of measurements could be made.
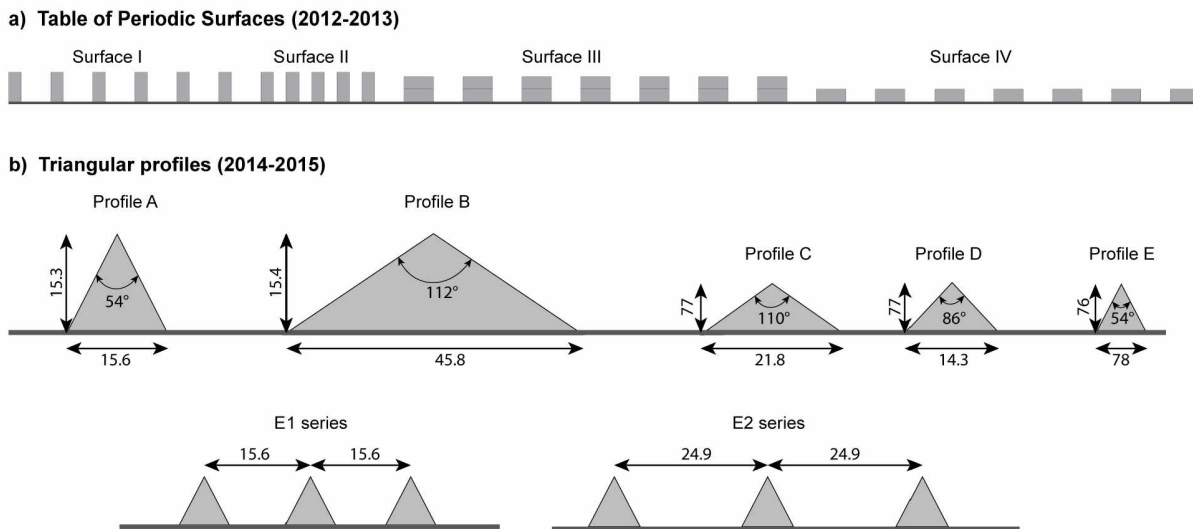
Figure 3.4: Cross profiles of artificial bumps on which snow accumulated. In 2012-2013 (top) we focused on impact of heights and gaps on snow smoothing (Table 3.1), and in 2014-2015 we focused on the impact of slope angle and size. All units are in centimeters.

Table 3.1: Artificial Surfaces, 2012-2013

Surface	Height (cm)	Step width (cm)	Period (cm)	Spacing (cm)
I	8.9	3.8	12.7	8.9
II	8.9	3.8	7.6	3.8
III	7.6	8.9	17.8	8.9
IV	3.8	8.9	17.8	8.9

Our goal was to produce cross sections of the snow over the artificial bumps that revealed the layering (Figure 3.5). The typical processing pipeline was to first geometrically correct the images with the library Lensfun (http://lensfun.sourceforge.net/), then convert the images to black and white, apply a median filter and a local adjustment of the exposure to enhance contrast locally in between layers. For images from the periodic surface table, we then stitched images together using an Adobe Photoshop automatic algorithm as well as manual stitching when the algorithm could not resolve the mosaic. The final stage consisted of scaling the images using objects of a known size in the frame (*i.e.* a ruler). From these processed images we manually extracted relevant metrics including the width and height of undulations in the snow surface in order to track their evolution as snow accumulates. The sharpness (or peakedness) of undulations was quantified by computing both the mean slope and apex angle (Figure 3.5). All the processing algorithms were developed with the programming language Python, using the library Scikit-image [*Van Der Walt et al.*, 2014] for the image enhancement and filtering.
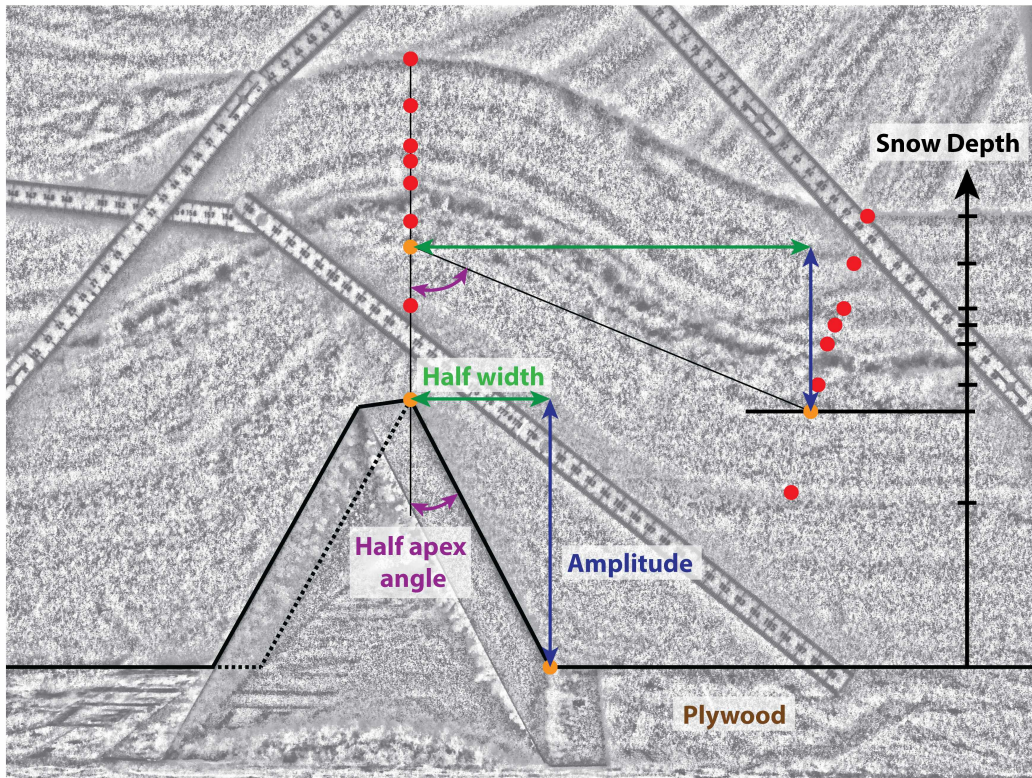
Figure 3.5: Near-infrared photograph of the snowpack covering triangular metal profile A (15.4 high and 15.6 wide). The peaks and bases of nine layers of snow have been identified and marked with red and orange dots.

3.3.2 Results

3.3.2.1 Falling snowflakes at impact

We recorded snowflake trajectories during 5 storms for a cumulative total of 1948 individual measurements. The mean fall speed was 90 ± 2.0 cm s^{-1} (Figure 3.6 and Table 3.2). Because snowflakes have complex geometries and are susceptible to slight air movement and flutter as they fall, resulting in trajectories that are not straight lines. This can produce non-vertical trajectories, though 95% of all snowflakes in the experiment fell within 3.2° of vertical. Since our experiment could not resolve the three-dimensional path of the snowflakes (that would have required two synchronized cameras), the distributions presented in Figures 3.6a and 3.6b represent the projection of a three-dimensional path on a two-dimensional plane. We also could not resolve actual grain sizes and shapes from our images, but the width of the tracks on the images give at least an approximation of snowflake size.

Table 3.2: Snowfall Events Captured using the Strobe Apparatus

Storm	Temp. (°C)	Samples	$\mu_{fall\ direction}$ (°)	$\sigma_{fall\ direction}$ (°)	$\mu_{fall\ speed}$ (cm/s)	$\sigma_{fall\ speed}$ (cm/s)	μ_{width} (cm)	σ_{width} (cm)
I	-22.4	135	-0.6	2.8	86.6	16.1	0.14	0.03
II	-13.1	171	-0.3	3.1	86.4	13.4	0.17	0.05
III	-7.3	65	-1.2	2.5	137.2	52.7	0.22	0.05
IV	-4.3*	407	0	2.4	88.1	16.6	0.18	0.07
V	-0.7**	1170	-0.3	3.6	90	16.3	0.16	0.06

Note: μ = mean value; σ = standard deviation. Measurements marked with * correspond to storm III (*) and storm I (**) of the gap experiment.
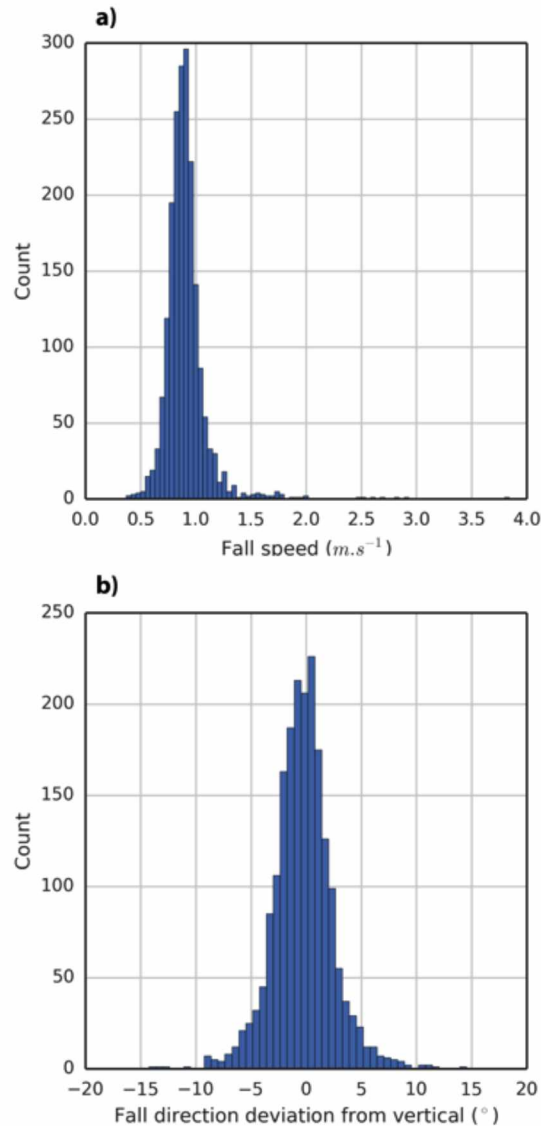
Figure 3.6: Histograms for 1948 snowflake trajectories showing the distribution of fall speed (a), deviation with respect to vertical (b).

The bounce behavior of snowflakes impacting a surface at an air temperature of -4.3 °C (Storm III) is highlighted in Figure 3.7: in 3.7a the snowflakes were falling on wood, whereas in 3.7b they were falling on wood covered by a thin layer of snow (~1 mm). From the wood the flakes bounced as much as 43.8 mm sideways and 23 mm high (Figure 3.7a). Substantial lateral bounce was observed even when the snowflake fall trajectories were vertical. By simply altering the nature of the impact surface (covering it with 1 mm of snow), lateral bouncing was greatly reduced. For example, in Figure 3.7b, the snowflakes bounced only 5.3 mm away from their impact points and jumped only 3.4 mm high, a reduction by a factor of 8.
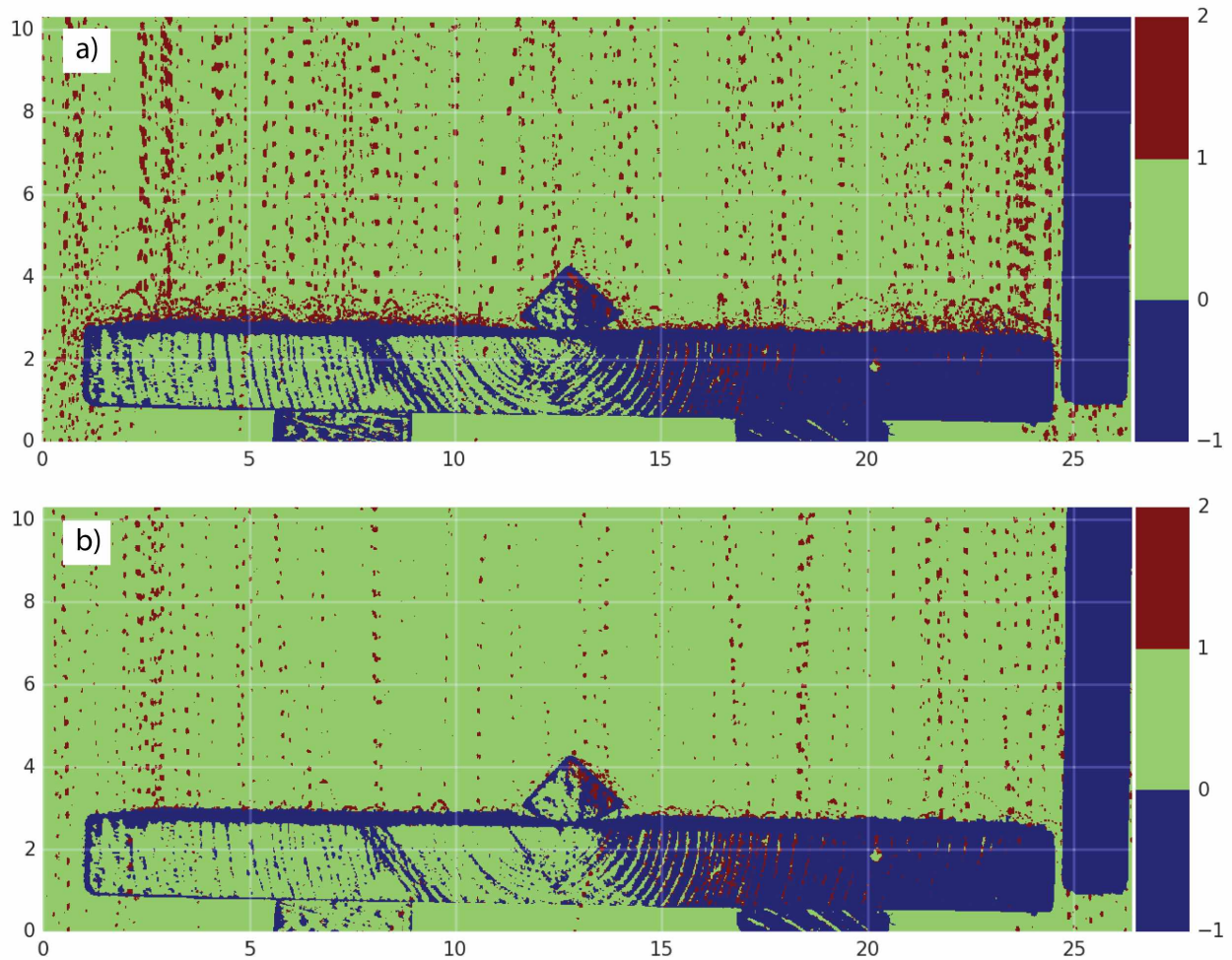
Figure 3.7: Snowflake trajectories during Storm III; a) landing and bouncing on a clean wooden surface (1000 frames combined), b) landing and bouncing on a wood surface covered with a thin (~1mm) layer of snow (2000 frames combined). Notice the significant decrease in bounce height on the snow-covered surface. The gaps in the trajectories are due to the refreshing time of the CMOS sensor of the video camera recording at 30 Hz. In these composite images blue indicates that a pixel reflected the strobe light more than two times (fixed surface). Green means that the pixel never reflected the light (no target), and red indicates the pixels reflected the light only once, the case for falling and bouncing snowflakes. For both composite images the surface temperature was -4.3 °C.

This experimental setup also allowed us to observe the impact of single snowflakes. We placed a 44.5 mm diameter copper pipe in the frame and let snow accumulate on its upper part, then observed impacts. Figure 3.8 shows the three different classes of interactions:

1. *elastic bounce* (Figure 3.8a).
2. *ejection of multiple smaller grains* or *breakage plus ejection* (Figure 3.8b).

3. *retention* at the snow surface due to dissipation of energy and rapid cohesion (Figures 3.8c and 3.8d).

For example, when the snowflake in Figure 3.8c impacted the surface, instead of bouncing it either rolled to its final position, or the impact deformed the lattice of resting snowflakes, pushing them outward. In Figure 3.8d a snowflake falling vertically moved down slope upon impact, ejecting or breaking other snow particles, but one particle remained entangled and moved only a short distance.
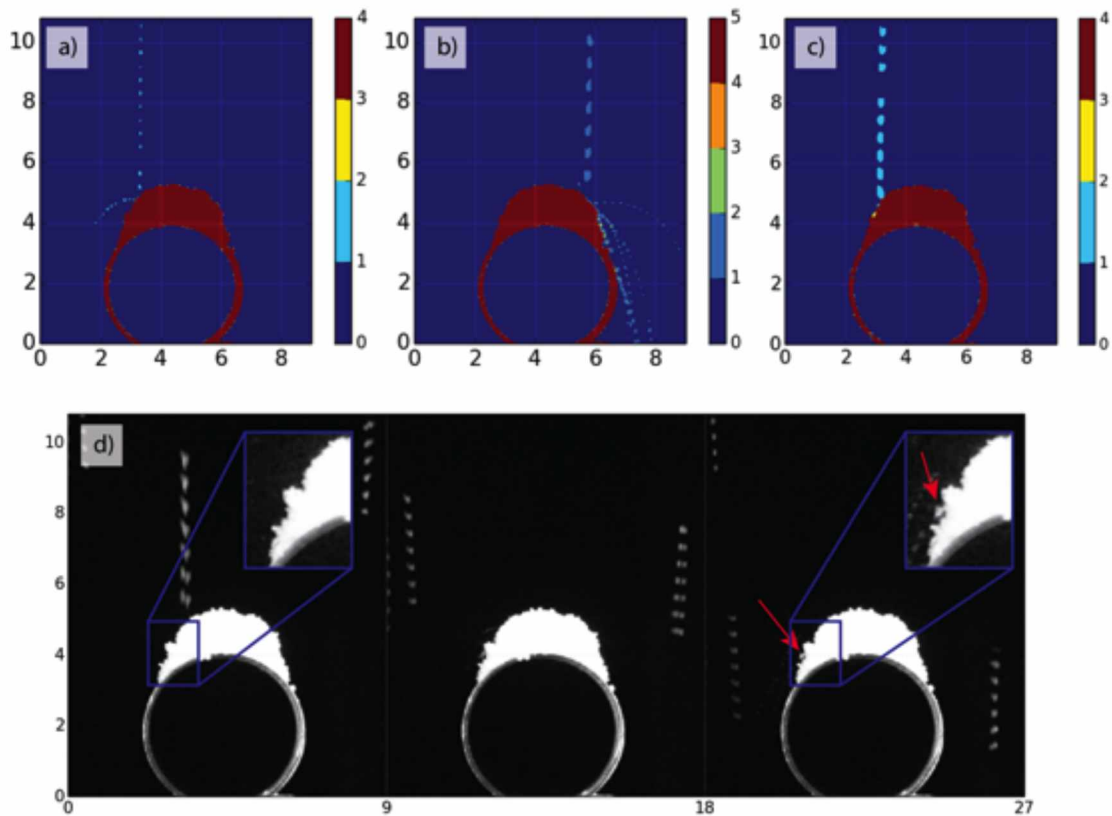
Figure 3.8: Impact interactions of snowflakes with a snow on top of a copper pipe 44.5 mm in diameter: a) bouncing, b) breakage, ejection, and bouncing, c) displacement of surface grains, and possibly downslope rolling, and d) a sequence showing a particle locked in a overhanging situation. In a, b, and c, the color scales correspond to the number of times a pixel was white in each multi-frame exposure. All spatial coordinates are in centimeters.

3.3.2.2 Growth of a snowpack under a gap

Snow deposits were photographed during three different storms as part of the gap experiment. The first storm took place at -0.7 °C and had a maximum accumulation of 36 mm; the second was at -4.1°C with 93 mm of snow, and the third took place at -4.3°C with 15 mm of snow. The deposits

were sectioned and photographed three times during each storm (with the exception of Storm III). The deposits were 2 to 5 times wider than the gap itself (4 cm) and had distinctive Gaussian (bell) shapes (Figure 3.9). To some extent, these characteristics can be explained by the non-vertical fall trajectories (Figure 3.6b and Table 3.2), which had near-zero means, but during which individual trajectories varied from 2.4° to 3.6° off-vertical (Table 3.2, $\sigma_{fall\ direction}$). Over the 62 cm vertical span of the box, these non-vertical trajectories can explain deposits ranging from 9.2 cm to 11.8 cm wide. We note that these values imply a lateral spreading of more than 230% from the gap itself, and the Gaussian shape of the deposits is consistent with the probability distribution function of fall trajectories (Figure 3.6b). Nevertheless, the non-vertical trajectories are not sufficient to explain the full spread of the observed deposits. As Figure 3.9 shows, deposits eventually reached widths of more than 20 cm, fully 9 cm greater than what can be explained by the trajectories alone. From this we conclude that other processes, mainly those detailed in the previous section (bounce, ejection, etc.), were active in moving snow grains laterally. Avalanching of grain packets driven by the angle of repose, as would be expected for sand reaching instability, was never observed.

If we normalize the gap deposit profiles ($h=h/h_{max}$), we find that the deposits during each storm exhibited a distinctive signature (Figure 3.10) that did not change with time or increasing snow height. Storm II (at -4.1°C) produced a wider pattern than Storm I (at -0.7°C), suggesting that there was more lateral spreading of snow at the lower temperature. This is consistent with the work of *Kobayashi* [1987], who found that at lower temperatures bouncing increased and cohesion decreased. It seems contradictory at first, then, that Storm III (at -4.3°C) has the same narrow pattern as Storm I. However, photographs of the snowflakes that fell in the three storms indicate that those falling in Storm III had the most intricate shapes and that interlocking of these flakes may have inhibited lateral displacements despite the lower temperature (Appendix B).
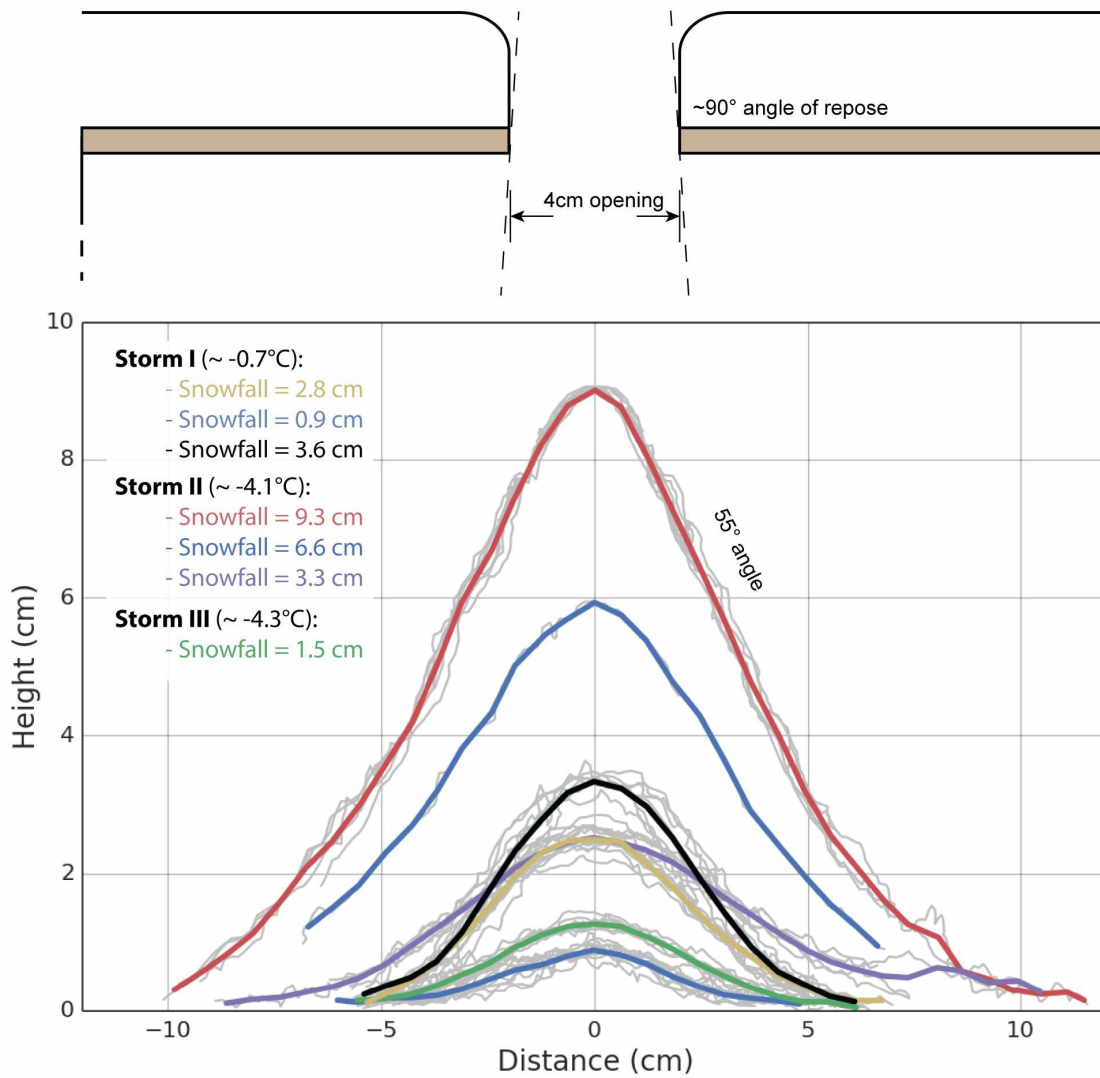
Figure 3.9: Measured cross sections (gray) of snow deposited beneath a 4 cm gap (see Figure 3.3). Roughness at the snow grain scale, as well as some digitization error, can be seen in the individual profiles, but the average profiles (colored lines) remove this random noise.
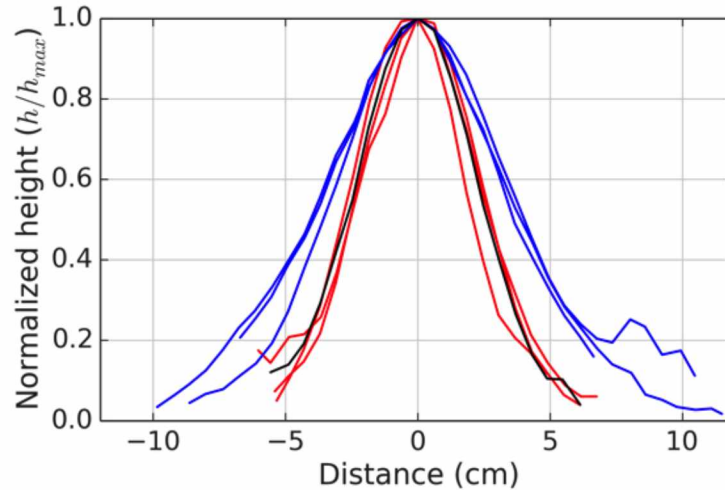
Figure 3.10: Normalized (h/h_{max}) cross sections based on the data in Figure 3.9. Red curves correspond to Storm I (at -0.7°C), blue curves to storm II (at -4.1°C), and the black curve to storm III (at -4.3°C but with intricate snowflakes that could interlock).

While snow was accumulating as a bell-shaped curve at the base of the box, snow also accumulated on the top of the box. The maximum slope of the bell curve was 55° whereas snow at the edge of the gap was nearly 90° (Figure 3.9). This difference indicates that the angle built by snow accumulation is not only a function of the snow characteristics, but also depends on the geometry of the deposition surface, a fact not reported before. In the case of the bell-shaped deposit, the snow supply was artificially limited, but the space for snow to accumulate was unlimited. Whereas at the top of the box, the snow supply was spatially unlimited with a limited space available for accumulation.

3.3.2.3 Snowpack smoothing over artificial bumps

As snow accumulated over the artificial bumps, we tracked three smoothing metrics:

1) change in bump "sharpness" (apex angle),
2) reduction in bump amplitude (Figure 3.5), and
3) increase in bump width (Figure 3.5).

We looked first at single isolated bumps (no interaction with adjacent bumps) (Figure 3.4 bottom), then at groups of interfering bumps (Figure 3.4 top).

Sharpness decreased rapidly at first (Figure 3.11) then more slowly with a fairly distinctive change occurring between 7 and 13 cm of snow, the height of the artificial bumps. The initial rate was significantly higher for the sharply pointed triangles. With increasing snow height (or time), the rate of change in sharpness (the slope of the lines in Figure 3.11) converged for all initial apex angles and sizes. Once the snow height exceeded 20 cm, sharpness continued to decrease but at a low (though measurable) rate that was constant for all bumps.
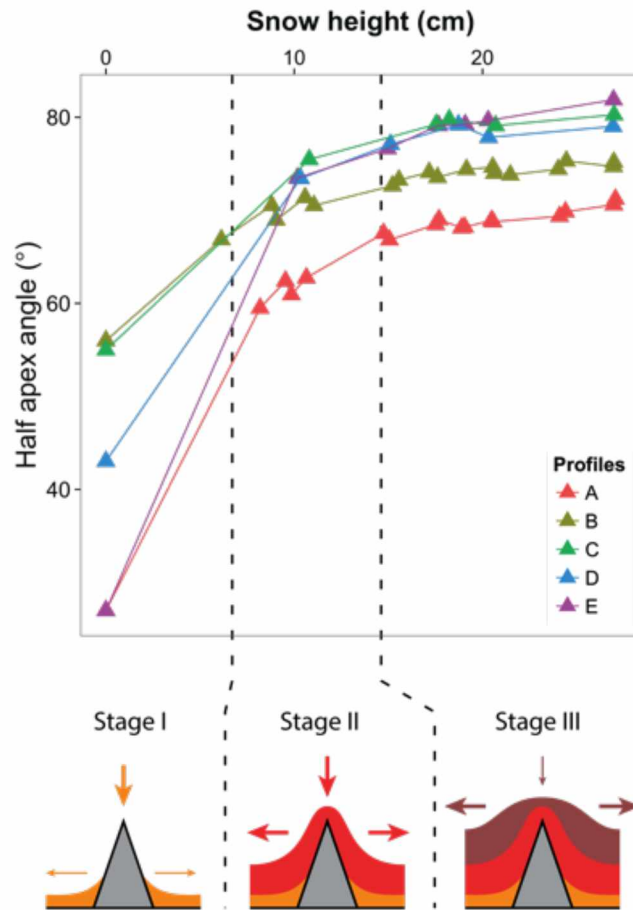
Figure 3.11: Reduction in the "sharpness" of the snow surface over an artificial bump as snow height increased. Five different triangular profiles were used. During the initial stage (Stage I: snow height < 8 cm), the rate of smoothing differed for sharp (A and E) and less sharp (B and C) triangles, and mainly occurred through amplitude reduction. It was followed by stage II in which smoothing rates were lower, and similar, regardless of the initial bump size or sharpness, and during which widening and amplitude reduction had equal weight. In Stage III, smoothing continued, but mainly through increases in width rather than reductions in amplitude. A fully smoothed disturbance would have a half-apex angle of 90°.

A similar pattern of reduction was observed for amplitude (Figure 3.12a). Amplitudes decreased rapidly at first, then more slowly, but unlike the pattern for sharpness, the rate of amplitude reduction did not differ significantly from zero by the end of the experiment. At the same time, the width of the surface disturbances over the artificial bumps increased (Figure 3.12b). The rate of width increase was 2.5 to 3.2 times higher than the rate of amplitude reduction, though we note that we were unable to obtain accurate stratigraphic measurements early in the experiment when the snow was thin, nor for snow heights much greater than 30 cm. By the end of the experiment, snow bump widths were still continuing to increase, albeit slowly, but amplitudes were no longer decreasing. By definition, then, the ratio of the two must have exceeded 3.2 by a considerable amount. As with sharpness, we can recognize two distinct stages in these amplitude and width trajectories (Figures 3.12a and 3.12b).
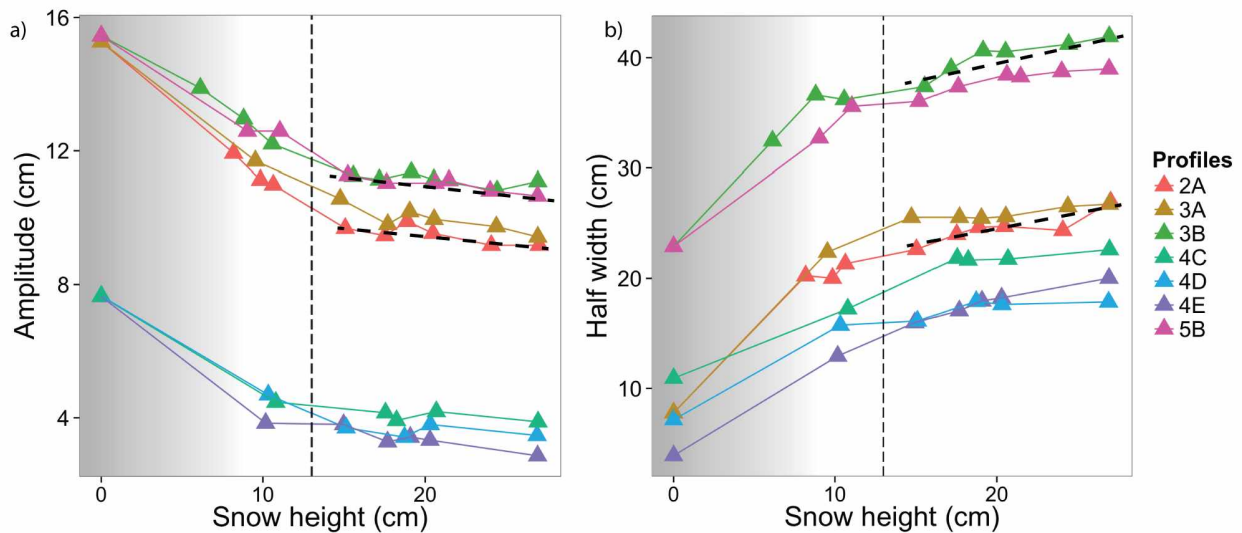
Figure 3.12: a) Reduction in the amplitude of the snow over triangle bumps. The grey shading indicates the snow height range in which the artificial bump was still protruding from the snow. The vertical dashed line separates the rapid initial periods of change (Stage I and II) from a slower, period of change (Stage III), occurring at about 13 cm height. b) Increase in the width of snow over bumps. Grey shading means the same as in Figure 3.12a.

In the natural world, micro-topographic features are rarely separated by large distances. For example in a field of tussocks or on a talus slope, the individual features (tussocks or rocks) are often closer together than they are tall. They are sufficiently close that as soon as the snow is deep enough to cover a feature, it is already constructively interfering with the snow covering adjacent features. With snow bump width increasing at three times the rate of amplitude reduction (Figures 3.12a and 3.12b), this interference is even more likely to occur. We observed this accelerated smoothing effect

(Figure 3.13) in the snow stratigraphy profiles measured over the E1 and E2 series as well as over surfaces I, II, III, and IV (see Figure 3.4 and Table 3.1). Not only did the rate of amplitude reduction increase as artificial bumps were placed closer together, but also the total amount of reduction by the end of the experiment increased as well; 25% greater in the cases of the E1 series. For this series, the acceleration in the rate of amplitude reduction had appeared when the snow was only 7 cm deep. The E1 triangles were 15.6 cm apart (peak-to-peak), but their bases were only 7.8 cm apart, suggesting that the constructive interference occurred before the snow had even reached the height of the triangle tops. For E2 series, which had a base-to-base separation of 17.1 cm, constructive interference had occurred by the time the snow was 12 cm deep.
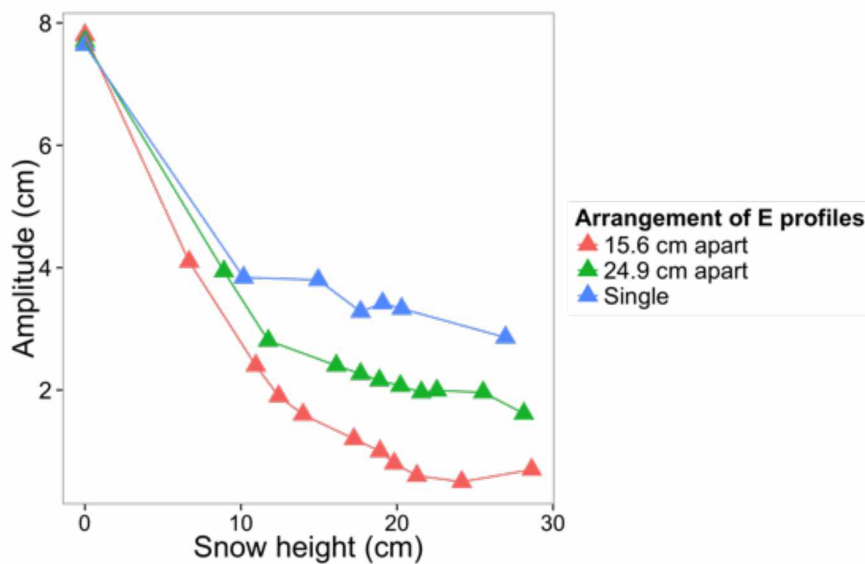
Figure 3.13: Relative decrease in amplitude of the snow surface relief as snow accumulates above (blue) a single E triangle, (green) a series of three E triangles separated by 249 mm peak-to-peak (E2 series), and (red) a series of three E triangles separated by 156 mm peak-to-peak (E1 series).

If the spacing between bumps or features becomes close enough, bridging occurs [*Schmidt and Gluns*, 1991; *Pfister and Schneebeli*, 1999] and accelerates smoothing even more. This effect can be seen in NIR images of surfaces I (spacing 8.9 cm) and II (spacing 3.8 cm) (Figure 3.14a). Over surface I, the snow has draped downward all the way into the cavity between the blocks, but over surface II the cavities are mostly air-filled and the lowest stratum bridges between blocks. The effect of bridging on the smoothing can be seen in Figure 3.14b, where the amplitude of the snow surface is much more rapidly reduced over surface II than surface I, and in fact, the surface expression of the

underlying bumps is gone by the time 14 cm of snow has accumulated. Surface I does not achieve the same reduction until 25 cm of snow has accumulated.
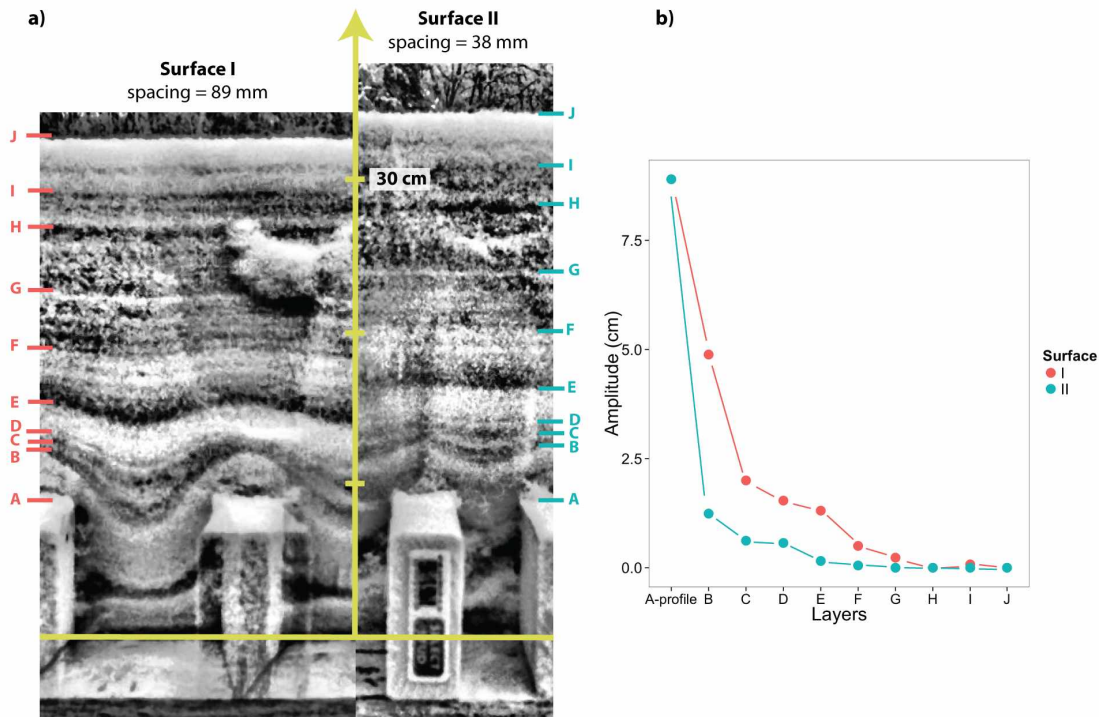
Figure 3.14: a) NIR images of snow strata above surface I (left) and surface II (right). Note how the lowest strata dip down into the cavity between blocks for surface I, but bridge over the gap for surface II. The blocks are standard American lumber (8.9 cm high by 3.8 cm wide). b) Amplitude reduction for the distinct layers marked in Figure 3.14a.

3.4 A Descriptive Model of Snow Smoothing

Assuming a theoretical snowfall during which 1) the flux is spatially uniform, 2) the snowflakes fall vertically, 3) remain where they fall, and 4) no processes such as creep or metamorphism occur after snow has been deposited, then no smoothing of the underlying substrate would occur. This is easily demonstrable with an abacus placed vertically where a first set of beads set at the bottom represent the ground surface profile, and other individual beads represent falling snowflakes brought down one by one: no change of the surface geometry can happen unless we allow beads to move laterally. So what processes move particles laterally, and what processes restrain or inhibit that lateral motion? Table 3.3 summarizes the location and the timescale at which each of these processes occur, as well as their overall effects on smoothing. First, as the strobe-light and gap experiments showed, even without wind, snowflakes follow non-vertical trajectories because they flutter and tumble as they fall

[*Varshney et al.*, 2013]. The trajectories by themselves do not lead to smoothing unless the falling flux is spatially non-uniform (*e.g.* gap experiment), or the surface on which the snow is falling exhibits step-like functions against which the off-vertical trajectories can ricochet and collect unevenly. In the natural world, this effect can be observed when snow falls on a spruce canopy, leading to the formation of a smooth bowl-shaped depression (a tree well) [*Woo and Steer*, 1986; *Sturm*, 1992], a rather sharp-edged hole in the snow.

Table 3.3: Processes Controlling Lateral Redistribution of Snowflakes

Location	Timescale: Short (~seconds)	Timescale: Long (~hours to days)
Atmosphere	Non-vertical snowflake trajectories	Spatial variability of snowfall
Surface	Bounce Ejection Breakage Cohesion Adhesion Interlocking Packing Grain scale roughness Static charges*	
Bulk snowpack		Sintering Metamorphism Creep

Green: processes that enhance lateral displacement of snowflakes. Red: processes that restrain lateral displacement. Black: processes having an uncertain effect. Note: * static charges were shown by *Schmidt et al.* [1999] to play a role in drifting snow, and we suspect they play some role in snow smoothing as well.

Moving down to the snow surface, rapid (≤ 1 s) processes including snowflake bouncing, breakage, and ejection promote lateral displacement, as illustrated in Figure 3.8. Working against these redistribution processes, the forces of cohesion and adhesion, and the interlocking of snowflakes due to their complex geometry, restrain lateral motion of snowflakes. Not explored in our set of experiments, but also likely to be important, is snowflake arrangement (packing), as well as the surface roughness at the grain scale in catching the falling snowflakes [*Löwe et al.*, 2007]. *Schmidt et al.* [1999] showed that static charges affect the force balance of a saltating snowflake. We think these may play a role in the deposition of snowflakes that have fallen through a long air column.

Considering the 10 fast processes (Table 3.3), and the interactions that must occur between them, the balance between enhancement and restraint in lateral transport is clearly complex. It is also controlled by environmental variables that include the air temperature, the shape and size of snowflakes, their fall speed, and the nature of the impact surface (Figure 3.15). For example, merely covering the surface by snow several grains thick changes the surface coefficient of restitution and is sufficient to damp bouncing by a factor of 8 (Figure 3.7), a fact that *Kobayashi* had observed in his 1987 experiments. It is notable that 5 of these processes (breakage; cohesion; adhesion; interlocking; packing) are unique (or amplified) in snow vs. sand.
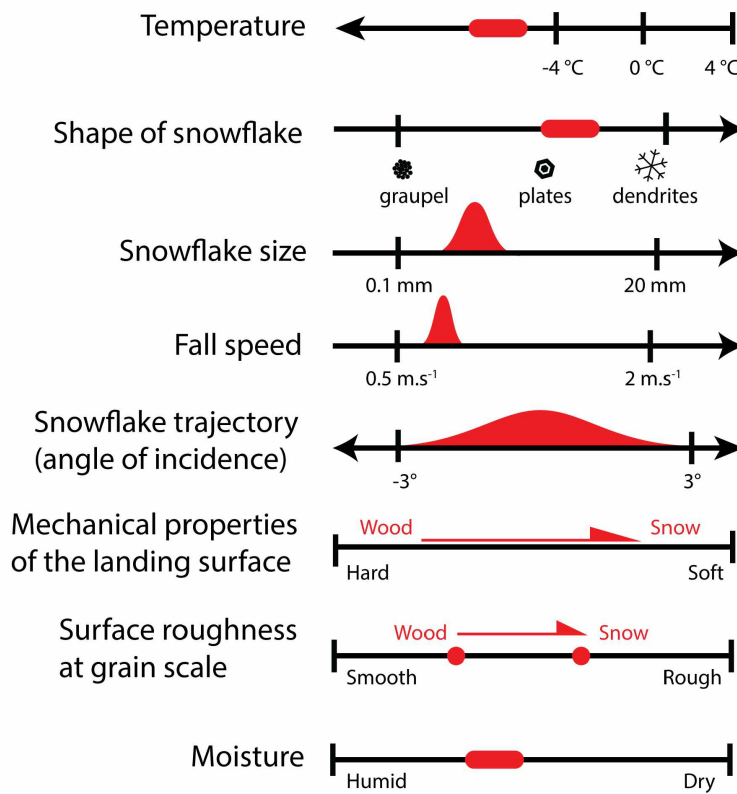
Figure 3.15: Controls on the processes producing lateral displacement of snow grains. The black lines indicate the range of credible variability for each control, and the red arrows indicate how these variables typically evolve during a storm. The example shown here (red shapes) is inspired from our snow bouncing experiment with the snowflakes bouncing on a wood board.

The last set of processes that affect smoothing take place over longer periods of time (hours to days) and affect the whole (bulk) snowpack. These include sintering, creep, and snow metamorphism. While we have no new quantitative data on these slow smoothing effects we have been observing

them for some time (Figure 3.16), and recognize that they too are critical in determining the rate of smoothing and whether bridging will occur or not. In fact, these long period processes are unique to snow. For example, not only (Figure 3.16 right) is the initial angle of repose of snow often higher than sand due to rapid cohesion and interlocking, but (Figure 3.16 left) over time snow can attain angles over 90°, which sand cannot. Both initial and long period processes contribute to bridging, a mechanism that cannot take place in dry sand. Metamorphism, another process unique to snow, might aid smoothing by modifying the shape of snowflakes, and therefore the packing of snowflakes over time. For example a snowpack undergoing kinematic metamorphism (temperature gradient > 0.25 °C cm^{-1}) will see its snowflakes transforming to depth hoar crystals, altering with time its structure.
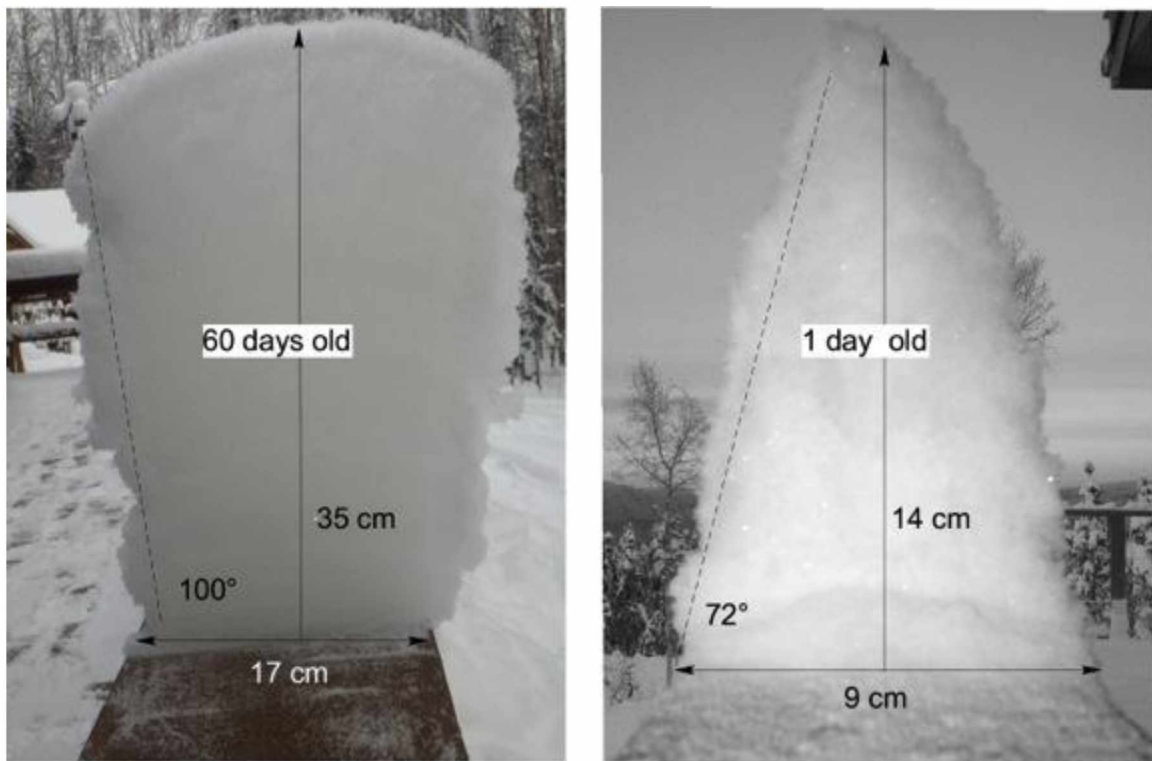
Figure 3.16: Creep and sintering over a period of 8 weeks have created a smoothly rounded snow surface with an angle of repose (AoR) that exceeds 90°, but even over short periods (right) snow that has fallen overnight can achieve an AoR (72°) that exceeds AoRs for dry sand by a significant amount.

As a snowpack forms, all the processes in Table 3.3 occur simultaneously. While some of them, like bouncing or ejection, enhance lateral redistribution of snow, others like cohesive forces inhibit smoothing processes. The fine balance between these processes and their relative efficacy is the key

to explaining observed rates of smoothing, but at present we only have knowledge to describe that balance qualitatively.

3.5 Macroscopic Behavior of Smoothing

At the macroscopic scale, it is the combined effect of the process presented in Table 3.3 that we were able to observe. The relative strength of each process is controlled by a set of environmental variables like temperature, material properties like snowflake size and shape, and the mechanical properties of the landing surface (Figure 3.15). For instance, bouncing, the most effective process for moving snow laterally and therefore in driving smoothing, is highly sensitive to the nature of the substrate. The strobe experiment highlighted that bounces on a wood board were on the order of 4 cm laterally, but only 1/8th as large from a surface covered by 0.1 cm of snow, so we expect a marked reduction in smoothing rates as snow accumulates over a bump.

At first these controls may dominate the smoothing process, but as the snow surface evolves, the geometry of the surface begins to play an increasingly important role. This evolution suggests three stages of smoothing:

- Stage I, when the snow is filling the voids between bumps, but the bumps still protrude and the surface has spatially variable elastic and plastic properties.
- Stage II, when the snow has fully covered an area, creating a homogeneous surface where bumps decrease in amplitude but increase in width, and
- Stage III, when smoothing continues by widening bumps, but amplitude reaches a minimum and ceases to decrease.

Smoothing during Stage I is driven by the heterogeneity of the surface, with the effectiveness of the processes in Table 3.3 varying spatially in a significant way. For example (Figure 3.11) a snowflake impacting exposed metal will bounce 8 times farther than a nearby snowflake impacting snow-covered metal. By Stage II, the surface properties are homogeneous and the surface profile or topography begins to control smoothing. During this stage, what happens to a snowflake striking the surface depends on its incident angle with respect to the local slope. For example, the horizontal distance reached by a bouncing sphere falling vertically and assuming no air drag, will be maximized

for a slope of 22.5° (because the rebound will be at 45°). In a similar way, a falling snowflake is more likely to dislodge a grain at rest when the surface slope is high. In the final stage, when the surface is homogeneous snow and the topography is subdued, then the smoothing processes slow, considerably, and in fact asymptotically approaches zero rates.

We explored the dependence of smoothing on the surface topography using our NIR photo-mosaics (Figures 3.5 and 3.14), computing the slope and curvature of layer interfaces (Figure 3.17). We were most interested in seeing where (along the x-position) layers were thickening or thinning most rapidly (as measured by the ratio of the change in layer thickness, $\Delta h(x)_A$ over the mean layer thickness $\overline{\Delta h_A}$). What we found was that areas of maximum thickening or thinning aligned best not with the slope itself, but with the slope gradient (the curvature). This finding is actually not surprising, for if slope is the driver of lateral transfer, then slope gradient has to be the driver of accumulation and removal.
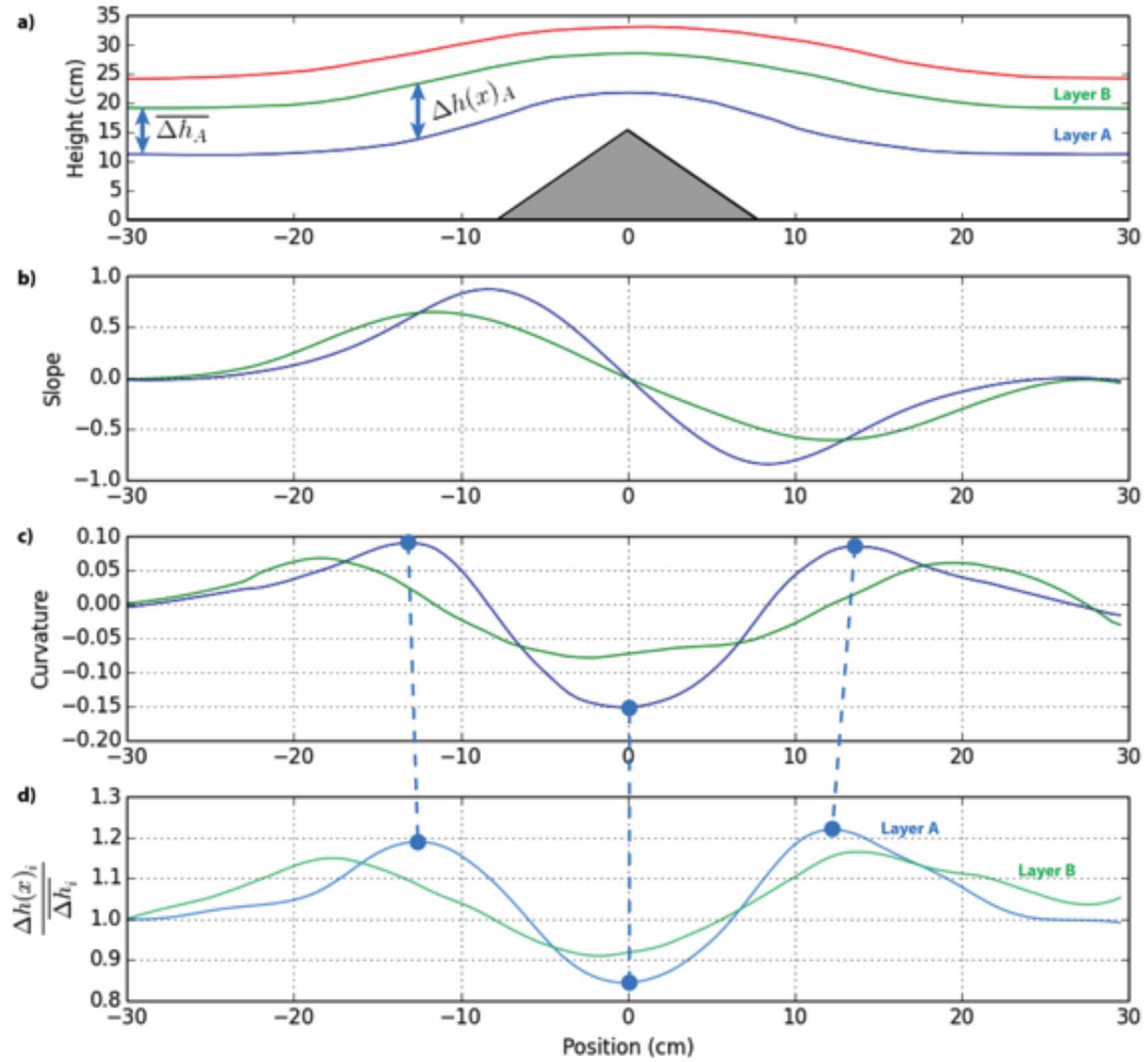
Figure 3.17: a) Snow surfaces digitized from a NIR mosaic, b) surface slopes of layers A and B, c) surface curvature of layers A and B, and d) relative thickness changes of these snow layers in comparison to the mean snow layer thickness (see text).

3.5.1 Surface Growth from a Theoretical Viewpoint

The close correlation between areas of maximum change in layer thickness and the curvature suggests a macroscopic accumulation model for smoothing. If we consider an infinitesimal unit horizontal length (dx) at some position x on an accumulating snow surface at a moment in time (t), we can solve for the change in height dz at that location based on a mass continuity equation:

$$\Delta N = N_{x_{in}} - N_{x_{out}} + N_{z_{fall}} \qquad (3.1)$$

95

with ΔN the change in amount of snow within the vertical column defined by dx. $N_{x_{in}}$ and $N_{x_{out}}$ are defined by the amount of snow moving horizontally in and out of the cell dx in the x-direction. $N_{z_{fall}}$ is the amount of snow falling from the sky directly within the cell dx. Making assumptions that the surface remains continuous through the second order derivative, and that the horizontal flux is proportional to the local slope, we can derive a partial differential equation describing the evolution in time of the snow surface (Appendix B):

$$\frac{\partial z(x,t)}{\partial t}\sigma = -\alpha\nabla^2 z(x,t) + F_z \qquad (3.2)$$

where the term on the left hand side, $\partial z/\partial t$, corresponds to the change in elevation of the surface at (x) over time, ρ is the bulk density of the snow, and F_z is the flux of incoming snow falling from the sky. The first term on the right hand side of this equation corresponds to the redistribution of snow driven by the surface curvature $\nabla^2 z$. Here, α is a coefficient that captures the net effectiveness of all the processes (Table 3.3) that mobilize or restrain lateral transfer. If we set the bulk density to one, then this equation is analogous to the Edward and Wilkinson equation [*Edwards and Wilkinson*, 1982], which describes the surface evolution of a cohesionless granular material like sand.

We implemented a one-dimensional iterative numerical model of equation 3.2 in which we assumed the bulk density to be equal to one, and the incoming flux and the α coefficient to be constant in both time and space. We ran this model for all of our experimental geometries (Figure 3.4). Figure 3.18 shows a simulation run for the E-2 profiles, where the triangular bumps were separated by 24.9 cm peak to peak. While we cannot compare the behavior of our model to observations for Stage I (iterations 1-10), we would expect that during this stage, when the metal bumps were still exposed, α was not constant in x. Snow moving laterally and sliding off the metallic surfaces would have produced larger and wider snow bulges on the sides of the triangles than predicted by our model. However, once Stage II was reached, better agreement between the model predictions and measurements should be observed.
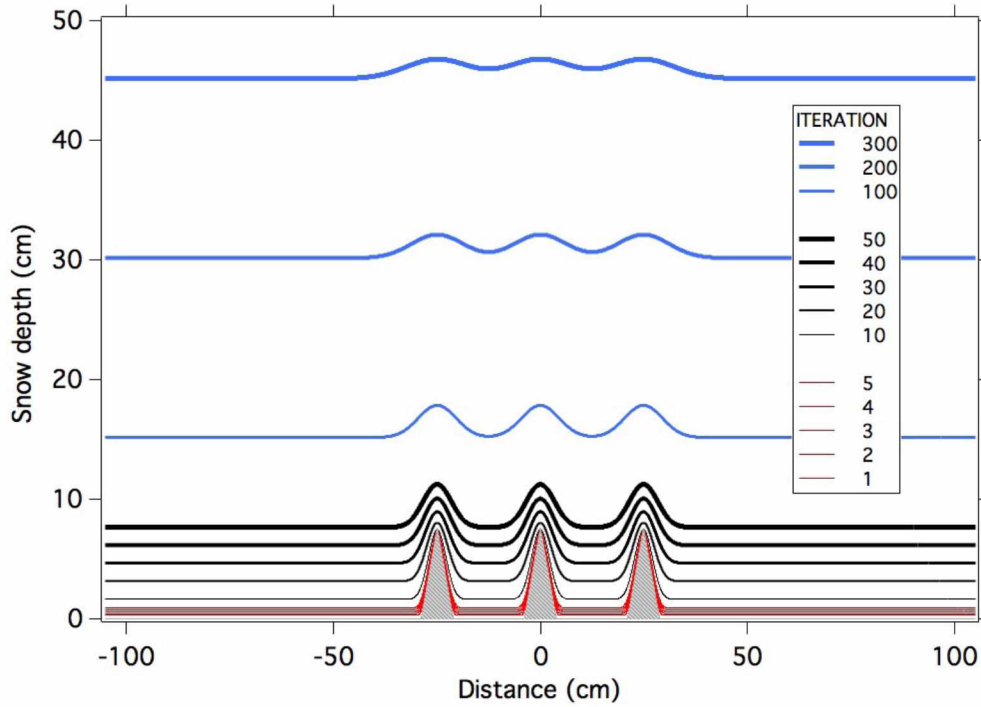
Figure 3.18: Model simulations in one-dimensions of the snow surface evolution based on Equation 3.2 with the following parameter settings: α = 0.08 cm/iteration, or 4.63 X 10^{-8} m s^{-1}, σ = 1 kg m^2, F_z = 0.15 cm iteration^{-1}, which would roughly correspond with F_z=8.68 X 10^{-8} m/s (500 iterations assumed to represent 100 days of winter with steady incremental snowfall). Simulation implemented with Igor Pro software (https://www.wavemetrics.com/).

In fact, for Stage II the simulations closely modeled the behavior of the real snow surface geometry. Figure 3.19 shows the decrease of in snow surface amplitude for the two E-profile simulations, and for a single triangular bump of similar height and width, modeled while keeping the coefficient α constant in both time and space. For the two E-series profiles, the model matches the observations remarkably well. However, for the single bump, the model is unable to attenuate the feature as rapidly as it occurred in reality. We attribute this model behavior to the fact that for the E-profiles in series, the interference between the multiple bumps led to a very rapid passage through Stage I, the stage in which our setting of α is clearly wrong. For the single bump, it took longer (or more iterations) before the model was through Stage I and consequently the offset between model and measured values was larger.
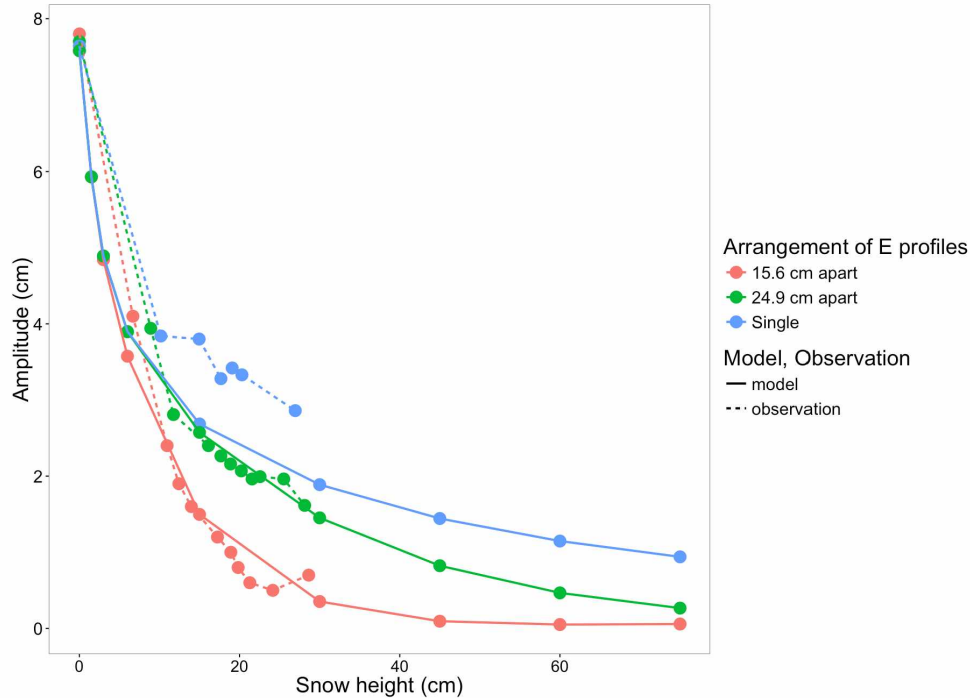
Figure 3.19: Comparison of observations (dashed lines) and modeled (solid lines) amplitudes of the snow surface above three different surface topographies: in blue a single E-profile, in green three E-profiles separated by 15.9 cm, and in red three E-profiles separated by 24.9 cm.

Because the model is macroscopic in scale, all of the processes in Table 3.3 are represented by a single variable, α. While this might be reasonable for a cohesionless material like sand, it is not realistic for snow. Processes like interlocking or metamorphism require variations of α over space when the landing surface may have laterally varying properties (*e.g.* metal or snow), and variations over time during a snowfall as the snowflakes evolve in shape and size, and as snow grains settle and metamorphose. Also, again unique to snow in the natural world, the extreme sensitivity of most smoothing processes to slight variations in temperature [*Kobayashi,* 1987] would require changing α over time and space.

The α-parameter is clearly complex, but we can conceptualize how its value would behave in time (Figure 3.20). During Stage I, it varies mostly in space due to heterogeneity of landing surface properties. Once Stage II is reached, α can be approximated as a constant, as this stage is dominated by bouncing, rather than material properties. Once snowfall stops, creep and metamorphism are the only smoothing processes that remain active at the grain scale. These continue to contribute to

smoothing (though we were unable to measure them in this study) albeit at increasing slower rates, until α must reach a value close to zero. The whole cycle is then reset if there is a new snowfall.
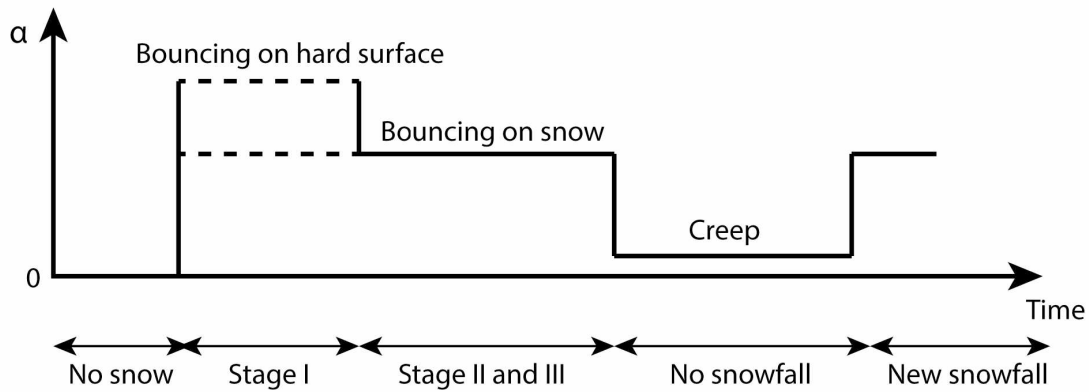
Figure 3.20: Conceptual time evolution of the coefficient α depending on stages and snowfall rate with the dominating grain scale process indicated.

While it is still missing some of the key relationships between grain-scale physics and the macro behavior of the snow surface, our model does provide a useful predictive capability, and strong framework for future investigations. With further experiments like the table experiment, we think it should be possible to find realistic values for α, as well as the functional relationship between α and material properties and environmental variables.

3.6 Conclusion

Investigating the reasons why snow surfaces smooth out an underlying rough landscape, we found that it was the lateral displacement of snowflakes during and following deposition that was the key to the answer. At least 14 grain-scale processes are responsible for the lateral movement of grains. Their combined effect becomes visible and quantifiable at the snow depth scale. Our work and others show that these grain processes are affected by environmental conditions (temperature, snowflake size, shape and fall speed, surface properties) such that slight variations in these conditions can alter the strength of snow lateral transfer. Of these many processes, we found bouncing to be the most effective for moving snow laterally (and therefore smoothing), but also the most affected by changes in surface conditions.

99

Based on observed rates of smoothing, we identified three stages in the smoothing process. The first stage is where surface properties are heterogeneous because the snow surface is not yet spatially continuous. The second Stage II corresponds to when the snow surface is continuous, the amplitude of bumps is rapidly decreasing. Finally in Stage III, the dampening of bump amplitude reaches a limit, while widening continues, but at lower rates.

At the macro-scale, we derived a model of the evolution of a snow surface based on a conservation of mass equation. This model is analogous to the model developed by *Edward and Wilkinson* [1982] for cohesionless materials. However, unlike most E-W equation-based models, for snow we recognize that right now many grain scale processes are being represented by a single lumped parameter (α). This parameter, in reality, is quite complex, varying with both space (stage I) and time (transition stage I to stage II), and true physically based modeling will need to be treated as such.

Our experiments, combined with the modeling results, provide new insights in the smoothing mechanisms responsible for redistributing snow in a landscape. However, quantitative linkage between the two scales (grain and snowpack) at which our experiments took place is still missing, as reflected in our lack of a clear understanding of how to parameterize α. We need a better understanding of the relationship between the 14 processes that contribute to smoothing. The key to understanding the relationship between these process and their respective controls on smoothing will be to run experiments using a similar approach to *Kobayashi's* [1987] bouncing experiment, exploring the influence of temperature on bouncing of ice spheres.

Work on forest canopy interception by *Miller* [1964] and *Schmidt and Gluns* [1991] had already drawn theoretical frameworks, which converged toward a similar set of processes and controls occurring at the grain scale. In this respect, we think our findings might bring a new insight to the problem of predicting forest canopy interception, especially in regards to forest in boreal regions where snow deposition in calm conditions typically occurs over a multi-month period.

Acknowledgements

References

Burnside, J. (2013), A Winter Mind, *London Review of Books* [Online], vol. 35 no. 8, 21-23.

Bader, H., R. Haefeli, E. Bucher, J. Neher, O. Eckel, and C. Thams (1954), Snow and its Metamorphism, *Translation Rep. 14*, USA-SIPRE.

Barabási, A. L., and H. E. Stanley (1995). Fractal concepts in surface growth. *Cambridge university press*. ISBN 0521483085

Bradski, G. (2000), The OpenCV Library *Dr. Dobb's Journal of Software Tools*.

Bunnell, F. L., R. S. McNay, and C. C. Shank (1985). Trees and Snow: The Deposition of Snow on the Ground: a Review and Quantitative Synthesis. *Research, Ministries of Environment and Forests*.

Deegan, R. D., O. Bakajin, T. F. Dupont, G. Huber, S. R. Nagel, and T. A. Witten (1997). Capillary flow as the cause of ring stains from dried liquid drops. *Nature*, 389(6653), 827-829. doi: 10.1038/39827

Dominé, F., S. Morin, E. Brun, M. Lafaysse, and C. M. Carmagnola (2013), Seasonal evolution of snow permeability under equi-temperature and temperature-gradient conditions, *The Cryosphere*, 7, 1915-1929, doi: 10.5194/tc-7-1915-2013.

Edwards, S. F., and D. R. Wilkinson (1982), The Surface Statistics of a Granular Aggregate, *Proceedings of the Royal Society A: Mathematical, Physical and Engineering Sciences*, 381, doi: 10.1098/rspa.1982.0056.

Faraday, M. (1850). On certain conditions of freezing water. *Athenaeum*, *1181*, 640-641.

Festenberg, N., and S. Gumhold (2011), Diffusion-Based Snow Cover Generation, *Computer Graphics Forum*, 30, doi: 10.1111/j.1467-8659.2011.01904.x.

Flin, F., J.-B. Brzoska, B. Lesaffre, C. Coléou, and R. Pieritz (2004), Three-dimensional geometric measurements of snow microstructural evolution under isothermal conditions, *Annals of glaciology*, 38(1), 39–44, doi: 10.3189/172756404781814942.

Gautier, T. (1850), Œuvres de Théophile Gautier, Poésies, *Lemerre*, Volume 2, 206-208.

Kardar, M., G. Parisi, and Y. C. Zhang (1986). Dynamic scaling of growing interfaces. *Physical Review Letters*, *56*(9), 889, doi: 10.1103/PhysRevLett.56.889.

Kobayashi, D. (1987), Snow accumulation on a narrow board, *Cold Regions Science and Technology*, *13*, doi:10.1016/0165-232X(87)90005-X.

Korslund, L., and H. Steen (2006), Small rodent winter survival: snow conditions limit access to food resources, *Journal of Animal Ecology*, *75*, 155-156 doi: 10.1111/j.1365-2656.2005.01031.x.

Kuroiwa, D., Y. Mizuno, and M. Takeuchi (1967). Micromeritical properties of snow. *Physics of Snow and Ice: proceedings= 雪氷の物理学: 論文集*, *1*(2), 751-772.

Locatelli, J. D., and P. V. Hobbs (1974). Fall speeds and masses of solid precipitation particles. *Journal of Geophysical Research*, *79*(15), 2185-2197.

London, J. (1908), To build a fire, *The Century Magazine 76*.

Löwe, H., L. Egli, S. Bartlett, M. Guala, and C. Manes (2007), On the evolution of the snow surface during snowfall, *Geophysical Research Letters*, *34*(21), doi: 10.1029/2007GL031637.

Manes, C., M. Guala, H. Löwe, S. Bartlett, L. Egli, and M. Lehning (2008), Statistical properties of fresh snow roughness, *Water Resources Research*, *44*(11), doi: 10.1029/2007WR006689.

Mellor, M., and A. Mellor (1988) Some characteristics of falling snow. *Cold Regions Science and Technology*, 15(2), 201-206.

Miller, D. H. (1964), Interception processes during snowstorms. Research Paper PSW-RP-18. Berkeley, CA: Pacific Southwest Forest & Range Experiment Station, Forest Service, U. S. Department of Agriculture; 24 p.

Mehta, A., J. Luck, and R. J. Needs (1996) Dynamics of sandpiles: physical mechanisms, coupled stochastic equations, and alternative universality classes. *Physical Review E*, 53(1), 92, doi: 10.1103/PhysRevE.53.92.

Pfister, R., and M. Schneebeli (1999), Snow accumulation on boards of different sizes and shapes, *Hydrological Processes*, 13: 2345–2355, doi:10.1002/(SICI)1099-1085(199910)13:14/15<2345::AID-HYP873>3.0.CO;2-N

Sazaki, G., S. Zepeda, S. Nakatsubo, M. Yokomine, and Y. Furukawa (2012). Quasi-liquid layers on ice crystal surfaces are made up of two different phases. *Proceedings of the National Academy of Sciences*, 109(4), 1052-1055, doi: 10.1073/pnas.1116685109.

Schmidt, R. A., and D. R. Gluns (1991). Snowfall interception on branches of three conifer species. *Canadian Journal of Forest Research*, 21(8), 1262-1269, doi: 10.1139/x91-176

Schmidt, D. S., R. A. Schmidt, and J. D. Dent (1999), Electrostatic Force in Blowing Snow, *Boundary-Layer Meteorology, 93*(1), 29-45, doi: 10.1023/A:1002045818907.

Shapiro, L. (Ed.). (1992). Computer vision and image processing. *Academic Press*.

Stomakhin, A., C. Schroeder, L. Chai, J. Teran, and A. Selle (2013), A material point method for snow simulation, *ACM Transactions on Graphics, 32*, doi: 10.1145/2461912.2461948.

Sturm, M. (1992), Snow distribution and heat flow in the taiga, *Arctic and Alpine Research, 24*(2), 145–152, doi: 10.2307/1551534

Sturm, M., and C. S. Benson. (1997), Vapor transport, grain growth and depth-hoar development in the subarctic snow. *Journal of Glaciology* 43.143: 42-59.

Tape, K. D., N. Rutter, H. P. Marshall, R. Essery, and M. Sturm (2010). Recording microscale variations in snowpack layering using near-infrared photography. *Journal of Glaciology*, 56(195), 75-80, doi: 10.3189/002214310791190938.

Trabant, D., and C. Benson (1972). Field experiments on the development of depth hoar. *Geological Society of America Memoirs, 135*, 309-322.

Van Der Walt, S., J. L. Schönberger, J. Nunez-Iglesias, F. Boulogne, J. D. Warner, N. Yager, E. Gouillart, and T. Yu (2014). scikit-image: image processing in Python. *PeerJ*, 2, e453: e453, doi:10.7717/peerj.453.

Varshney, K., S. Chang, and J. Z. Wang (2013). Unsteady aerodynamic forces and torques on falling parallelograms in coupled tumbling-helical motions. *Physical Review E*, 87(5), 053021, doi: 10.1103/PhysRevE.87.053021.

Vold, M. J. (1963), Computer simulation of floc formation in a colloidal suspension, *Journal of Colloid Science*, 18(7), 684-695.

Wakahama, G., G. Kuroiwa, and K. Goto (1978). Snow accretion on electric wires and its prevention. *Journal of Glaciology, 19, 479-487*.

Woo, M. K., and P. Steer (1986), Monte Carlo simulation of snow depth in a forest. *Water Resources Research*, 22(6), 864-868.

Wood, G. (1940), January, *Cleveland Museum of Art*.

Yunker, P. J., M. A. Lohr, T. Still, A. Borodin, D. J. Durian, and A. G. Yodh (2013) Effects of particle shape on growth dynamics at edges of evaporating drops of colloidal suspensions. *Physical review letters*, 110(3), 035501, doi: 10.1103/PhysRevLett.110.035501

APPENDIX B

Snow Grain Microphotographs and Mathematical Derivation of the Smoothing Model

Introduction

The supporting information presented here comprise

1. A set of microscopic snowflake pictures,
2. Derivation of Equation 3.2 in 1 dimensions

The set of snowflake photographs show the shapes and sizes of snowflakes falling during the three storms (I, II, and III) captured by the closed box experiment (section 3.3.2.3.). Pictures were taken with a Sony Xperia Z3 compact camera (20.7 MP) over the eye-length of a Nikon 20X handheld microscope. Snowflakes deposited naturally on a 2 mm grid.

Equation 3.2, based on the mass conservation equation is a partial differential equation describing the evolution of the snow surface at the macro-scale.

Snow Grain Photographs

The set of microscopic photographs for the three storms (Figure B.1) allow us to get an idea of the types and sizes of snowflakes falling and constituting the accumulation mound observed in the closed-box experiment. We see that Storm I and II had snowflakes of similar sizes (~1 mm), whereas storm III had snowflakes of smaller sizes (<1 mm) with more intricate shapes; bright and white snowflakes are indicative of strong light scattering, occurring due to complex geometry.
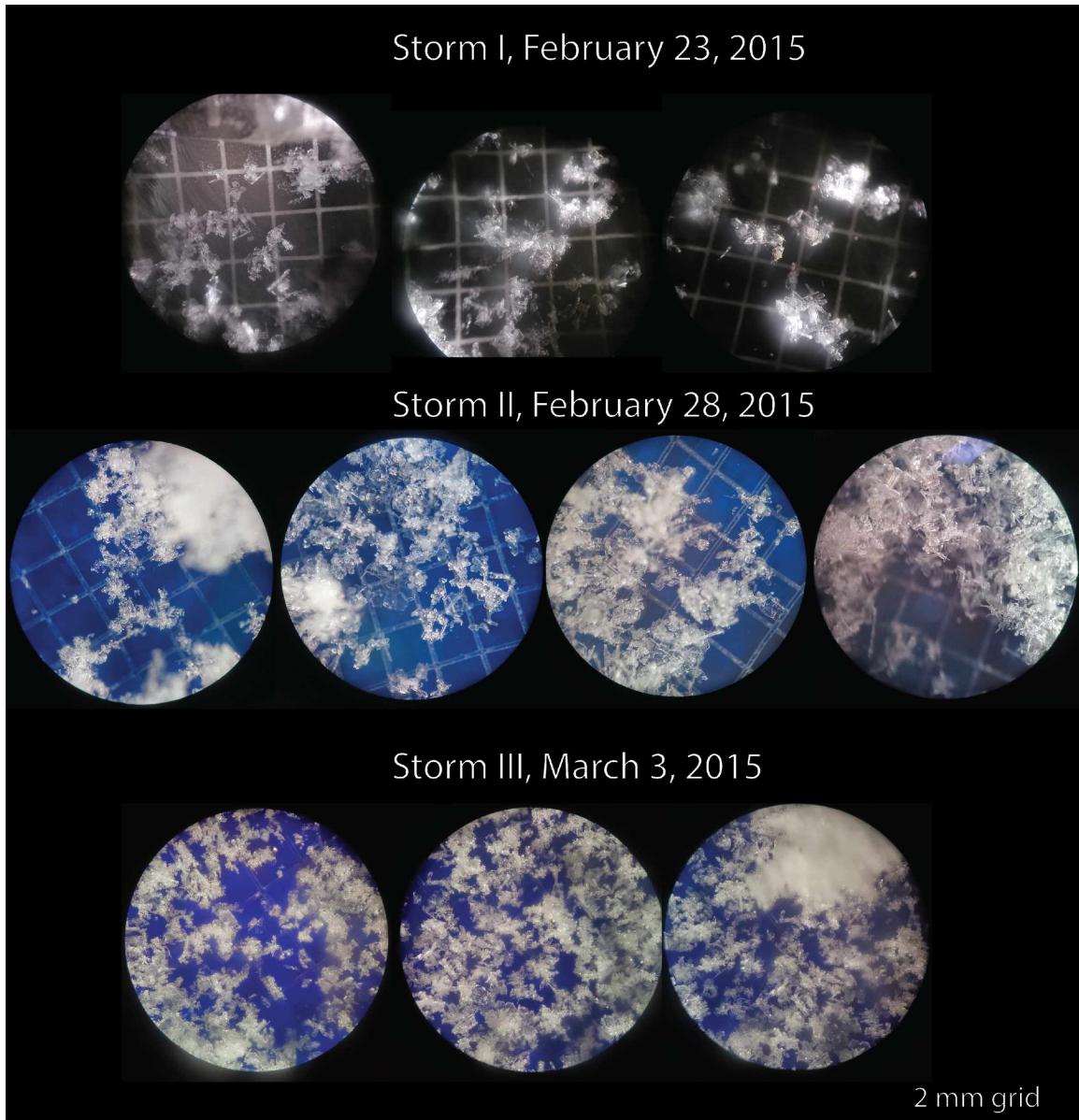
Figure B.1: Photographs of snowflakes for storm I, II, and III of the gap experiment plate through a handheld microscope. Backgrounds are 2mm grids.

Deriving a Mass Balance Model

Based on the conservation of mass equation, we can derive at the macro-scale a model capturing the evolution of a snow surface with time given a constant flux of snow falling from the sky. In a one dimensional space, we define the snow surface by the function $z(x,t)$. For this analysis, the surface $z(x,t)$ must be continuous and derivable to its second order with respect to x.

If we consider a unit horizontal segment defined by dx, we can write the mass balance of snow material, which will accumulate or deplete from the vertical column of footprint dx. Knowing the density of the bulk snow after deposition σ [kg m^{-2}], we can retrieve the change in elevation of the surface $z(x,t)$ by:

$$\Delta z = \frac{\Delta N}{\sigma dx}$$

with the change in height Δz [m] due to a net change in mass of snow of ΔN [kg] in the cell dx [m]. Figure B.2 shows a representation of the problem.
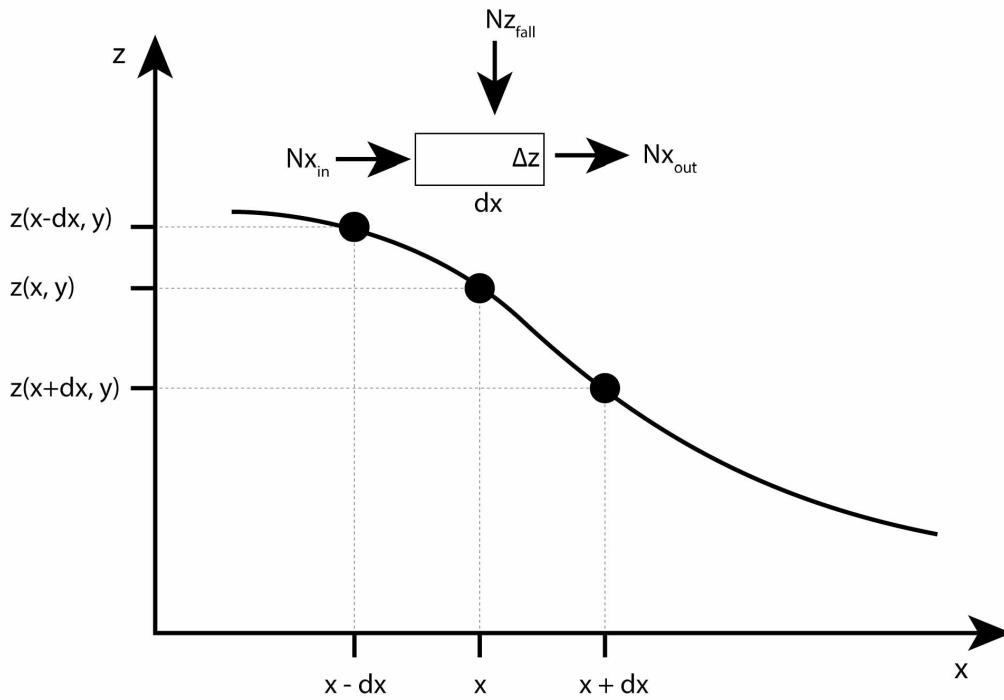
Figure B.2: Representation of the surface $z(x,t)$ and the mass balance in the column defined by dx.

Following the diagram of Figure B.2, we can write the following mass balance equation:

$$\Delta N = N_{x_{in}} - N_{x_{out}} + N_{z_{fall}}$$

with:

1. ΔN the change of the amount of snow in the column defined by dx over the time period dt.

2. $N_{x_{in}}, N_{x_{out}}$ the amount of snow moving laterally in and out of the cell in the x-direction

3. $N_{z_{fall}}$ the amount of snow falling from the sky in the cell.

If now we assume the horizontal fluxes of material being proportional to the local slope then we can write for each horizontal component of the mass balance equation:

$$N_{x_{in}} = \frac{z(x,t) - z(x-dx,t)}{dx} \alpha dt$$

$$N_{x_{out}} = \frac{z(x+dx,t) - z(x,t)}{dx} \alpha dt$$

where α is the coefficient of proportionality between the amount of snow moved laterally and the local slope. The unit of α is [kg s^{-1}].

Lastly, the vertical amount of snow falling in the cell dx can be defined by $N_{z_{fall}} = F_z dx \Delta t$ with F_z the vertical flux of snow in [kg s^{-1} m^{-1}]. Substituting all the individual terms into the mass continuity equation we obtain:

$$\Delta N = \frac{z(x,t) - z(x-dx,t)}{dx} \alpha dt - \frac{z(x+dx,t) - z(x,t)}{dx} \alpha dt + F_z dx \Delta t$$

This can be simplified to:

$$\frac{\partial z(x,t)}{\partial t} \sigma = -\alpha \nabla^2 z(x,t) + F_z$$

CHAPTER 4: Snow Accumulation in a Boreal Forest of Interior Alaska Recorded With a Terrestrial Lidar[1]

Abstract

The taiga (boreal forest), which is covered by snow for 6 to 8 months of the year, extends over 16 million km^2, making it the largest biome on Earth. While the snow has a strong impact on the development of taiga plants, these plants in turn affect the local distribution of the snow. In this study, using a terrestrial lidar, we followed the evolution of snow accumulation in the taiga during three winters (2010-2013) at a 2000 m^2 site near Fairbanks, Alaska. Based on lidar 3D models, we were able to identify and quantify the impact of various canopy types on the nature and shape of the snowpack surfaces. From these measurements, we identified five types of canopies based on their effects on the snow distribution: spruce trees, young spruce ($\leq$ snow depth), stiff shrubs, supple shrubs, and tussocks. Snowpits revealed the long-lasting presence of air cavities at the bottom of the snowpack, in large measure due to prostrate plants and small shrubs at the base of the snow. Over the three study years, the snow distribution patterns at the end of winter were similar despite the complexity of the landscape geometry and differences in the amount and seasonal pattern of snowfall.

4.1 Introduction

Interactions between snow and vegetation have been studied from two main perspectives: an ecological point of view designed to understand the impact of snow on plant communities in order to better predict the evolution and distribution of plants or ecotypes with time; and a hydrological point of view designed to clarify the impact of trees (mostly evergreens) on the hydrographs of catchment basins, especially in mid- and northern latitudes.

In our changing climate, the Arctic and sub-Arctic biomes are expected to go through major shifts [*Chapin et al.,* 2004]. Based on satellite imagery, these shifts are already underway. Tundra has been

---

[1] Filhol, S. Snow Accumulation in a Boreal Forest of Interior Alaska Recorded With a Terrestrial Lidar, Prepared for submission to the journal Hydrological Processes.

observed to be greening, while in contrast, the boreal forest has been browning, moving to a lower photosynthetic activity state [*Epstein et al.*, 2013]. Because of the close linkage between snow cover and the tundra and taiga ecosystems, the long-term linked evolution of the snowpack and the plants needs to be understood [*Liston and Hiemstra*, 2011]. In this respect, the expansion of tundra shrubs has drawn a lot of attention [*Sturm et al.*, 2001; *Myers-Smith et al.*, 2015]. Modeling efforts have been incorporating different shrub ecotypes and examining how the whole system might respond [*Kaplan et al.* 2003; *Bonfils et al.*, 2011]. These models react to climatic and snow variables, but they incorporate only crude assumptions for snow-shrub interactions. Other ecological studies have shown how a change in snow condition might favor certain species at the expense of others. For instance, the expansion of the Siberian dwarf pine (*Pinus pumila*) throughout eastern Siberia identified by *Lozhkin and Anderson* [2013] from pollen records in lacustrine cores, is thought to be linked to an increase in winter precipitation since ~8300 yr BP. *Okitsu and Ito* [1984] observed that this species is particularly well suited to handle deeper snow than other species of the local plant community.

Because snow is not only important to ecosystem evolution, but also to humans in the form of fresh water supply, many groups have studied the impact of forested lands on the total accumulation of snow and spring run-off [*Davis et al.*, 1997; *Ellis et al.*, 2010; *Lundquist et al.*, 2013]. Trees have been found to intercept snow, facilitating the sublimation of snow, decreasing wind transport events as the tree density increases, and shading the sub-canopy snowpack from direct sunbeams in springtime, resulting in later melt. As a result, we now know that a forest canopy decreases the overall snow water equivalent, and delays the onset of the melt period [*Varhola et al.*, 2010; *Miller*, 1964; *Bunnell et al.*, 1985]. But a recent inter-comparison of Snow Water Equivalent (SWE) dynamic models for forests [*Rutter et al.*, 2009] showed great differences in model output, in large measure because of the abstraction of forest canopy processes into two simplifying metrics, the leaf area index and the canopy closure. *Moeser et al.* [2015] showed that improving the canopy representation in the *Hedstrom and Pomeroy* [1998] model by incorporating 3D canopy metrics improved the forecast of snow accumulation by 25%. Clearly, there is room for better data and better understanding of how snow and the boreal forest interact.

The boreal forest is of particular interest when it comes to snow and vegetation interactions because snow accumulates there over 6-7 months of the year, and because it is the largest forest in the world, covering up to 11% of the continents. This forest is known to have a well-defined life cycle of about

100-150 years, paced by forest fire frequency [*Yarie*, 1981; *Fastie et al.*, 2002]. Right after a burn, shrubs recolonize the land, followed by deciduous trees (*Betula sp.*, or *Populous sp.*). The forest reaches maturity when evergreen trees (*Picea sp.*) have returned and overtaken deciduous trees. These stages produce distinct ecotypes that are distributed in a patchwork pattern in flat regions, based on historical fire succession, and soil conditions (presence of permafrost and moisture content). In regions with relief, the ecotypes tend to be segregated based on slope, aspect, and elevation. Low south facing slopes are populated with deciduous trees, while north-facing slopes are populated with evergreen species such as black spruce (*Picea mariana*). For each stage of tree succession there exists an understory plant community varying based on tree spacing and soil conditions.

The *U.S. Geological Survey NLCD* [2001] land classification for Alaska shows that 69% of the Alaskan forest is evergreen, from which about 44% is dominated by black spruce [*Van Cleve et al.*, 1986]. Based on *Viereck et al.* [1992], typical plant communities associated with black spruce (*Picea mariana*) are:

1. moss (*Sphagnum sp.*)/Labrador tea (*Ledum sp.*)
2. tussock sedges (*Carex sp.*)/dwarf shrubs such as birches (*Betula glandulosa /nana*), willows (*Salix sp.*), Labrador tea and blueberry (*Vaccinium alaskaense*).

These lower plant communities form a sub-canopy affecting the deposition of snow. The impacts of shrub vs. tree canopies on snow distribution have been studied [*Varhola et al.*, 2010; *Ménard et al.*, 2014], but always separately. However, in the case of the boreal forest, if one wants to understand the impact of snow distribution on plants, or the impact of plants on snow accumulation processes, it is necessary to adopt a comprehensive view of the processes occurring in the forest, and study both sets of interactions together.

That is what we do here. In this paper, we present data acquired over three years of snow measurements at a boreal forest plot using a terrestrial laser scanner, time-lapse photography, and manually dug snowpits. With the lidar we were able to visualize the various responses of plants to snow loading over time, and in a number of snowfall events. We were able to measure precisely the geometry of the snow surface over a 2000 m^2 area for three winters. To structure our results, we will split our descriptions into three canopy types: the trees, the shrubs of the understory, and the

smaller vascular plants populating the bottom part of the snowpack, called here the subnivean plants.

4.2 Methods

4.2.1 Site Description

Our study site is located in the vicinity of the U.S. Army permafrost tunnel in Fox, Alaska, in a lowland black spruce forest. Indicated locally by the presence of hummocks, permafrost underlies the entire site. It is part of the watershed of Glenn Creek, which was used from 1964-1967 for one of the first hydrological studies of a boreal water basin influenced by permafrost [*Dingman*, 1971]. The area of our study was a circular plot of about 50 m in diameter facing northwest, with an average slope of 4°.

The largest plants at that site are black spruce (*Picea mariana*), birch trees (*Betula papyfera*), and larches (*Larix laricina*). Trees are surrounded by a thick mat of shrubs consisting of dwarf birches (*Betula glandulosa/nana*), willows (*Salix sp.*), labrador tea (*Ledum sp.*), blueberry (*Vaccinium alaskaense*), and low-bush cranberry (*Vaccinium vitis-idaea*). The soil is covered by either *sphagnum sp.* or by sedges (*Carex sp.*) in the form of tussocks. These plants account for most of the predominant species interacting with the snow, though vascular plants and bryophyte species not specifically mentioned here are either present in small (anecdotal) amounts, or for some species (*e.g.* grasses, lichens) do not interact with snow and only develop canopy foliage in the summer time. For this study we ignored birch trees, as they were located on the outer edge of our study area and not within the reach of the lidar.

Figure 4.1 shows the site based on terrestrial laser scanner data acquired in September 2012, before the first snowfall and after plants had shed their leaves. Trees were sparsely distributed, on average 5.6±3.4 m apart (Figure 4.2). Spruce trees reached 8.1 m tall at most, with crown diameters of 1.04 m on average. Larch trees were present but were small, reaching only 3.1 m tall. Shrubs, as we will investigate in more detail in section 4.3.3, formed a thick mat of intricate branches below the tree canopies and in the clearings. In September, the average mat thickness was 0.37 m.
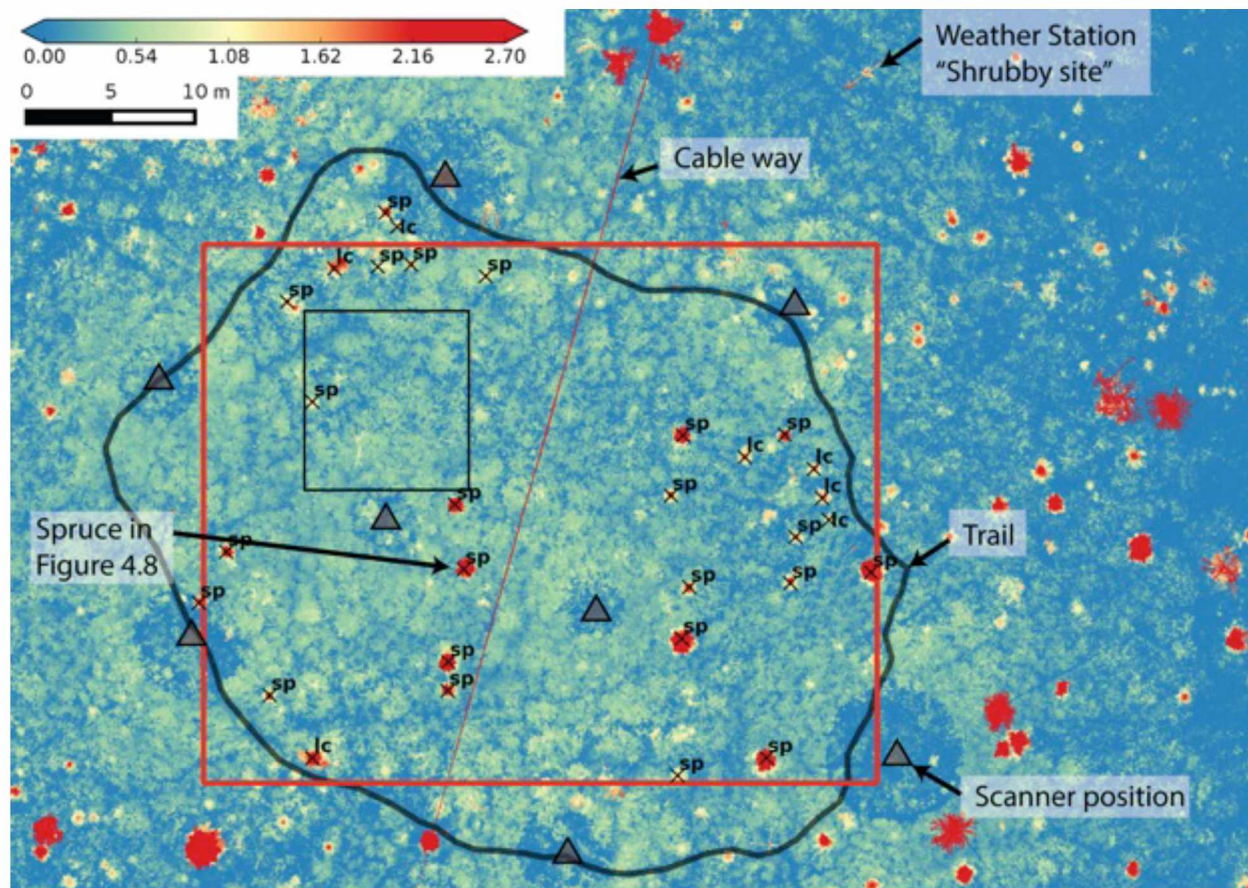
Figure 4.1: Canopy height map of the study site based on lidar data from September 2012 (snow free). Because pixels represent an area of 2*2 cm, blue colored pixels either indicate no canopy or the lack of data. Values of the color-scale are in meters. The red rectangle indicates the boundary of the area used for analyzing the lidar data. The black line corresponds to the trail contouring around the site. The gray triangles are the locations where the lidar scanner was set up. In winter, the lidar was only positioned along the trail. The black rectangle shows the zoomed area in Figure 4.12. Black crosses indicate trees with the species coded by: sp-spruce, lc-larch.
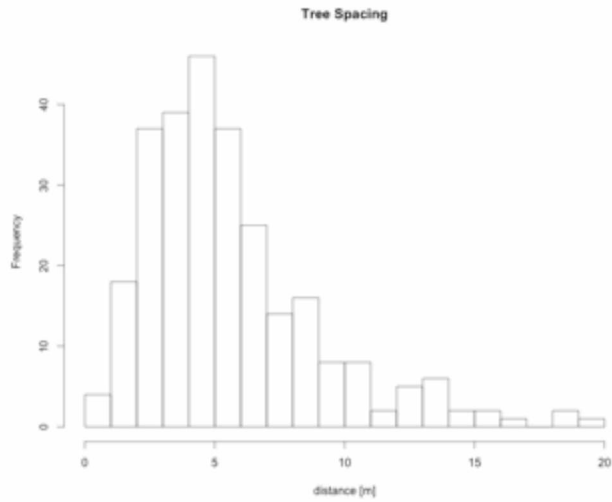
Figure 4.2: Histogram of distances separating trees including black spruce, larch and birch (mean= 5.6 ± 3.4m, median=4.8m).

The plant community composition of the understory between trees was measured every 30 cm along four randomly oriented transects. Figure 4.3 presents the frequency of each species and the occurrences at which two species were found together. There is a clear dominance of the understory plant community by *sphagnum* mosses, followed by low-bush cranberry (*Vaccinium vitis-idaea*), and then labrador tea (*Ledum sp.*). These latter two were often found together. A second group composed of dwarf birch (*Betula nana/glandulosa*), blueberry (*Vaccinium alaskaense*), and sedges (*Carex sp.*) was also frequently found together.
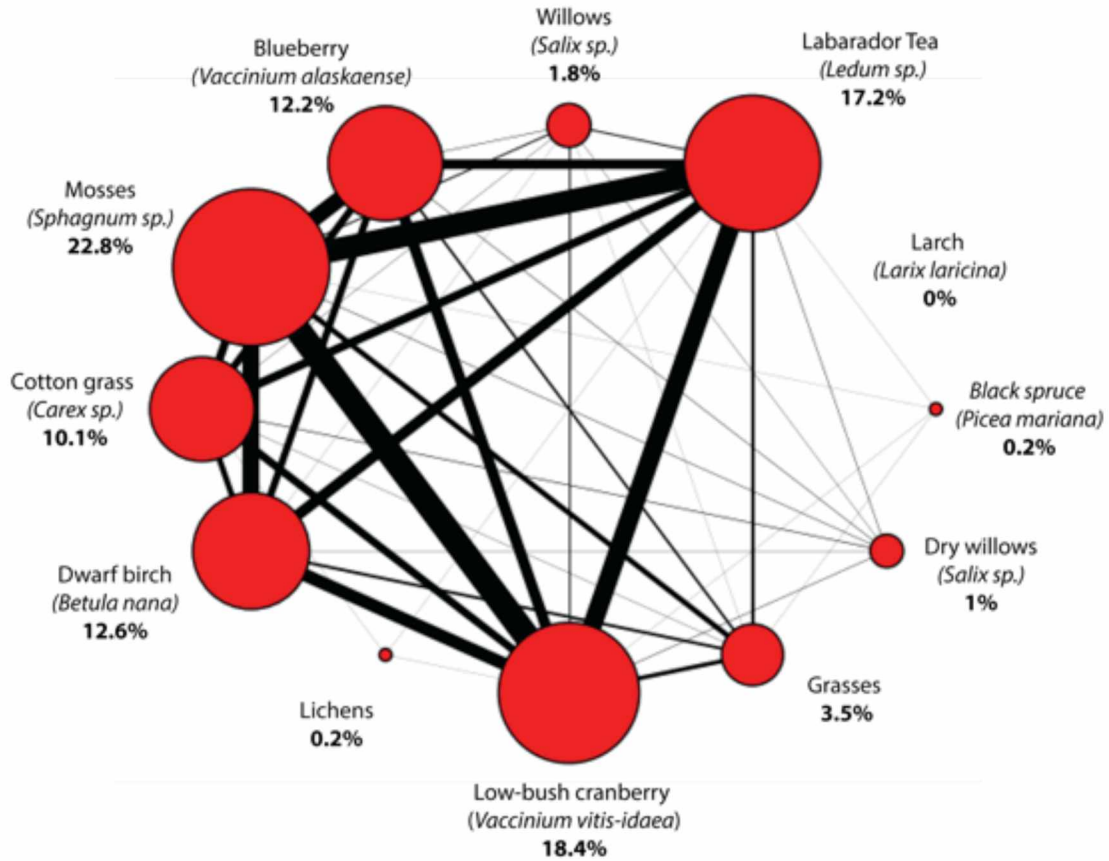
Figure 4.3: Plant community composition and frequency. The size of the red nodes indicates the frequency of occurrence of a given species, and the width of the lines connecting the nodes is proportional to the frequency at which two connected species were found together. Data were collected every 30 cm along four randomly oriented transects for a total length of 104 m.

4.2.2 Instrumentation

The site was equipped with multiple instruments to follow the evolution of the snowpack throughout the winter (Figure 4.4). There was a time-lapse camera recording the overall conditions of the site during the first year, as well as two autonomous weather stations measuring snow depth with a sonic ranger, air temperature with a 107 Campbell temperature probe, and wind speed and direction with a Young 5103 anemometer. One weather station was located within 50 m from the site in an open part of the forest, surrounded by shrubs (visible on Figure 4.1). The second weather station was located 600 m from the site, in a denser birch and spruce mixed forest.
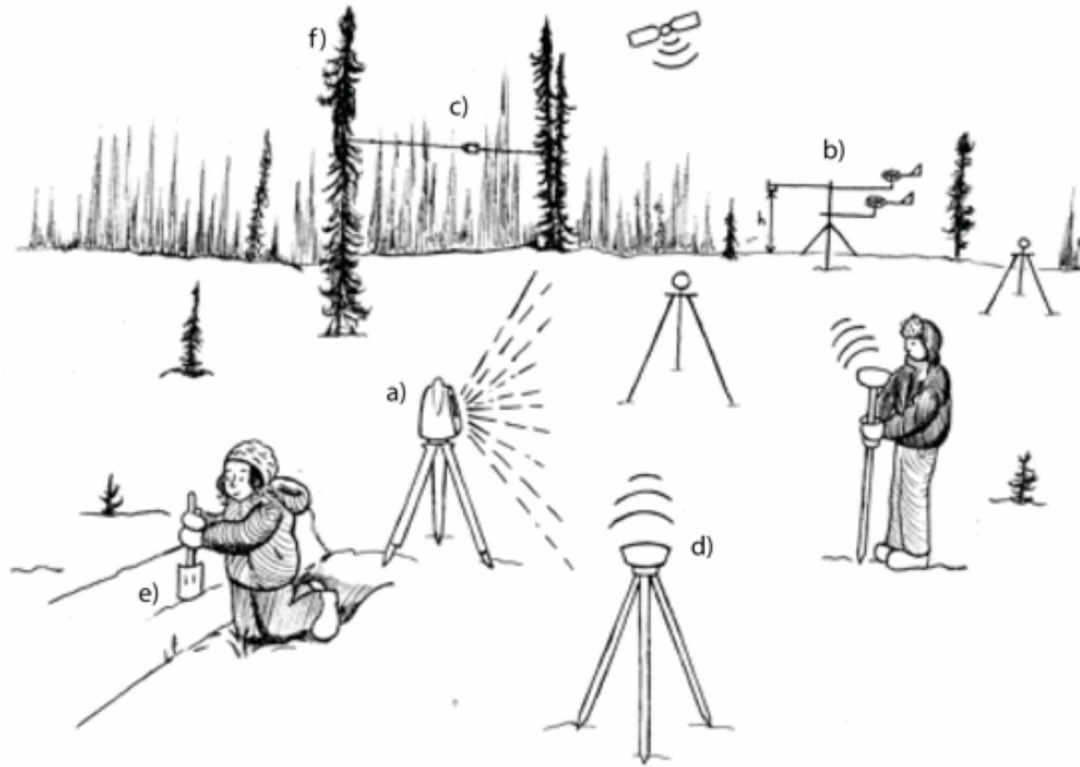
Figure 4.4: Instrumentation and field techniques deployed at the study site: a) terrestrial laser scanner, b) weather station, c) cable camera, d) differential GPS plant/snow survey, e) snowpits, f) time-lapse photography. Illustration by Sarah DeGennaro.

In addition to the autonomous instrumentation, we visited the site regularly to record the evolution of the snowpack using visual snowpit stratigraphy, photography from a cableway, and to make snow depth measurements. At the core of this experiment, a terrestrial laser scanner unit (lidar) was used to map the snow and vegetation surfaces. The first lidar run was done on March 2011, just before melt. For the following two winter seasons (winter 2011-2012 and 2012-2013), we scanned the site multiple times particularly after significant snowfalls, as long as the temperature would allow running the lidar unit (>-20 °C) for the extended time required to scan the entire site (~6 hrs.).

In the snowpits we measured the size and extent of the recurring presence of air cavities below the snowpack. Using basic tools (ruler, microscope, gridded card), we recorded snow layer thicknesses, snow crystal types, and approximate crystal size. When possible, we measured the layer density and identified the bottom flora.

4.2.3 Lidar Data Processing Method

The terrestrial lidar was a Leica C10 Scanstation, equipped with a green laser (532 nm) scanning its entire surroundings. Each time we set the scanner on a tripod, scanned, then moved the lidar to one of six different viewpoints around the site (Figure 4.1). This minimized lidar shadows. The six acquired scans were then merged with the Leica commercial software Cyclone using a set of six targets. This process aligned the scans with an error of less than or equal to 10 mm. For comparing scans acquired at different dates, several target positions were measured with a Differential GPS to obtain their coordinates in the Universal Transversal Mercator system using the WGS 84 datum. Table 4.1 summarizes the dates and seasons of each lidar run performed at the site.

Table 4.1: Dates of Lidar Scans

Season	Scan date	Number of positions	Snow depth (cm)
Spring 2011	March 11	6	59.8
	April 30	6	-
Winter 2011-2012	September 29	8	-
	October 23	6	~2
	November 11	3	13.3
	November 12	3	11.5
	December 12	6	18
	January 11	6	35.5
	February 15	6	39.5
	March 8	6	66.7
	March 26	6	54
Winter 2012-2013	October 21	6	4.1
	January 7	6	26.5
	February 13	6	45.5
	March 8	6	59
	April 5	6	65.9

A lidar provides data in the form of a point cloud, where each point represents the location of the laser reflection calculated based on the speed of light in the air and the laser orientation. Point clouds merged with Cyclone were then opened and processed systematically with scripts written in the programming language Python, using the open-source libraries Pandas (http://pandas.pydata.org/), Laspy (http://pythonhosted.org/laspy/), and GDAL (http://www.gdal.org/) to extract raster files and point cloud slices. These allowed us to visualize

the time evolution of the snowpack with respect to the plant communities. The scripts are accessible at the URL https://github.com/ArcticSnow/dempy.

4.3 Results

4.3.1 Weather History

Both plants and snow respond to weather. Temperature directly affects plant mechanical strength [personal communication with Dr. Syndonia Bret-Harte, *Bret-Harte et al.*, 2001], and is a key environmental variable for snow metamorphism, as well as snow deposition processes [*Filhol and Sturm*, in Prep]. Wind in the boreal forest often sheds snow off trees through induced vibrations, rather than transporting snow as described in *Filhol and Sturm* [2015].

Figure 4.5 presents the weather for the winter of 2011-2012 for both weather stations. Despite eight melt events there was a continuous record of snow on the ground. Because the spruce forest station had a cleared space below the sonic ranger, the beginning and the end of the snow depth signal is clean. In contrast, because the closer, shrubbier station was placed on top of a permafrost hummock and surrounded by complex shrub structures 1) at the beginning and the end of the season (when the snowpack was thin) the signal is noisy, and 2) the station mast must have slowly moved throughout the season as zero snow in the fall registered zero, but the reading was negative in the spring after the snow had melted. But more important than the absolute value of snow depth, this station showed the relative evolution of the snowpack as the shrubs became covered with snow. In November and December we see that the variability of the snow depth signal decreased as the snow accumulated in the shrub canopy, indicating both smoothing and settling of the underlying canopy. . At the forested met site, the snow depth reached a maximum of 69.7 cm on March 7th following a 23 cm snowfall.

Combining time-lapse video and wind records, we were able to observe the dynamic of tree loading by snowfall. For this, we used a qualitative scale of four levels to denote the degree of loading, ranging from no snow to a canopy fully loaded. This scale shows that there were long periods of up to 24 days during which the trees stayed fully loaded (Figure 4.5c). Winds rising above 5 m s^{-1} were sufficient to shed these snow loads, and these wind events were often associated to episodes of

warm temperature, like on February 4th and 7th where temperatures were above freezing and wind peaks were around 6 m s⁻¹. In such cases, the wind mechanically shed snow off the canopy, and above-freezing temperatures significantly decreased the adhesion forces between snow and the canopy foliage (*e.g.* needles), aiding the shedding.
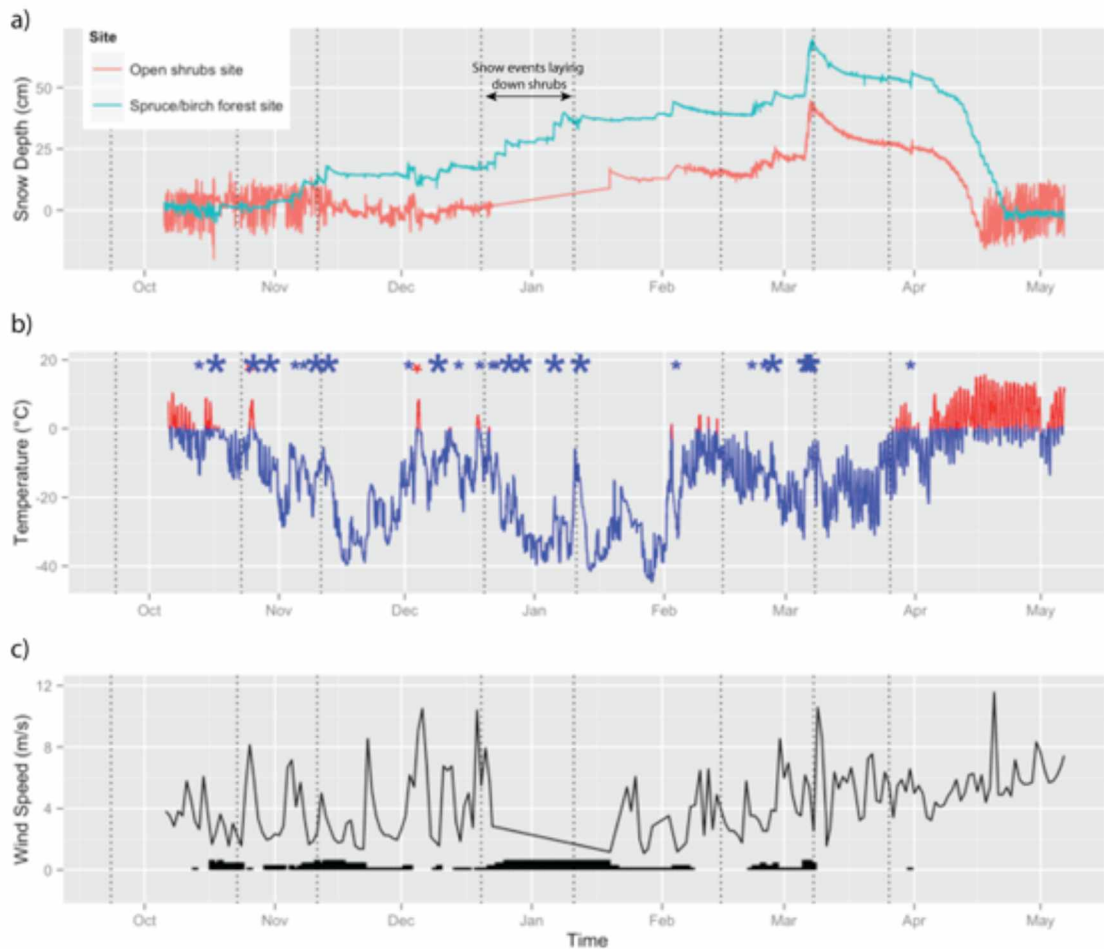
Figure 4.5: Snow depth (a), temperature (b) and wind speed (c) at Glenn Creek at the forest and shrub sites 2011-2012. Stars in graph b) indicate snowfall events with star size indicating light and heavy snow. Graph c) shows the loading of the spruce canopy (four qualitative levels) based on the time-lapse video; the taller the bar, the more the tree canopy is loaded. The dotted lines represent the dates at which we scanned the site with the lidar. Winds in excess of 6 m s⁻¹ appear to have triggered canopy unloading.

For the second winter season, 2012-2013 the shrub station did not run, so we only have partial weather records from the station located farther away in the dense forest. As seen in Figure 4.5, snowfall events and temperature signals were similar at both sites, but wind at the forested site was greatly reduced by the surrounding trees. In this respect, it is not representative of the wind

119

occurring at the research site, so Figure 4.6 excludes any wind record. During the second season (Figure 4.6) there were only two melt events, and fewer but larger snowfall events. On December 13, 29.3 cm of snow fell, settling to 25 cm two weeks later.
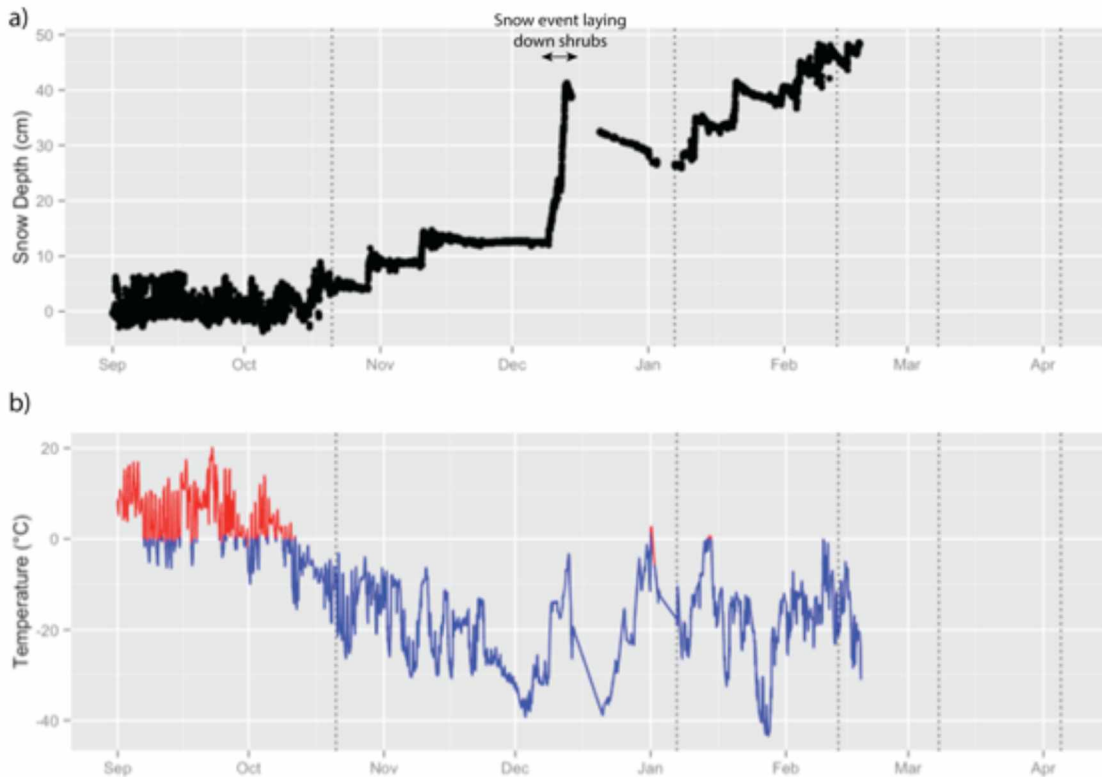
Figure 4.6: Snow depth (a) and temperature (b) at the Glenn Creek forest weather station for the winter season 2012-2013. The dotted lines represent the date at which we scanned the site with the lidar. No data from shrub site are available for this winter.

4.3.2 Trees

The largest elements in the landscape were trees. Mostly black spruce, they ranged from less than a meter to over 5 meters tall (Figure 4.2). The second tree species was larch, which was typically less than 3 m high.

In Figure 4.7 the snow surface around a small spruce (<1 m) is shown for all three winters. During the first winter, the spruce was small enough to be pushed down by snow and was not visible above the snow surface after March. In the following winter, the same spruce protruded through the snowpack throughout the entire winter, and for the last winter of record the spruce also maintained its tip above snow. Two reasons, possibly complementary, explain these inter-annual differences.

120

First, the winter of 2010-2011 had a snow surface 10 cm higher than the following two winters. Second, the spruce had grown (~25 cm in three years) to a critical size beyond which the local snow load was unable to push it down.
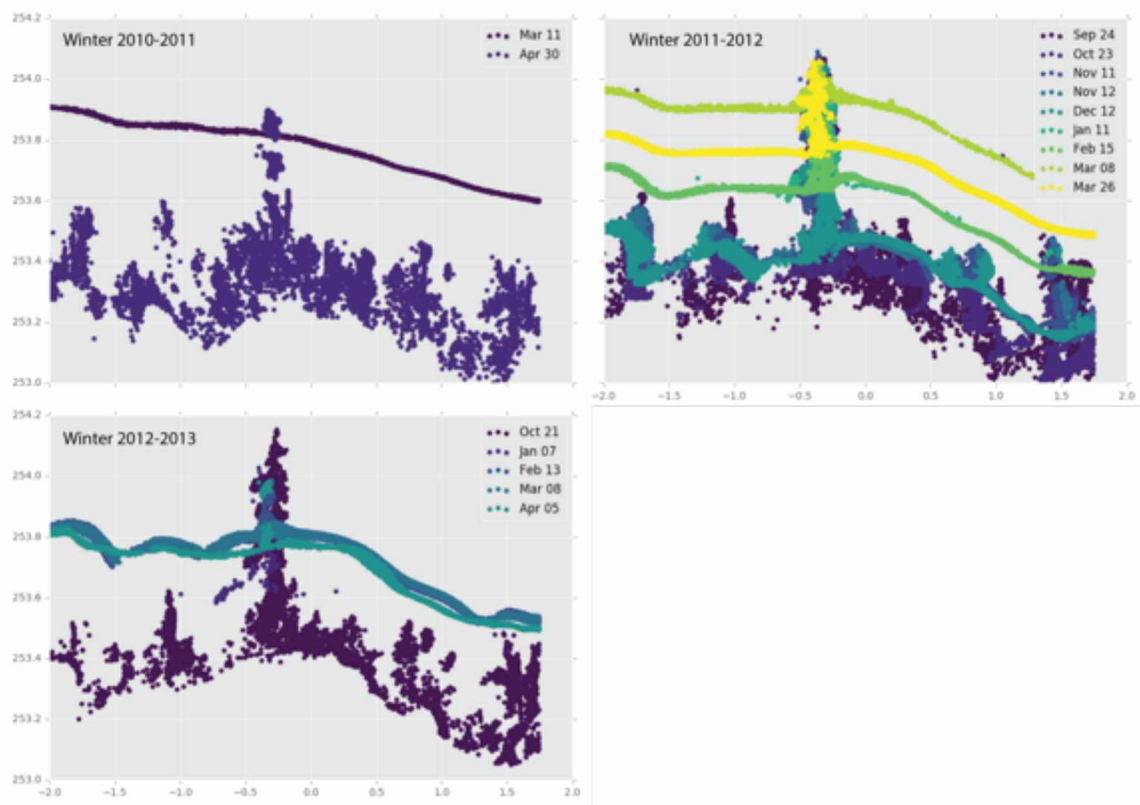
Figure 4.7: Vertical slices (10 cm thick) through the lidar point clouds for the three winter seasons 2010-2011, 2011-2012, and 2012-2013. The slices were arbitrarily picked to show a small spruce (<1 m). Notice how the spruce has grown by 25 cm in three years. All units are in meters.

Trees taller than a few meters interacted with snow in a different way. As described by *Miller* [1964] and *Bunnell et al.* [1985], the spruce canopy intercepted snowflakes on their descent. Snow bridging across twigs [*Schmidt and Gluns,* 1991] increased with time, as did the efficiency of interception. The net effect of this canopy interception was visible at the base of the tree, where the snow surface formed a depression, referred to as a *tree well* [*Sturm,* 1992]. In Figure 4.8 (a 5 cm thick slice of the point cloud) acquired during the 2011-2012 season, all of the above processes are visible. The first effect (interception) causes the branches to move up and down due to cycles of loading (snowfall) and unloading (wind-melt). Branch oscillations reach up to 20 cm at branch tips. The tree well becomes visible by February.

Figure 4.8: A 5 cm thick vertical slice of the season 2011-2012 lidar point clouds. Colors indicate the date of scanning. The spruce tree is marked in Figure 4.1.

While it can be hard to observe shedding of snow from trees, a bird's-eye view from the lidar data reveals the location of shed snow impacts on the snow surface (Figure 4.9). The snow fell from the tree in clumps, showing that while in the canopy it had sintered. The fact that impacts on Figure 4.9 are all on one side of the tree indicates that there was wind when the snow was shed, and in fact the wind probably triggered the shedding.
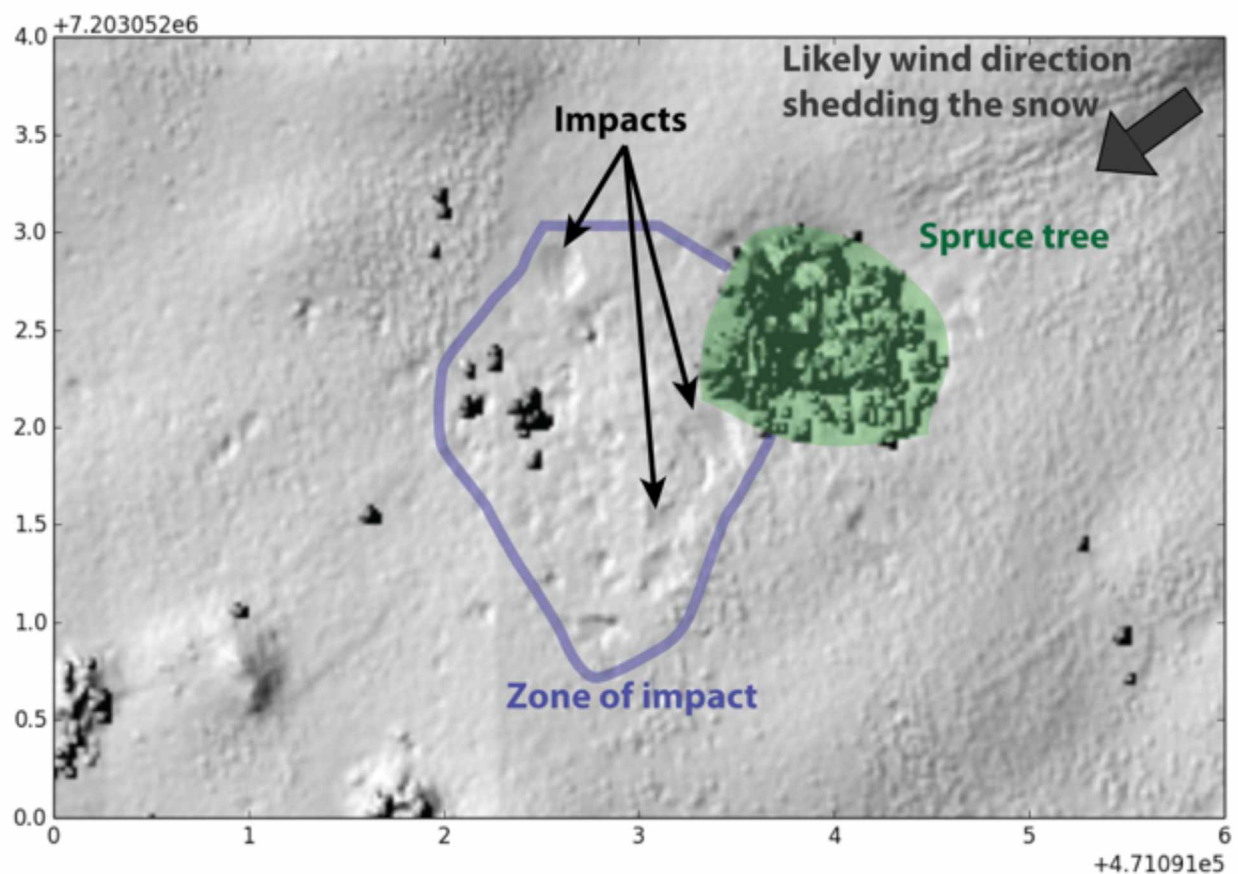
Figure 4.9: Hillshade view of the impacts left in the snow cover by clumps of snow falling from a spruce canopy. The black spots in the zone of impact are individual shrub branches protruding from the snowpack. Lidar scan from March 8, 2012. Units are in meters.

4.3.3 Understory

More widespread than trees, the understory shrubs covering the site exhibited distinct behavior during snowfalls. As the lidar data reveals in Figure 4.10, there were two distinct types of interactions with snow. In Figure 4.10a, shrubs protruded from the snow surface until December 20th, at which time new snowfall pushed them down. A smooth cover of snow replaced the rough snow and shrub surface. This snow cover did not exhibit any particular bumps or disturbances that

would reveal the presence of the underlying shrubs. In Figure 4.10b, the shrubs did not get buried under the snow until about February 15th. These shrubs did not totally disappear until March 26th and when they did, the snow surface maintained a permanent deformation indicative of their presence. These two different impacts on the local distribution of snow clearly highlight differences in stiffness of shrubs either due to mechanical properties of their branches, or to their canopy structures.
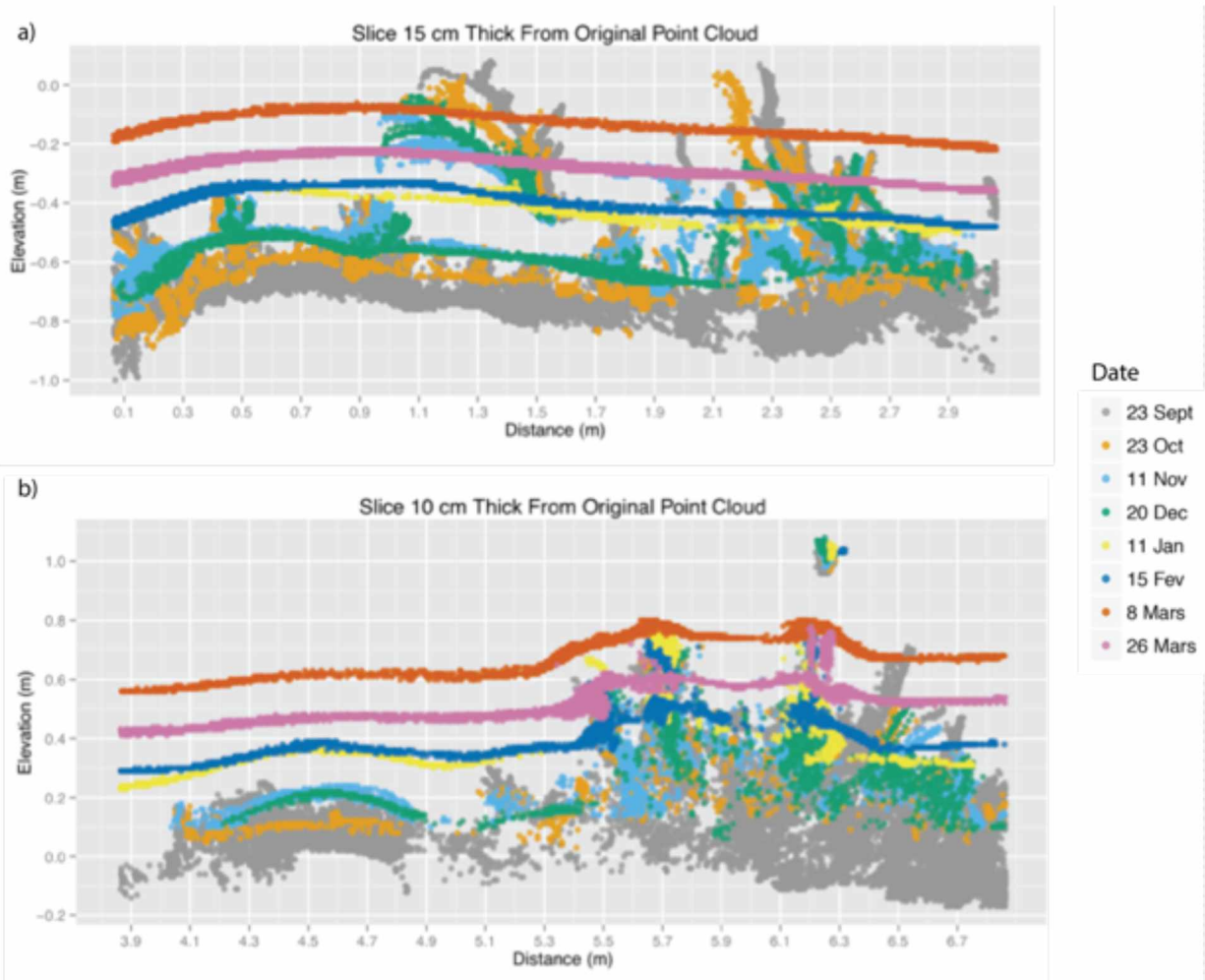
Figure 4.10: 15 cm thick vertical slices of the lidar point clouds for season 2011-2012 through two groups of shrubs. Colors indicate the date of scanning. In a) the shrubs (here dwarf birch (*Betula nana*)) get laid down by the snow load and become buried. Once this happens, the snow surface becomes smooth. In b) the shrubs get over-topped but do not lay down, so the surface reflects their presence till the end of winter.

At the scale of the entire site and through all three winters, the lidar results show a closely repeating pattern of shrub reactions to snow loading (Figure 4.11). Starting with a shrub layer 38 cm thick on average before there was any snow, we observed a rapid compression of the shrub understory once

loaded. For both winters, using the vertical distribution of the point cloud as a proxy for the quantity of protruding branches above the snow, we found that the point clouds became tighter with time across the whole site, reflecting the disappearance of shrub branches beneath the snow. Combined with the time-lapse video from the first season (2011-2012), this sharp disappearance of canopy protruding through the snow can be attributed to supple shrubs (mainly dwarf birch) getting bent and buried [*Sturm et al., 2005*].

However, this metric of point cloud spread extracted from the lidar has limitations. Indeed, on November 10th and 11th, 2011, for which we have scans, there was a sudden drop in the spread. Overnight, the wind had picked up to 5 m s^{-1} and shed snow off the protruding shrub branches. Because snow on branches creates a larger target for the lidar laser, there is more scatter recorded from snow-covered branches than bare branches. So with no real change in the amount of branches exposed, there was a change in the amount recorded by the point cloud. On the 10th the lidar received more returns from branches than on the 11th. This effect is clearly visible on the first graph of Figure 4.11.
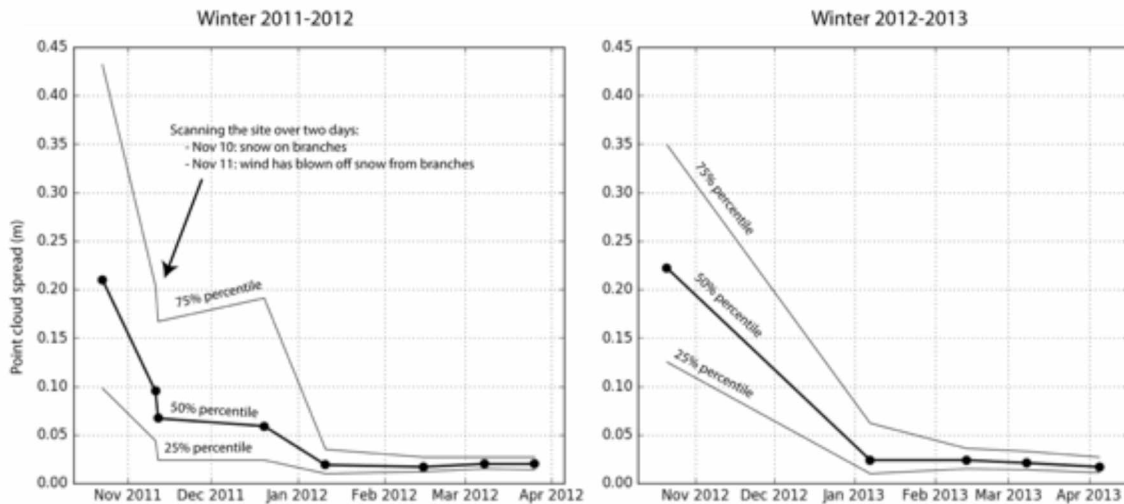
Figure 4.11: Evolution over two winter seasons of point cloud spreads (highest minus lowest point within a 10*10 cm pixel). Curves indicate the 25, 50 and 75 percentile of the spread over the 40*40 m area. Not only does the spread drop dramatically across the season, but also it can drop significantly overnight.

Because the lidar data lack the needed temporal resolution, we must use our time-lapse video to see how the snow buried the shrubs. For the winter 2011-2012, successive small snowfalls from the end of December to the first week of January were responsible for burying the shrub canopy. For the following winter, it was a single snowfall event on December 13th (29.3 cm) that buried the canopy.

The closeness in timing for both years' burial is most likely a coincidence, but the fact that snow depth reached 25-30 cm might indicate that a minimum snow depth is the critical parameter.

Despite a system that appears to be dynamic and might be expected to evolve differently depending on the succession of weather events, it is interesting to note the similarity and consistency of the end-of-winter snow cover distribution. Figure 4.12 shows the point cloud spread for three winters (2011, 2012, and 2013). For these three winters, with respectively 59.8, 54.0 and 65.9 cm of snow, the number of shrubs still protruding through the snowpack is basically the same (Figure 4.12).

Aside from shrubs, small spruce trees are the other plant that protrudes through the snow at the end of winter (Figure 4.7). Young spruce of a size equivalent to the snowpack form a natural shaft through the snow up which heat and moisture travel and are exhaled to the atmosphere. It is typical to observe large hoar frost growing at the upper opening of these natural air shafts, indicating an outward moisture and heat flux.
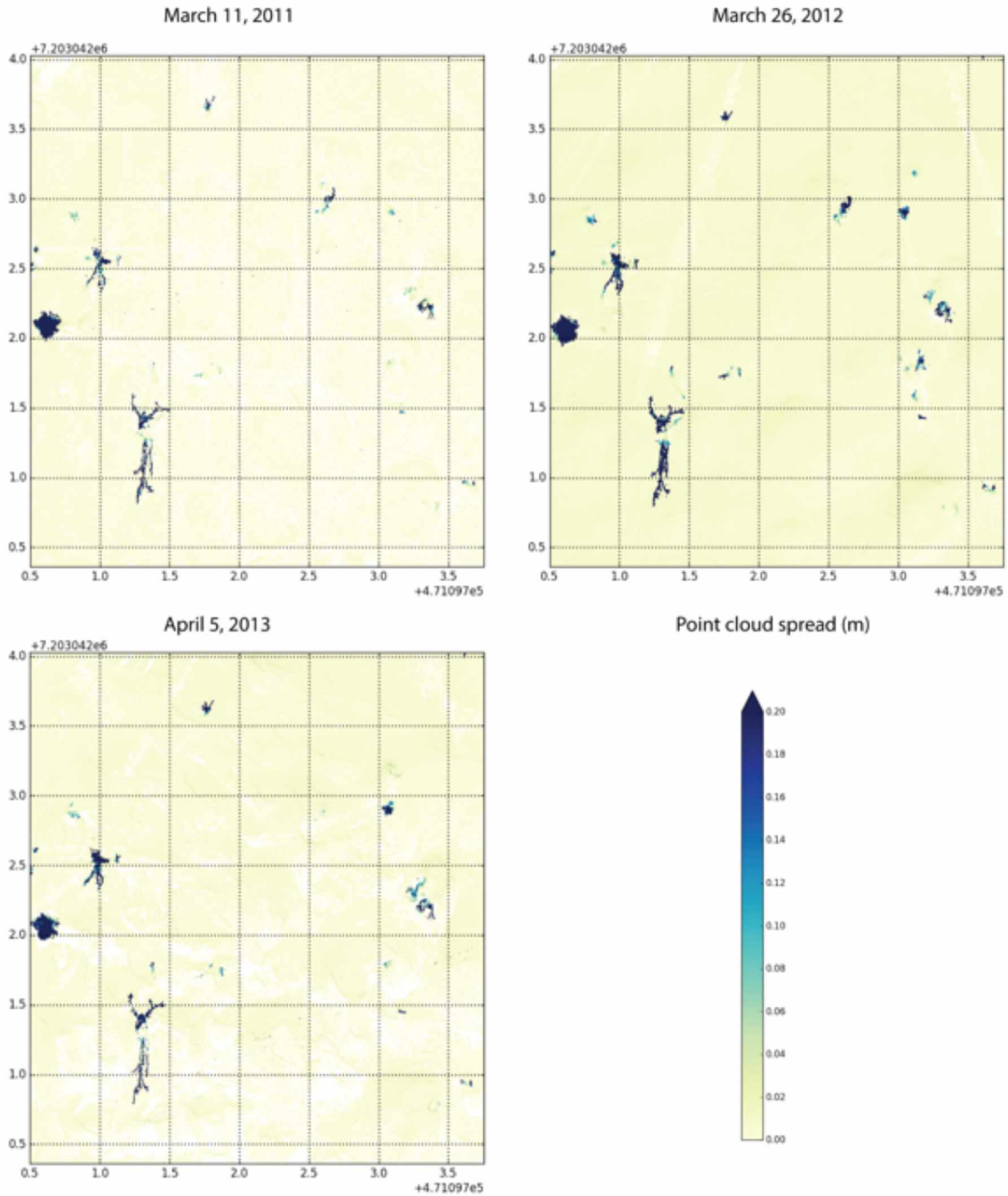
**Figure 4.12:** Point cloud difference between highest and lowest points (spread) by pixel (2*2 cm) for the last scan of the winter season (i.e. maximum snow accumulation). Elements above the snowpack appear in cyan to dark blue (>0.20 m), and the snow appears yellow. The map is projected in the UTM coordinates system in meters with North oriented up.

4.3.4 Subnivean Air Cavities

Below the shrub canopy and above the ground we often found air pockets when digging snowpits. This zone has been named the subnivean space by ecologists [*Pruitt*, 1958; *Pauli et al.*, 2013] and has been shown to be the habitat and refuge for many mammals, insects and arthropods during the winter season. While several studies [*Schmidt and Lockwood*, 1992; *Korslund and Steen*, 2006; *Aitchison*, 2011; *Bilodeau et al.*, 2013] have focused on the impact of the subnivean space on the fauna and flora of the taiga, its definition in terms of physical characteristics is less clear, with the limited exception of its temperature and CO_2 accumulation [*Starr and Oberbauer*, 2003]. In what follows we will use the term subnivean space to mean the specific case where there is an air gap between the bottom of the snowpack and the ground.

We found that a subnivean space could form early and remain present throughout the whole winter. Based on snowpit observations, we have plotted (Figure 4.13) the ratio of air cavities to total cross-sectional area of each snowpit we measured. In early winter, the air cavities occupied as much as 55% of the snowpack section. This significantly decreased as snow accumulated, but instead of being reduced to zero at the end of winter, the value reached a plateau of about 10% at the end of the season. This presence of air cavities is therefore not only interesting for its ecological importance but also for its impact on snow depth and SWE estimation. When using typical snow instruments (*e.g.* a ruler or a lidar) we assume that the full thickness of the measurement is snow, but the presence of air cavities might suggest that this value is too high by as much as 10% at the end of winter.
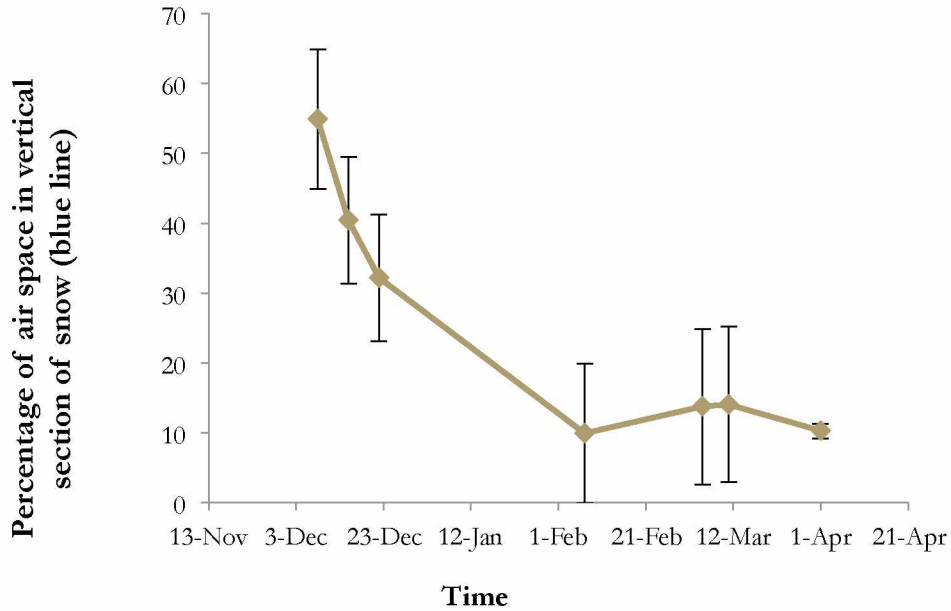
Figure 4.13: Percentage of air cavities over time based on snowpit cross-sections for the winter season 2011-2012.

As seen in Figure 4.14, air cavities exposed in three snowpits each 4 m long and separated by 20 cm were not isolated. Cavities in one cross section extended in the third dimension and connected with neighboring cavities. These cavities were often located below or at the same level as the upper bound of the vegetation buried in the snow.

When we look at the plant species associated with the presence and size of air cavities, we find that four plants were prevalent (Figure 4.15). Sedges (*Carex sp.*) were associated with the largest (deepest) air cavities, some up to 30 cm high. Because of their shapes and how close together they can be located, sedges can form a thick canopy that prevents snow from accumulating around their bases. The second plant species most associated with air cavities was the dwarf birch (*Betula nana/glandulosa*). Already mentioned for its capacity to bend under snow load (section 4.3.3), this plant was responsible for the formation of the second largest air cavities. Finally, Labrador-tea (*Ledum sp.*) and blueberry (*Vaccinium alaskaense*) were also found coincident with air cavities.
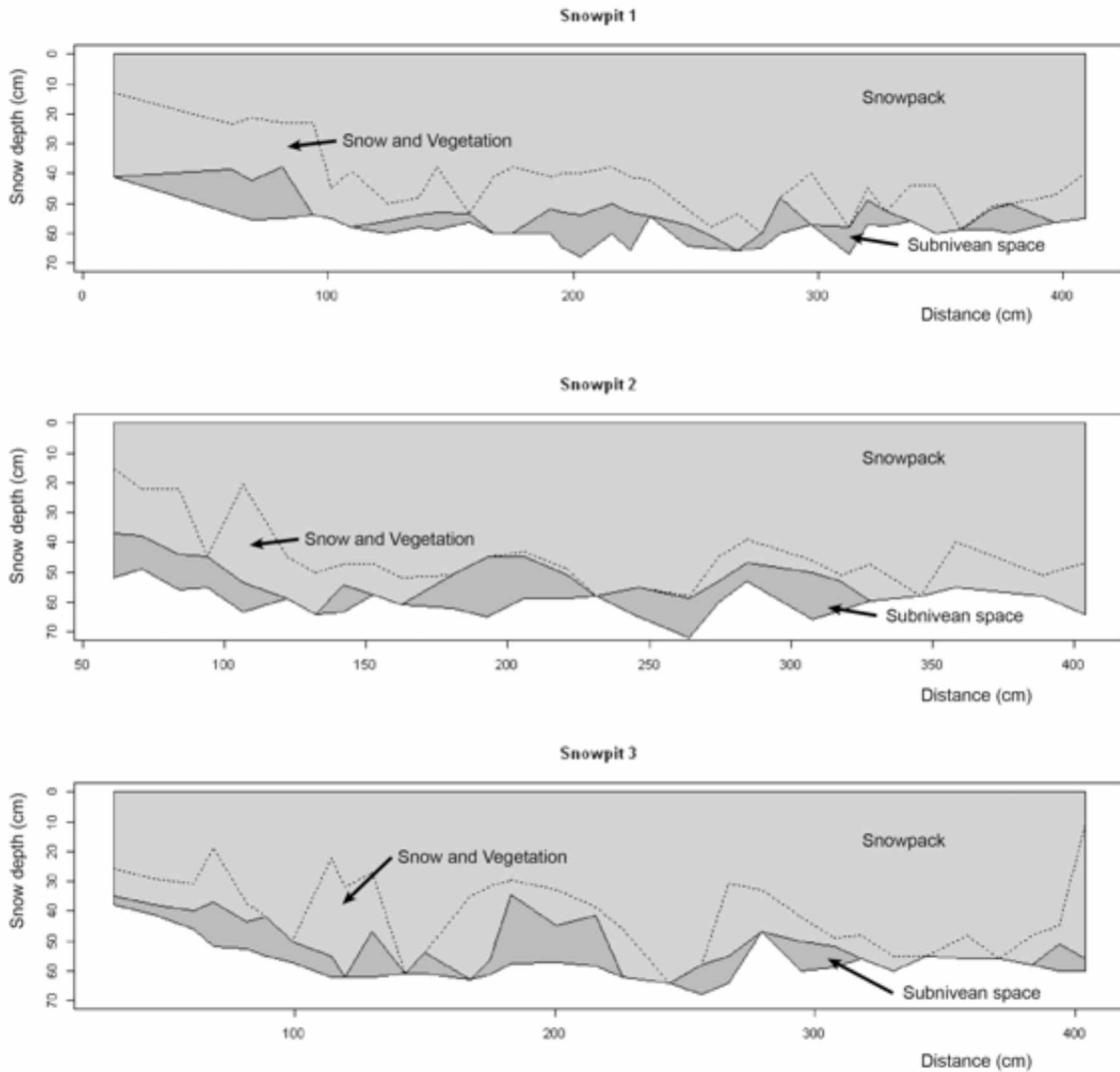
Figure 4.14: Three 4-m long snowpits indicating the ground (white), the bottom of the snowpack, and the maximum height of the vegetation within the snowpack (dotted line). Subnivean spaces are indicated by dark grey shading. All vertical measurements are referenced to the top of the snowpack, which here is forced to be flat and horizontal. Each snowpit was cut back 20 cm from the previous one.

130
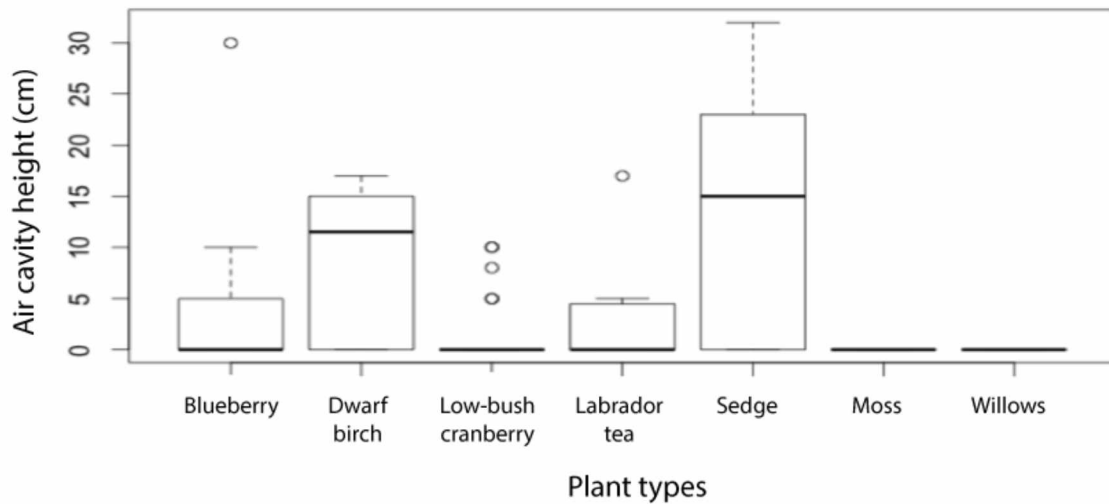
Figure 4.15: Boxplot of the air cavity heights sorted by the plant type present at each cavity.

Air temperature played a big role in determining when and if there would be a subnivean space. During the first snowfall on October 17, 2011, temperatures were nearing 0°C, producing snowflakes with high adhesion forces that were intercepted by plant canopies and stuck to them. As a consequence, the snowpack formed a continuous cover separated from the ground by low-bush cranberry and other small but densely branched plants that formed a continuous net. In contrast, the following year, because the first snowfall arrived when temperatures oscillated around -6 °C, we observed that snowflakes fell through the same canopy and reached the ground, accumulating around the same small canopy plants (*e.g.* low-bush cranberry) and filling the space instead of forming an air gap.

4.3.5 At the Plot Scale

The lidar data reveal patterns of snow accumulation in the boreal forest at the plot scale that were repeated year after year with surprising similarity. Figure 4.12 shows this similarity for the shrub cover, but it extends to areas of trees and areas without shrubs (Figure 4.16).

The three upper maps of Figure 4.16 show the snow surface elevation with respect to the mean elevation for three end-of-winter scans (last scan before the melt season). The next two rows of maps correspond to 1) a low pass filter at 2 m, and 2) a high pass filter at 2 m of the maps shown in the first row. With this decomposition of the snow surface, we see that the larger scale variability

(low-pass filtered maps) of the snowpack converges to similar spatial patterns. For both filtered map series, the patterns from 2012 and 2013 appear closer to each other than the ones from March 2011.
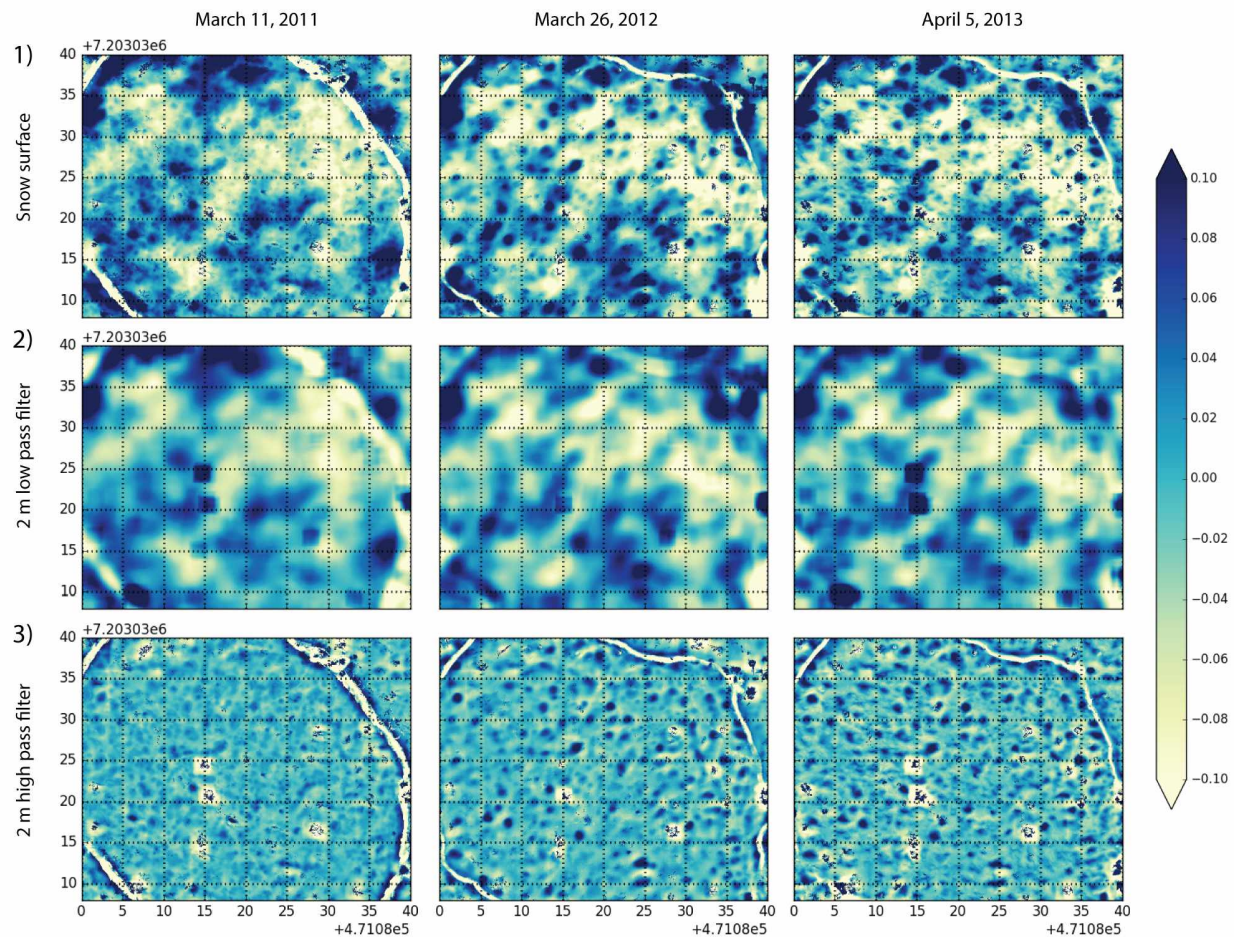
Figure 4.16: Variation from the mean of the snowpack surface elevation in meters. Each column corresponds to 1) the actual snow surface map derived from lidar, 2) a low-pass filter of the maps at 2 m, and 3) a high pass filter at 2 m. The bright track visible on the original and the high-pass filtered image corresponds to the path in the snow around the site. The dark blue spots appearing as squares in the low-pass maps are processing artifacts generated by noise left from filtering out spruce trees. All maps are projected in the UTM coordinate system in meter with a 2*2 cm pixel size. The y-axis is oriented with the geographical North direction.

To get an insight into the origin of these long wavelength spatial patterns in the snow surface, we can seek clues in the surface topography. The map derived in Figure 4.17 shows the lowest laser returns collected from eight scanning positions on September 29, 2011. Despite a greater number of scanning positions, the scanner was not able to provide an actual bare ground map because of the shadowing effect created by the micro-topography (hummocks and tussocks), and the thick layer of shrubs. Nevertheless, this map provides good indications on the location of hummock tops

throughout the site (in dark blue). We have overlain with red dots the location of high points of the snow surface bumps. Their locations coincide exactly with higher points of the topography indicating that the snow surface geometry after a whole winter still carries information from the underlying topography.
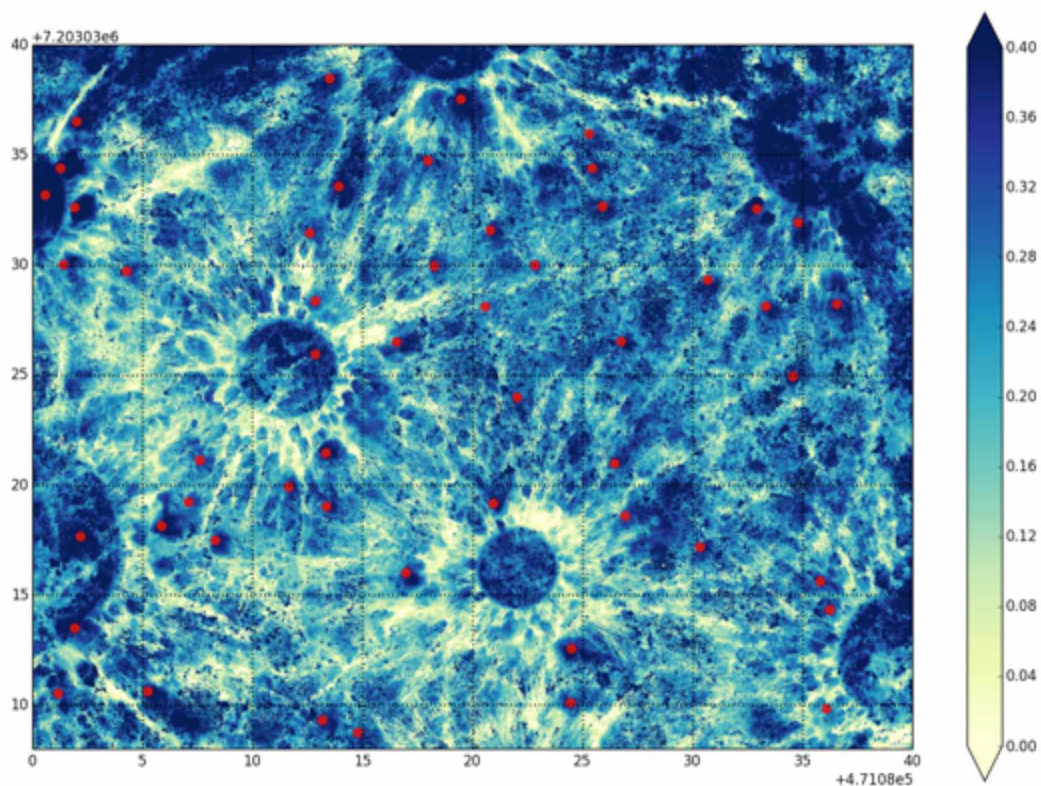
Figure 4.17: A near bare ground surface extracted from summer lidar data. Red dots indicate large snow bumps manually localized based on March 2012 snow cover. The color-coded elevation is given in meters, ranging from 250.0 m to 250.4 m above sea level. The blue circular patterns are artifacts from the lidar at the scanning positions. Due to a shadowing effect by micro-topography and shrub branches, the lidar preferentially sees deeper the closer the returns are from the scanning station.

4.4 Discussion

The development of the snowpack in the boreal forest involves a multitude of interactions shaping the bottom and the top interfaces of snow around several vegetation canopies. We find that while the snow cover forms by the deposition of single snowflakes [*Filhol and Sturm*, in Prep], its interaction with the plant canopies strongly depends on the type and geometry of the canopy. Figure 4.18 summarizes in a sketch the five main types of canopies we identified impacting locally the distribution of snow:

- Tree canopies remaining all winter above the snow surface. They are encountered first by snowflakes, and these canopies intercept enough snowflakes to cause a local depression of the snow beneath the canopies.

- Stiff shrubs (that do not bend) act locally as a second canopy and an obstacle for snow deposition, deforming the snowpack surface geometry locally where they protrude.

- Supple shrubs that are slowly buried by the increasing snow accumulation through the winter. These shrubs seem to have a threshold snow depth, above which they bend over and are subsequently buried by snow. We think this threshold is dictated by a balance between the shrub size relative to the snow depth [*Sturm et al.*, 2005], and the architecture of the shrub canopy [*Ménard et al.*, 2014]. Where these shrubs densely populate an area, their supple branches can form an overarching platform that prevents snow from reaching the ground, leading to the creation of air cavities.

- Young coniferous trees (size equivalent to snowpack) that form local air cavities in the shape of a shaft across the snowpack (a special case of the previous point). The conifers are stiffer than shrubs, and so rarely bend over.

- Tussock canopies shedding snowflakes around them, leaving a circular air space around their base. Tussocks also locally raise the bottom of the snowpack, which later translates into bump signatures on the snow surface.
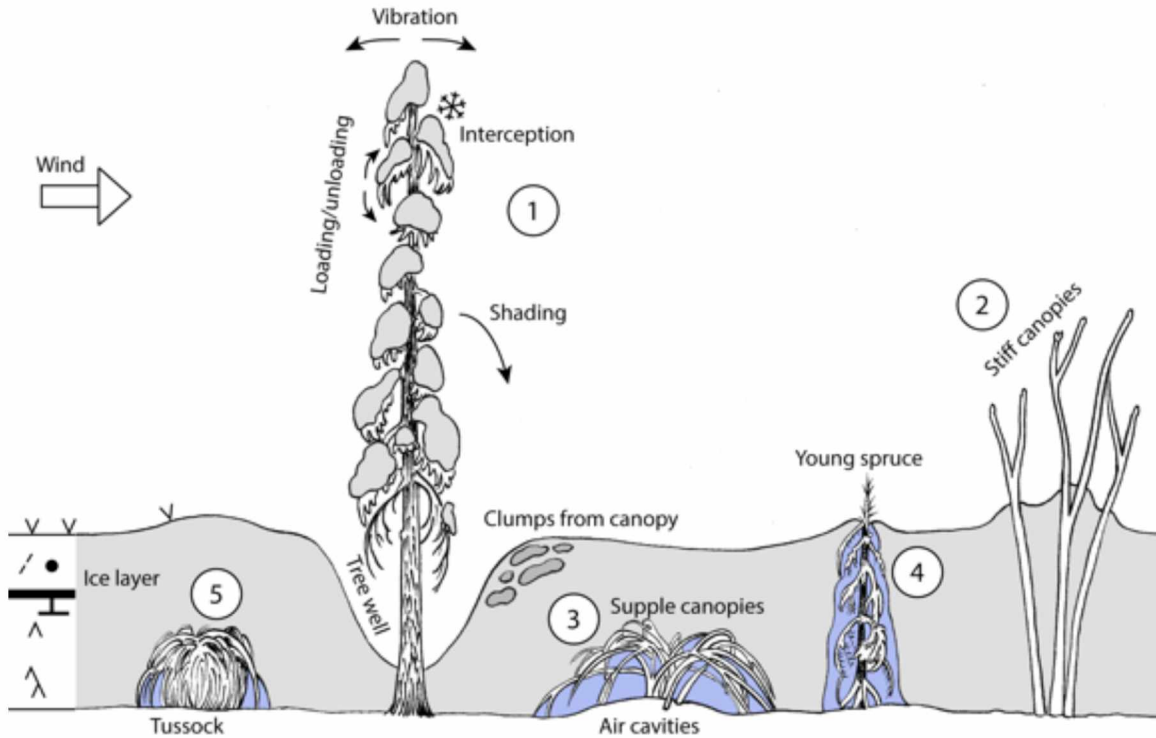
Figure 4.18: Sketch summarizing the spectrum of interactions involved between snow and the boreal forest vegetation. Snow is represented by gray shaded regions, and air cavities by the blue shaded regions. Numbering indicates: 1) Tree canopies, 2) stiff shrubs canopies, 3) supple shrubs canopies, 4) small evergreen trees, and 5) tussocks canopies. Illustration by Sarah DeGennaro.

In 2005, *Sturm et al.* proposed a ratio (λ) of snow depth (h_s) to shrub height (h_b) for capturing the interaction of shrubs with the snow cover:

$$\lambda = \frac{h_s(t)}{f(t) \cdot h_b} \qquad (4.1)$$

f(t) is a compression factor ranging from about 0.1 to 1, that is also function of time (*t*). Originally applied as an aid in interpreting the time evolution of the snow surface albedo, this ratio is equivalently applicable to the cases shown here. In fact, the ratio can be expanded more generally to all five canopy elements mentioned previously. For tall spruce trees, $\lambda << 1$, because the snow pack depth always is lower than the height of these tall (and stiff) canopies. For the canopy covering the ground (mosses, low-bush cranberry), $\lambda >> 1$, because their canopy height is extremely small in comparison to the snow depth. When $\lambda \approx 1$, the case that includes young spruce trees, stiff shrubs,

135

supple shrubs, and tussocks, we observed more complex behavior and generally the presence of air cavities at the base of the snow.

When a snowflake comes down, it interacts with the landscape following the same processes highlighted in Chapter 3. Bouncing, cohesion, adhesion, creep, bridging, etc. occurs as the snowflakes encounter branches, spruce needles, shrubs, or moss surfaces. The behavior described in Chapter 3 applies the same way in forests, though the surfaces encountered are more complex (largely discontinuous, and in addition, deformable). Bridging and deflection of snowflakes become visible when air cavities form at the bottom of the snowpack. These cavities can reach about 10 % of the snowpack section at the end of winter. Also, as demonstrated in Chapter 3, we find that both the variability of snow influx and the geometry of the underlying ground are the main controls on the redistribution of the snow. We observe that a spruce canopy, by shadowing the ground and preventing snow from falling close to the tree trunk, creates a smooth depletion in the snowpack (tree well). Also, as shown in figures 4.16 and 4.17, the underlying topography drives the shape of the snowpack, repeating similar accumulation patterns (scale ≥ 2 m) over the years.

Despite two different sequences of weather events in winter 2011-2012 and 2012-2013, we find the understory canopy responded similarly in both seasons. Beyond an accumulation of 25-30 cm, supple shrubs became fully buried, leaving at the end of winter, the same individuals protruding the snow surface (Figure 4.12). From this set of observations , we think that if the climatological conditions are bounded, then the substrate (ground topography and canopy architecture) seems to be the main driver of snow distribution.

4.5 Conclusion

This chapter reports results and preliminary interpretations from an experiment run at Glenn Creek, Fox, Alaska, over the course of three years. The site was located in a low-land black spruce forest, with trees sparsely distributed and surrounded by a thick (38 cm) layer of shrubs, and tussocks. To track the evolution of the snowpack, we used a terrestrial lidar, in addition to more traditional instruments. With this state-of-the-art tool, we were able to produce maps of snow distribution across a site of 2000 m^2, as well as vertical cross sections comparing point clouds from multiple dates. The lidar gave us new insights into the dynamic of the forest while snow was depositing,

allowing in particular, the tracking of the shrub canopies as they were loaded with snow. Because the lidar sensor can only detect the top of the snowpack, we dug pits to follow the bottom and layering of the snow.

We found that through the course of a winter, the landscape changed significantly following the sequence of weather events. Based on their impact on snow distribution we found five distinctive types of canopies in the landscape: trees (spruce), young spruce, stiff shrubs, supple shrubs, and tussocks. Some of these canopies have a larger impact on the snowpack bottom (*e.g.* tussocks), while others, like trees, mainly influence the shape of the snow cover top. Despite different weather histories for each of the three years, the end of winter snow documented by the lidar showed very similar spatial patterns. Canopies too, showed similar reactions to snow loading across several winters.

This experiment gave us some new insights into the dynamics of snow deposition in the forest. It allowed us to identify key elements for which new experiments would help further our understanding of the complex way that the taiga interacts with falling and settling snow. For instance, our monitoring of the subnivean space suggests the need for more studies to document in greater detail the spatial extent, the formation processes, and the temporal evolution of these air cavities. For this purpose, we designed a probe that was able to detect the presence of air cavities under the snow. Potentially, the device would have been able to produce geo-located profiles of snow versus air space. We did not acquire enough data to explore the 3-D nature of the subnivean space, largely because the apparatus was still under development, but if further developed, it could help us to explore this critical habitat and document its extent and geometry.

Now that lidar technology is more accepted and widespread as a tool for measuring snow depth in forested regions, developing knowledge of the subnivean space and the processes that produce it, is likely to become more needed. In our study, up to 10% of the volume between the ground interface and the snow cover top was air cavities at the time of maximum accumulation, which if unknown, could lead to an overestimation of the total amount of snow. The formation process of these air cavities is also fascinating and is going to require a separate set of experiments and observations. We found that these cavities tended to be associated to specific species, suggesting that the properties of canopy and the process of bridging are key to their formation.

The shrub canopy, with its $\lambda \approx 1$, is the most problematic and challenging of the canopies we observed. Our lidar experiment at a plot scale of about 50 m was only able to capture some of the interactions taking place between the vegetation and the snow. Shrubs have thin branches (a few millimeters in diameter). With the chance of being detected by the lidar decreasing with distance, the zone in which our measurements are useful was quite limited. Shrubs are diverse in size, species, canopy architecture, and stiffness, so a smaller scale experiment using a similar approach with lidar (potentially automatized) would facilitate obtaining a greater characterization of the canopy structure and of the ground surface. It would increase the consistency in the detection of individual branches and it would therefore be possible to track individual branches in response to snow loading. In complement, we could imagine placing multiple time-lapse cameras, and lastly with a smaller plot, we could generate a detailed botanical description.

Acknowledgements

References

Bilodeau, F., G. Gauthier, and D. Berteaux (2013), The effect of snow cover on lemming population cycles in the Canadian High Arctic, *Oecologia*, 172(4), 1007–16, doi: 10.1007/s00442-012-2549-8

Bonfils, C., T. Phillips, D. Lawrence, and P. Cameron-Smith (2011), On the influence of shrub height and expansion on boreal climate, *No. LLNL-JRNL-495260*. Lawrence Livermore National Laboratory (LLNL), Livermore, CA.

Bret-Harte, M. S., G. R. Shaver, J. P. Zoerner, J. F. Johnstone, J. L. Wagner, A. S. Chavez, R. F. Gunkelman IV, S. C. Lippert, and J. A. Laundre (2001), Developmental plasticity allows Betula nana to dominate tundra subjected to an altered environment, *Ecology*, 82(1), 18–32, doi: 10.1890/0012-9658(2001)082[0018:DPABNT]2.0.CO;2

Bunnell, F. L., R. S. McNay, and C. C. Shank (1985). Trees and Snow: The Deposition of Snow on the Ground: a Review and Quantitative Synthesis. *Research, Ministries of Environment and Forests*.

Chapin III, F. S., T. V. Callaghan, Y. Bergeron, M. Fukuda, J. F. Johnstone, G. Juday, and S. A. Zimov (2004), Global Change and the Boreal Forest: Thresholds, Shifting States or Gradual Change?, *Ambio Journal of the Human Environment*, 40(6), 361–365, doi: 10.1579/0044-7447-33.6.361.

Davis, R. E., J. P. Hardy, W. Ni, C. Woodcock, J. C.McKenzie, R. Jordan, and X. Li (1997). Variation of snow cover ablation in the boreal forest: A sensitivity study on the effects of conifer canopy. *Journal of Geophysical Research Atmospheres*, 102, 29, doi: 10.1029/97JD01335.

Dingman, S. L. (1971). Hydrology of the Glenn Creek Watershed Tanana River Basin, Central Alaska. *No. CRREL-Reasearch Report-297*.

Ellis, C. R., J. W. Pomeroy, T. Brown, and J. MacDonald (2010) Simulation of snow accumulation and melt in needleleaf forest environments. *Hydrology and Earth System Sciences*, 14, 925-940, doi: 10.5194/hess-14-925-2010.

Epstein, H., I. Myers-Smith, and D. Walker (2013), Recent dynamics of arctic and sub-arctic vegetation, Environmental Research Letter, 8(1), 015040, doi: 10.1088/1748-9326/8/1/015040.

Fastie, C., A. Lloyd, and P. Doak (2002), Fire history and postfire forest development in an upland watershed of interior Alaska, *Journal Geophysical Research Atmospheres*, *107, 8150*, doi: 10.1029/2001JD000570.

Filhol, S., and M. Sturm (2015), Snow bedforms: A review, new data, and a formation model, *Journal of Geophysical Research Earth Surface*, *120*, *1645–1669*, doi: 10.1002/2015JF003529.

Filhol, S., and M. Sturm (in Prep), How Falling and Settling of Snowflakes Smooth a Landscape, Prepared for submission to the Journal of Geophysical Research Earth Surface.

Hedstrom, N. R., and J. W. Pomeroy (1998). Measurements and modeling of snow interception in the boreal forest. *Hydrological Processes*, *12*(1011), 1611-1625, doi: 10.1002/(SICI)1099-1085(199808/09)12:10/11<1611::AID-HYP684>3.0.CO;2-4J.

Kaplan, O., N. H. Bigelow, I. C. Prentice, S. P. Harrison, P. J. Bartlein, T. R. Christensen, W. Cramer, N. V. Matveyeva, A. D. McGuire, D. F. Murray, V. Y. Razzhivin, B. Smith, D. A. Walker, P. M. Anderson, A. A. Andreev, L. B. Brubaker, M. E. Edwards, and A. V. Lozhkin (2003), Climate change and Arctic ecosystems: 2. Modeling, paleodata-model comparisons, and future projections, *Journal of Geophysical Research Atmosphere*, *108*, 8171, doi: 10.1029/2002JD002559.

Korslund, L., and H. Steen (2006), Small rodent winter survival: snow conditions limit access to food resources, *Journal of Animal Ecology*, *75*, 155-156 doi: 10.1111/j.1365-2656.2005.01031.x.

Liston, G., and C. Hiemstra (2011), Representing Grass– and Shrub–Snow–Atmosphere Interactions in Climate System Models, *Journal Climate*, *24*(8), 20612079, doi: 10.1175/2010JCLI4028.1.

Lozhkin, A., and P. Anderson (2013), Late Quaternary lake records from the Anadyr Lowland, Central Chukotka (Russia), *Quaternary Science Reviews*, *68*, 116, doi: 10.1016/j.quascirev.2013.02.007.

Lundquist, J., S. Dickerson-Lange, J. Lutz, and N. Cristea (2013), Lower forest density enhances snow retention in regions with warmer winters: A global framework developed from plot-scale observations and modeling, *Water Resource. Research*, *49*(10), 6356–6370, doi: 10.1002/wrcr.20504.

Ménard, C., R. Essery, J. Pomeroy, P. Marsh, and D. Clark (2014), A shrub bending model to calculate the albedo of shrub-tundra, *Hydrological Processes*, 28, 3541-351, doi: 10.1002/hyp.9582.

Miller, D. H. (1964), Interception processes during snowstorms. Research Paper PSW-RP-18. Berkeley, CA: Pacific Southwest Forest & Range Experiment Station, Forest Service, U. S. Department of Agriculture; 24 p.

Moeser, D., M. Stähli, and T. Jonas (2015). Improved snow interception modeling using canopy parameters derived from airborne LiDAR data. *Water Resources Research* 51, no. 7 (2015): 5041-5059, doi: 10.1002/2014WR016724.

Myers-Smith, I. H. and C. S. Elmendorf, P. S. A. Beck, M. Wilmking, M. Hallinger, D. Blok, K. D. Tape, S. A. Rayback, M. Macias-Fauria, B. C. Forbes, J. D. M. Speed, N. Boulanger-Lapointe, C. Rixen, E. Levesque, N. M. Schmidt, C. Baittinger, A. J. Trant, L. Hermanutz, L. S. Collier, M. A. DawesT. C. Lantz, S. Weijers, R. H. Jorgensen, A. Buchwal, A. Buras, A. T. Naito, V. Ravolainen, G. Schaepman-Strub, J. A. Wheeler, S. Wipf, K. C. Guay, D. S. Hik, M. Vellend (2015), Climate sensitivity of shrub growth across the tundra biome, *Nature Climate change, 5* (9), 887–891, doi: 10.1038/nclimate2697.

Okitsu, S., and K. Ito (1984), Vegetation dynamics of the Siberian dwarf pine (Pinus pumila Regel) in the Taisetsu mountain range, Hokkaido, Japan, *Vegetatio*, doi: 10.1007/BF00044934.

Pauli, J., B. Zuckerberg, J. Whiteman, and W. Porter (2013), The subnivium: a deteriorating seasonal refugium, *Frontiers in Ecology and the Environment, 11*, doi: 10.1890/120222.

Pruitt, W. O. (1958), Quali, a Taiga Snow Formation of Ecological Importance, *Ecology, 39*(1), 169–172.

Rutter, N., R. Essery, J. Pomeroy, N. Altimir, K. Andreadis, I. Baker, A. Barr, P. Bartlett, P., Boone, H. Deng, and H. Douville (2009), Evaluation of forest snow processes models (SnowMIP2), *Journal of Geophysical Research*, 114(D6), doi:10.1029/2008JD011063

Schmidt, R. A., and D. Gluns (1991), Snowfall interception on branches of three conifer species, *Canadian Journal of Forest Research*, 21(8), 1262–1269, doi: 10.1139/x91-176.

Schmidt, P., and J. A. Lockwood (1992), Subnivean arthropod fauna of southeastern Wyoming: habitat and seasonal effects on population density, *American Midland Naturalist*, 66–76.

Starr, G., and S. F. Oberbauer (2003), Photosynthesis of Arctic evergreens under snow: implications for tundra ecosystem carbon balance. *Ecology* 84: 1415-1420, doi: 10.1890/02-3154

Sturm, M. (1992), Snow distribution and heat flow in the taiga, *Arctic and Alpine Research*, 145-152.

Sturm, M., J. Holmgren, and J. P. McFadden (2001), Snow-shrub interactions in Arctic tundra: a hypothesis with climatic implications, *Journal of Climate, 14*(3), 336-344.

Sturm, M., T. Douglas, C. Racine, and G. Liston (2005), Changing snow and shrub conditions affect albedo with global implications, *Journal of Geophysical Research Biogeosciences, 110*(G1), doi: 10.1029/2005JG000013.

U.S. Geological Survey NLCD (2001) Land Cover Alaska - National Geospatial Data Asset (NGDA) Land Use Land Cover

Van Cleve, K., F. S. Chapin III, P. W. Flanagan, and L. A. Viereck (1986), Forest ecosystems in the Alaskan taiga. *Springer-Verlag*.

Varhola, A., N. Coops, M. Weiler, and D. Moore (2010), Forest canopy effects on snow accumulation and ablation: An integrative review of empirical results, *Journal of Hydrology, 392*, doi: 10.1016/j.jhydrol.2010.08.009.

Viereck, L. A., C. T. Dyrness, A. R. Batten, and K. J. Wenzlick (1992). The Alaska vegetation classification (p. 278). Portland, OR, USA: *US Department of Agriculture, Forest Service*, Pacific Northwest Research Station.

Yarie, J. (1981), Forest fire cycles and life tables: a case study from interior Alaska, *Canadian Journal of Forest Research*, 11:554-562, 10.1139/x81-076

CHAPTER 5: Conclusions

Snow is unique in the natural world. Every winter, with one snowflake falling after another, snow alters the landscapes of the alpine and northern regions of the Earth for multiple months at a time. This widespread and seasonal presence deeply affects ecosystems, hydrology and climate [*Walker et al.*, 1993; *Mote*, 2008; *Orsolini and Kvamtø*, 2009]. Snow reflects sunlight, insulates the ground, loads plant canopies, forms a refuge in winter for small animals and plants, and is a source of the large influx of water that enters streams and rivers during the melt period. So understanding the variability of snow distribution at various scales provides key insights into the dynamic of northern ecosystems.

Instrumental and modeling tools developed by the scientific community tend to either focus on the grain scale (micrometer to centimeter), where researchers look at snowflake shapes, sizes and metamorphism, or these tools focus on scales of snow distribution larger than 10 m. For example the scale of satellite sensors (microwave or visible sensors) for measuring snow cover extent or snow water equivalent range from 10 m to 100 km. Redistribution models [*Brun et al.*, 1989; *Bartlett and Lehning*, 2002; *Liston and Sturm*, 2002] operate at scales equivalent to satellite sensors. For bridging the scale gap, sensors like lidar scanners used from low flying platforms or from the ground, can provide information about the snow distribution at scales ranging from centimeters to 100 meters. Also, models simulating snow accumulation in forests that incorporate grain-scale processes can generate snow distributions sensitive to the centimeter scale, but to date these are associated with a large amount of uncertainty [*Rutter et al.*, 2009]. Exploring linkages between the physics occurring at the grain scale to the deci/decameter scale is absolutely essential if we want to improve our understanding of snow distribution variability at scales relevant to the study of ecosystem processes.

In this study, I have identified linkages between grain-scale processes and centimeter to decameter snow distributions for two types of snow, polar and taiga snow. For example, the creep and saltation of individual snow grains leads to the development of dunes and other snow bedforms that may be tens of meters in extent. The ultimate size of these forms is limited by the sintering of snow grains (Chapter 2). Another example is the smoothing of landscapes and tree branches by the deposition of snow. This smoothing process requires individual grains to move laterally (Chapter 3).

The use of new tools, in particular a lidar scanner, allowed me to formulate and answer questions about macro-scale features that were rooted in grain-scale processes. In this respect, I revisited and explored linkages between grain scale and macro-scale features that were partially known to the snow science community, but had not been explored in full. My work is inspired by old, and still quite sound and useful research, like that done by Bagnold in the first half of the 20th century [*Bagnold*, 1941] to work done by R.A. Schmidt's group [*Schmidt*, 1980; *Schmidt and Gluns*, 1991] in the latter part of the 20th century. I also drew upon knowledge from other fields like sand desert science, as well as new fields like computer vision and theoretical mathematics on fractals. In particular, though, I owe a debt to the work done by Japanese researchers between 1960 and 1980, who were pursuing linkages between snow grain-scale processes and landscape snow cover, and made significant progress along that path before they (inexplicably) dropped that research thrust in the 1980s.

The three chapters presented above explore, for two types of atmospheric conditions (windy versus calm), how the shapes of snowpack surfaces evolve in time and with various weather conditions. My observations, in combination with previous knowledge of individual processes, led me to start defining new frameworks for approaching the study of some of these linkages. Chapter 2, building on a collection of lidar models of wind blown snow surfaces, and a review of existing classifications of these surfaces, led to improved understanding of both the geomorphology and genesis of these snow bedforms. The chapter ends with a new genetic classification system of these forms. Chapter 3, which was motivated by the need to look at simple versions of the system explored in Chapter 4, explores how snow transforms and smooths the geometry of the landscapes on which it falls, and for the first time identifies the full set of processes that allow this transformation to occur. A series of novel experiments on snow grain bouncing and angle of repose feed this larger understanding of the smoothing process. I investigated a complex landscape, that of the boreal forest, in Chapter 4. To understand snow in this landscape, I used the knowledge developed in Chapter 3 (and to a lesser extent, Chapter 2) for interpreting the sequential lidar observations of snow deposition in the forest. This line of study is not complete: the taiga landscape, with its five canopy elements, interacts with snow in very complex ways that will take considerably more study before it is understood.

In Chapter 2, which is about snow bedforms, I learned that the size of snow bedforms is a function of the flux of snow transported by wind, itself depending on wind speed and the erodibility of the

snow surface. When individual snow particles are entrained by wind and bombard the snow surface, snow hardness directly controls erodibility. Through my review, I found that hardness was a key component in the development of these rough surfaces. Hardness of snow increases over time because of sintering, a process forming bonds between ice particles. Using a simple model, I was able to show that due to the single effect of sintering, snow bedforms could not grow over long timescales as can sand bedforms. This simple model explains why we do not see 10-100 m tall snow dunes, as might be expected by analogy with sand dunes. The model also led me to the conclusion that with time, any snow dune would eventually be carved into sastrugi, the most widespread features of polar snow. Using data collected on the North Slope of Alaska with a terrestrial lidar, I was able to compare snow barchan dunes to their sand equivalent. I was also able to infer some of the dynamic behavior of snow dunes (during the formation process) and compared these to the sand dunes. Reviewing all the documented observations of snow bedforms led me to construct the first-ever genetic classification of the various bedforms. The new classification system uses the two main factors controlling the flux of blowing snow: wind speed, and susceptibility of snow to be transported by wind (essentially erodibility), to classify snow bedforms.

In Chapter 3, I investigated the processes responsible for the smoothing effect of snow accumulating on top of micro-topographic relief in calm conditions (no wind). Without lateral displacement of snowflakes during their deposition, smoothing would not be possible (nor would it be for any other granular material as well). I identified through review and experimentation what I believe is the complete set of processes responsible for either enhancing or inhibiting the lateral displacement of snowflakes. I found bouncing to be the strongest process in smoothing snow landscapes, with cohesion between snowflakes the primary process preventing smoothing. The rate at which a bump can be smoothed depends on a wide range of variables, with air temperature and snowflake properties (size, shapes, fall speed) being the primary ones. At the macro-scale of the snowpack, I found that the filling of snow on top of a bumpy surface occurred in three stages. First snow accumulates between bumps, leaving a discontinuous surface with heterogeneous properties (i.e, bare tops and covered bottoms). Next, the snow surface becomes continuous and homogenous (bumps covered). At that point, the bumps are attenuated by the snow, which shows decreasing amplitudes and increasing widths. A third and last stage corresponds to the point at which amplitude reduction ceases, but a constant and slow increase in the width of the bumps continues. The dynamic evolution of the snow surface appears to be driven by curvature, which corroborates the

work of *Edwards and Wilkinson* [1982]. They found that the surface growth of a purely granular material was proportional to the surface curvature. The coefficient of proportionality, called the surface tension or diffusivity by Edward and Wilkinson, for snow is a tuning parameter reflecting the cumulative strength of at least 14 grain-scale processes identified through the experimental work.

The last study, focusing on the deposition of snow in the boreal forest, identified five types of canopies that interact with the falling snow. These are differentiated by their effect on the shape of the final snowpack. From large spruce tree canopies, to small canopies composed of vascular plants, snow is intercepted, loading branches or leaves, and eventually bridging gaps and producing a continuous snow cover in the canopies. The overall effect of canopies on snow distribution is driven by their size relative to the snow depth (*i.e.* h_s/h_o). When this ratio is small ($\lambda<<1$; *e.g.* for tall tree) the impact on the snow distribution is radically different than when this ratio is large ($\lambda >> 1$). Large trees (*e.g.* spruce) intercept snow, depleting the amount of snow reaching the ground cover. Smaller evergreen trees like small spruce maintain a snow-free zone around them, creating chimney-like discontinuities in the snowpack cover.

The second effect of vegetation canopies on snow depends on mechanical behavior of canopies. For instance, I identified two types of shrubs, the first being supple and bending under the load of intercepted snow, and the second being stiff and retaining the same geometry despite the snow loading. At the bottom of the snowpack I was surprised to discover throughout the entire winter the presence of air cavities occupying 10% to 50% or more of the snowpack vertical cross section, with the amount decreasing through the winter, but never dropping below 10%. I found two main types of plants associated with the presence of air cavities: supple shrubs and tussocks. As previously stated, supple shrubs bend under the snow loads, but at a certain point, the matrix they form with their branches becomes a structure on top of which snow bridges and builds, leaving empty space below this roofing structure. Tussocks, due to their shape and dense canopy, shed snow aside typically leaving an air cavity in the shape of a torus surrounding the tussock. Undetected by the lidar, these cavities would lead to overestimation of snow depth by 10% at the end of winter. Their formation must also have implication for the decimeter scale snow distribution, preventing snow to fill volumes typically of about 225 cm^3.

In chapters 2, 3 and 4, the questions asked were simple in appearance: *What controls the shape and size of snow bedforms? How is the underlying topography smoothed by snow? What are the effects of the various plants of the boreal forest on the shape of the snowpack?* In all three cases, I was drawn to focus on the linkage between processes occurring at the grain scale and the results seen at the macro scale (0.1 – 10 m). The three studies ended with similar results: a comprehensive list or identification of the key components of each system. Identification is not understanding, of course, but I hope that these lists of grain-scale processes will not only guide future snow research, but also be used in scientific disciplines beyond the snow community. For example, they might provide useful information to studies of sand bedforms and other cohesive materials shaped by aeolian processes (*i.e.* soil material found on Mars). The studies also clarified some of the next steps for furthering our knowledge of snow from the grain–scale to the decameter scale, and allowed us to identify where the biggest gaps in our knowledge lie.

The first study area (Chapter 2), concerning snow bedforms, had not been revisited in detail since *Kobayashi* (1980). Building on a comparison of snow bedforms to sand bedforms and developing a new classification helped to identify the gaps in knowledge that need to be addressed in the future.

- The analysis used relies on the effect of sintering as detailed in two older studies, *Kotlyakov* [1966] for linking the amount of snow transported by wind, and *Gow and Ramseier* [1964] for the effect of time on snow hardness. While the effect of temperatures, humidity and grain size is well understood [*Hobbs and Mason*, 1964], the effect of time on sintering is poorly documented, and dates back to experiments run in the 50's and 60's in Antarctica for expressing the effect of sintering (increasing the material strength) to hardness (increasing the compressive strength). For determining the susceptibility of snow (the threshold wind speed) to be transported by wind, there are two methods and they too are both old. The most frequently used is to assume a threshold wind speed for the snow surface [*Li and Pomeroy*, 1997], but this does not take into account the feedback between the wind and the surface itself. If one wants to study the detailed morphology of wind-blown surfaces, we need to extend *Kotlyakov*'s [1966] approach, linking the local snow hardness to the threshold wind speed, while considering the effect of the surface geometry on the wind.

- The lack of consistency among the measurements of bedform observations is also an obstacle to better understanding their physics, limiting the possibility to compare observations. Here I have at least introduced a systematic method for measuring basic geomorphological metrics (length, width, and height) for barchan dunes. This method was borrowed from the study of sand barchans. Systematic methods of measurement need to be established and expanded to the other bedforms, in particular to sastrugi, before more universal understanding of how they form is developed.

- Sastrugi are ubiquitous in the world of snow bedforms, but the term implies an entire family of erosional features. There is still a lot of confusion in the literature about describing and naming these features. One of the main problems, as discussed in our study, is the difficulty in extracting simple metrics for characterizing their shape. I showed that their inception might originate in subtle variations of hardness (resistance to erosion) of the foreset beds of snow deposition, but their formation process is still poorly documented and understood, and requires additional knowledge about sintering, and the deposition of snow in the lee side of bedforms, before a general model of sastrugi can be developed.

Chapter 3, on smoothing, raised a research question that had no real antecedent within the snow community. Much of the inspiration for this study came from the field of computer vision, where practitioners have tried to simulate serene snowy landscapes for video games and virtual animations. I established a new qualitative framework for approaching the mechanism of smoothing. In the discussion I introduced the model by *Edwards and Wilkinson* [1982], which is a continuous model at the macroscopic scale. This model does not tie the grain scale processes we observed to the macro-scale behavior of the snow surface, but at least it can predict the resulting surface smoothing with good accuracy. Much work is going to be necessary in quantifying processes like cohesion, interlocking or packing, before a physical model of smoothing can be developed. The work also led to questioning one concept that has been in the snow literature for more than 40 years: the angle of repose. Supposedly this is the maximum angle at which snow grains can remain in position, but I found that this angle differs greatly depending on the influx and available space conditions. *Kuroiwa et al.* [1967] had already observed from their laboratory experiment that the angle of repose depended on temperature, snowflake shapes and the proportion between the receptacle size and the drop height. If now we consider naturally falling snow, it remains unclear to us why there would be

various angles of repose for the same snowfall, yet the experimental results suggest that this is the case.

Applying a grain-scale approach to studying the deposition of snow in a forest remains unsolved. Forests present such challenging geometry that representing them mathematically will be very difficult. Recent work like that of *Moeser et al.* [2015] where they used an airborne lidar to derive more comprehensive metrics representative of canopies, shows some promise, but more work will need to be done before we know how to do this well. The next obstacle I identified is the variety in response to the different canopies to snow loading. Within the same landscape, the mechanical properties of the plants can be quite different, ranging from supple to stiff. Feeding back to the geometry of the scene, the forest itself is in continuous evolution, adapting its shape to the accumulation of snow.

Bridging is another particular process that I observed to have impact on the deposition of snow in canopies and on the formation of the bottom interface of the snowpack. Despite being prevalent in tree canopies and in the shrub understory, we still know little about how two clumps of snow separated by an air gap manage to bridge the gap. Cohesion, creep, and interlocking are probably part of the answer. For producing credible winter scenes, *Festenberg and Gumhold* [2011] had to include in their snow cover simulation algorithm an add-on and completely heuristic parameter for mimicking bridging.

The application of physics developed for purely granular materials (*e.g.* sand) to snow is not always a simple thing. Snow is a unique material that falls uniformly from the sky, that covers entire landscapes, and that presents particular physical processes because it is only a few degrees away from its fusion temperature (0 °C) wherever it is found. Snowflakes can sinter, forming ice bonds when brought in contact. As soon as deposited, snowflakes start metamorphosing depending on the local conditions bounding the snowpack. Depth hoar crystals (striated cup shaped) will form under the action of temperature and moisture gradients, and crystals will start rounding (minimizing their surface area) under temperatures at equilibrium. This constant adaptation of the material lattice structure to the local conditions is unique to snow, having no equivalent granular material. This is why the simple transposition from sand physics to snow is not possible without careful considerations.

For building on the work presented in this thesis I could imagine a series of experiments for quantifying individually the key processes identified above (*e.g.* snow hardening with time). Within the time period of this thesis, the cost for mapping surfaces in three-dimensions has significantly dropped. Lidar sensors are getting cheaper because of the development of the self-driving car industry (*e.g.* sensor companies like Velodyne and Quanergy). In the past six years, the cost has gone down by a factor of 20, and it is forecast to drop another 10X in the next few years. In parallel the development of technology like the Structure-From-Motion algorithms necessitating a commercial grade digital camera and a high-performance computer allows for creating high-resolution 3D models of snow surfaces with little investment cost [*Nolan et al.*, 2015]. At the same time, within this past few years, open hardware electronics like the microcontroller Arduino (www.arduino.cc) or the single board computer Raspberry Pi (www.raspberrypi.org) have appeared on the market, decreasing the cost of building data loggers and expanding the type of sensors to be used in future experiments. For instance the strobe light used in an experiment of chapter 3 was simply made with an Arduino connected to LED strips. The ease and affordability of hardware for building the type of experiments that could be useful for improving our knowledge of snow at the grain scale is getting better. What will be needed are snow scientists using these new (and old) tools to connect grain scale processes to landscapes of snow.

References

Bagnold, R. A. (1941). The physics of wind blown sand and desert dunes. *Methuen, London*, 265(10).

Bartlett, P., and M. Lehning (2002). A physical SNOWPACK model for the Swiss avalanche warning: Part I: numerical model. *Cold Regions Science and Technology*, 35(3), 123-145, doi: 10.1016/S0165-232X(02)00074-5

Brun, E., E. Martin, V. Simon, C. Gendre, and C. Coleou (1989). An energy and mass model of snow cover suitable for operational avalanche forecasting. *Journal of Glaciology*, 35(12), 1.

Edwards, S. F., and D. R. Wilkinson (1982), The Surface Statistics of a Granular Aggregate, *Proceedings of the Royal Society A: Mathematical, Physical and Engineering Sciences*, 381, doi: 10.1098/rspa.1982.0056.

Festenberg, N., and S. Gumhold (2011), Diffusion-Based Snow Cover Generation, *Computer Graphics Forum*,30, doi: 10.1111/j.1467-8659.2011.01904.x.

Gow, A. J., and R. O. Ramseier (1964), Age hardening of snow at the South Pole, *CRREL Research Report*, 112, p. 19.

Hobbs, P. V., and B. Mason (1964), The sintering and adhesion of ice, *Philos. Mag.*, 9(98), 181–197.

Kuroiwa, D., Y. Mizuno, and M. Takeuchi (1967). Micromeritical properties of snow. *Physics of Snow and Ice: proceedings= 雪氷の物理学: 論文集*, *1*(2), 751-772.

Kobayashi, S. (1980), Studies on interaction between wind and dry snow surface, *Contributions from the Institute of Low Temperature Science*, *29*, 1–64.

Kotlyakov, V. M. (1966), The Snow Cover of the Antarctic and Its Role in the Present Day Glaciation of the Continent, vol. 7, *Israel Program for Scientific Translations*, Jerusalem, Israel.

Li, L., and J. W. Pomeroy (1997): Estimates of Threshold Wind Speeds for Snow Transport Using Meteorological Data. *Journal of Applied Meteorology and Climatology*, 36, 205–213. doi: 10.1175/1520-0450(1997)036<0205:EOTWSF>2.0.CO;2

Liston, G. E., and M. Sturm (2002). Winter precipitation patterns in arctic Alaska determined from a blowing-snow model and snow-depth observations. *Journal of hydrometeorology*, *3*(6), 646-659, doi: 10.1175/1525-7541(2002)003<0646:WPPIAA>2.0.CO;2

Moeser, D., M. Stähli, and T. Jonas (2015). Improved snow interception modeling using canopy parameters derived from airborne LiDAR data. *Water Resources Research* 51, no. 7 (2015): 5041-5059, doi: 10.1002/2014WR016724.

Mote, T. (2008), On the Role of Snow Cover in Depressing Air Temperature, *Journal of Applied Meteorology and Climatology*, 47(7), 20082022, doi: 10.1175/2007JAMC1823.1.

Nolan, M., C. F. Larsen, and M. Sturm (2015). Mapping snow-depth from manned-aircraft on landscape scales at centimeter resolution using Structure-from-Motion photogrammetry. *The Cryosphere*, 9(1), 333-381, doi: 10.5194/tc-9-1445-2015.

Orsolini, Y., and N. Kvamstø (2009), Role of Eurasian snow cover in wintertime circulation: Decadal simulations forced with satellite observations, *Journal of Geophysical Research: Atmospheres* (1984–2012), 114(D19), doi: 10.1029/2009JD012253.

Rutter, N., R. Essery, J. Pomeroy, N. Altimir, K. Andreadis, I. Baker, A. Barr, P. Bartlett, P. Boone, H. Deng, and H. Douville (2009), Evaluation of forest snow processes models (SnowMIP2), *Journal of Geophysical Research*, 114(D6), doi: 10.1029/2008JD011063

Schmidt, R. A. (1980), Threshold wind-speeds and elastic impact in snow transport, *Journal of Glaciology*, *26*, 453-467.

Schmidt, R. A. and D. Gluns (1991), Snowfall interception on branches of three conifer species, *Canadian Journal of Forest Research*, 21(8), 1262–1269, doi:10.1139/x91-176.

Walker, D. A., J. C. Halfpenny, M. D. Walker, and C. A. Wessman (1993). Long-term studies of snow-vegetation interactions. *BioScience*, 43(5), 287-301, doi: 10.2307/1312061